A dynamical systems approach to unsteady systems

Thesis by

Shawn C. Shadden

In Partial Fulfillment of the Requirements

for the Degree of

Doctor of Philosophy

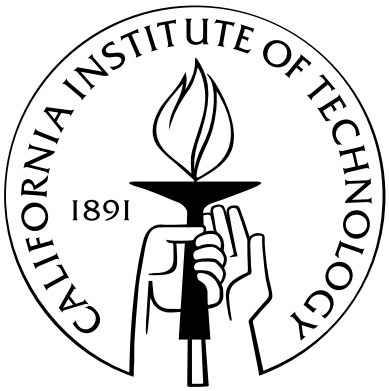

California Institute of Technology

Pasadena, California

2006

(Defended April 12, 2006)

To my parents, David and Diane Shadden.

Acknowledgements

I will always value having Jerrold Marsden as my advisor. Jerry is a first-class researcher, but his selfless character makes him an asset to society as much as to science. His positive influence on my professional and personal development will continue to benefit me throughout life.

Much of this thesis would not have been possible without the patient mentorship of Francois Lekien. His remarkable proficiency in both theory and numerics makes Francois a sound researcher. Francois introduced me to the concepts from which this thesis is based, and has played an integral role in the development of many of the results listed herein. I would also like to thank Francois, along with Chad Coulliette, for use of the software package MANGEN, which was used to compute many of the results listed in this thesis.

Much of this work has followed in the footsteps of George Haller, who has been a valuable resource, both through personal communication and through his enjoyable publications related to this subject.

Some of the most interesting results of this thesis are with the applications. I sincerely thank Frederic Bottausci, Yi Chow, Tim Colonius, Mike Cook, John Dabiri, Jeff Eldredge, Pierre Lermusiaux, Igor Mezić, Jeff Paduan, Igor Shulman, and Kakani Young for providing a diverse array of interesting applications for me to work on.

The biggest hurdle for first year students in the department of Control and Dynamical Systems are the qualifying exams. I am grateful to Lijun Chen for his help in preparing with me for the exams. Like many students doing their PhD, my research often shifted between various avenues before it settled into something meaningful enough to write a thesis about. I began my graduate research in the area of collision avoidance for multiple vehicle systems with the kind mentorship of Dong Eui Chang. I also spent several months working with Troy Smith on Dirac Structure, which I let fall to the wayside, but to my content, Troy was able to advance.

During my tenure at Caltech, I have met and interacted with an array of interesting and gifted individuals. I feel that this section would not be complete without thanking Harish Bhat, Bill Dunbar, Eva Kanso, Rouslan Kretchetnikov, Melvin Leok, Naomi Leonard, Tosin Otitoju, Shane Ross, Wang Sang Koon, Jair Koiller, and Wendy McKay for all their help and guidance. In addition, I greatly value having met my good friends James Faddy, Sean Humbert, Eimear Kenny, and Brian Zid. I sincerely appreciate the rich experience that I enjoyed during my time at Caltech and I know that I will miss all that the Institute has to offer.

I was supported by a National Science Foundation graduate student fellowship during my graduate work, which provided much freedom. The Office of Naval Research grants N00014-02-1-0826 and N00014-04-1-0534 and ONR-MURI Contract 00000916 provided additional funding needed to make the research successful.

I would last like to express my gratitude for those closest to me, my parents Dave and Diane, and my fiancée, Jen, for their open minds, unconditional support, and inspiration.

A dynamical systems approach to unsteady systems

by

Shawn C. Shadden

In Partial Fulfillment of the Requirements
for the Degree of
Doctor of Philosophy

Abstract

For steady systems, interpreting the flow structure is typically straightforward because streamlines and trajectories coincide. Therefore the velocity field, or quantities derived from it, provide a clear description of the flow geometry. For unsteady flows, this is often not the case. A more natural choice is to understand the flow in terms of particle trajectories, i.e., the Lagrangian viewpoint. While the chaotic behavior of trajectories of unsteady systems makes direct interpretation difficult, more structured and frame-independent techniques have been developed. The method presented here uses finite-time Lyapunov exponent (FTLE) fields to locate Lagrangian Coherent Structures (LCS). LCS are co-dimension 1 separatrices that partition regions in phase space with dynamically different behavior. This method enables the detection of often non-obvious, time-dependent boundaries in complicated flows, which greatly elucidates the transport and mixing geometry.

The first portion of this thesis deals with the theoretical development of LCS for two-, and then, n-dimensional systems, where $n > 2$. Based on the definitions presented, some important properties of these structures are proven. It is shown that the flux across an LCS is typically very small and depends on the relative strength of the structure, the difference between the local rotation rate of the LCS with that of the Eulerian velocity field, and the integration time used to compute the FTLE field.

The second portion of the thesis presents a series of numerical studies in which LCS are used to examine a range of interesting applications. This portion is bridged with the theoretical development presented in the first half by a brief chapter describing the numerical computation of FTLE fields and LCS. Applications presented in the second half of the thesis include the study of vortex rings in which LCS are used to define the unsteady vortex boundary to clarify the entrainment and detrainment processes; the computation of LCS in the ocean to provide mesoscale separatrices that help characterize the flow conditions and help navigate gliders or drifters used for sampling; flow over an airfoil where an LCS captures the unsteady separation profile; flow through a micro-mixing channel where LCS reveal the mechanism and geometry of chaotic mixing.

Contents

Chapter 1

Introduction

1.1 Background

Dynamical systems is a branch of applied mathematics with a keen interest in developing techniques to study the differential equation

$$\dot{\mathbf{x}} = \mathbf{v}(\mathbf{x}, t) \; . \tag{1.1}$$

There is no general analytic method for explicitly solving equation (1.1), unless $\mathbf{v}(\mathbf{x}, t)$ is time-independent and linear in $\mathbf{x}$; however, several methods have been developed to help analyze the behavior of such systems. This thesis explores a dynamical systems method for studying transport. In particular, we are interested in visualizing the flow geometry of unsteady dynamical systems by locating separatrices that partition otherwise complex particle motion into a coherent geometric picture. This thesis typically assumes that the system under study is a fluid system, however the methods are not restricted to such applications.

Most dynamical systems techniques assume that the vector field, $\mathbf{v}(\mathbf{x}, t)$, also known as the velocity field, does not explicitly depend on time. Such *steady* systems are the easiest to analyze. For example, streamlines and trajectories coincide for steady systems, thus viewing the Eulerian velocity field is often sufficient in understanding the transport structure. Additionally, the issues of mixing and transport are rather transparent because each location in space has a unique trajectory that passes through it. Nonetheless, separatrices exist in such systems and can help elucidate the exact partition of qualitatively different dynamics. These separatrices are given by the stable and unstable manifolds of hyperbolic, saddle-type fixed points. In particular, cases when the unstable manifold and the stable manifold for the same (homoclinic) or different (heteroclinic) saddle points coincide are of particular interest because these connections typically bound finite volumes of qualitatively distinct dynamics. Saddle-type hyperbolic fixed points are the most interesting because they are responsible for the stretching of fluid blobs, a precursor to mixing [69]. Additionally, for fluids satisfying continuity (i.e., incompressible and containing no sources or sinks) the hyperbolic points

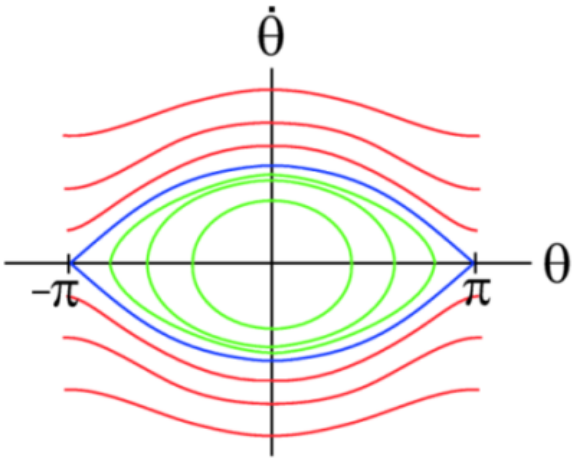

Figure 1.1: Phase portrait of pendulum. Angle θ is measured counter-clockwise from pendulum in downward state.

will be saddle points.

As the name implies, a saddle point can be thought of as the turning point that dictates nearby trajectories to have varying behavior. As a motivating example, consider the phase portrait of the pendulum shown in Figure 1.1. The hyperbolic fixed points at $(-\pi, 0)$ and $(\pi, 0)$ correspond to the pendulum in the inverted state. The unstable manifold of $(-\pi, 0)$ is the stable manifold of $(\pi, 0)$, thus forming a heteroclinic connection (shown in blue). In the upper quadrants, this connection is the dividing line, or separatrix, which separates trajectories of the pendulum spinning continuously in the counter-clockwise direction, from trajectories of the pendulum swinging back and forth.

When the velocity field is time-dependent, trajectories and streamlines can quickly diverge and thus it can be very difficult to interpret the flow geometry from naive interpretations that are commonly used for steady systems. Even for systems where the time-dependence is periodic and of very small amplitude, trajectories can become seemingly random, a phenomenon known as deterministic chaos, or chaotic transport. Studying periodic systems at fixed intervals of time, equal to the period of the vector field, can factor out the time-dependence of the governing equations, reducing the dynamics to a time-independent map, known as the Poincaré map. Such an approach can greatly simplify the dynamics and allow the application of traditional dynamical systems constructs that were developed for steady systems. For example, hyperbolic fixed points of the Poincaré map produce stable and unstable manifolds in the Poincaré section (the domain of the Poincaré map) that partition otherwise chaotic trajectories of the unsteady system. Additionally, these manifolds often intersect in a remarkably ordered manner to reveal the precise geometry of how mixing occurs [87, 88]. Steady or periodic systems are common in engineering so the established techniques for analyzing such systems can be quite useful, and these techniques form the foundation of much of the dynamical systems literature [28, 69, 111, 108].

Most interesting, real-world systems are not steady or even periodic. Additionally, just as the flow of a steady system can change dramatically from the addition of a time-periodic perturbation, the presence of aperiodicity can greatly complicate the dynamics and cause the analytic techniques used for steady and periodic systems to become irrelevant. However, it should still seem reasonable to try to locate analogous separating structures in aperiodic systems. Indeed, such separatrices are present in a remarkable range of practical applications, as we will be shown in this thesis.

When the right-hand side of equation (1.1) has general time-dependence, fixed points, periodic orbits, or other invariant sets are generally not available for defining invariant manifolds in the usual sense. Instead, one may rely on methods such as the study of uniformly hyperbolic trajectories [85, 78, 115] or exponential dichotomies [12, 55]. Such techniques can be thought of as extensions of traditional techniques used to locate stable and unstable manifolds in unsteady systems. That is, these techniques try to locate, *directly*, trajectories of the system that are analogous to stable and unstable manifolds. Such techniques are typically applied to analytic advection models where the behavior is known for all time. For many applications though, especially in fluid dynamics, the velocity field is only known over a finite time interval. For instance, this is typical of numerically generated flows resulting from the integration of a model or an approximation of the Navier-Stokes equations. Other practical concerns also limit the applicability of these methods.

This thesis relies on a more indirect means of locating separatrices in unsteady flows. This method is preferable because of its relative simplicity and wide applicability. We refer to these separatrices as Lagrangian Coherent Structures (LCS).[1] This terminology is motivated by the work of George Haller.

In a series of papers [29, 31, 30, 32], Haller and coworkers give refined versions of necessary and sufficient conditions for the existence of "finite-time hyperbolic manifolds" in aperiodic flows, which are analogous to the traditional invariant manifolds that are defined for time-independent, or time-periodic, systems. Haller refers to these "finite-time hyperbolic manifolds" as Lagrangian Coherent Structures, providing a precise definition of these structures based on dynamical systems constructs. In practice, Haller suggests that LCS can be found from a *hyperbolicity time approach*. Using this approach, LCS are defined by local extrema of the hyperbolicity time field, which measures how long each trajectory remains hyperbolic. In [30] Haller gives an alternative definition of LCS in §2.3 of that paper as local extrema of the finite-time Lyapunov exponent field (FTLE) and shows the strong correspondence between LCS computed from hyperbolicity time fields and finite-time Lyapunov exponent fields for steady and forced ABC (Arnold-Beltrami-Childress) flows. It should be noted that Pierrehumbert [76] and Pierrehumbert and Yang [77] provide two of the earlier references to the use of FTLE fields for capturing finite-time coherent structures to capture chaotic mixing regions

[1] Throughout this thesis, LCS is used for both the singular and plural forms, where the appropriate abbreviation should be clear from the context.

and transport barriers.

While there is a large body of literature on coherent structures in fluid mechanics that we will not attempt to overview here, [53, 59, 82, 30, 39] provide many useful references on the dynamical systems approach to this subject. There is a consensus that hyperbolic structures are critical to understanding transport; however there is a contention on the best way to measure hyperbolicity or compute these structures. There is typically a trade-off between the amount of rigor underpinning a particular method, and its practicality in studying a diverse range of applications. Based on this trade-off, this thesis hopes to justify the use of FTLE fields for locating LCS by addressing these issues.

1.2 Purpose

The goals of this thesis are to

- Offer a practical and robust method to study the flow geometry of unsteady systems, extending methods usually restricted to idealized examples to practical applications.
- Develop theoretical underpinnings for this method, which were previously missing in the literature.
- Demonstrate the application of these methods to a range of practical examples and explore the added knowledge gained by the analysis.

1.3 Organization

The general organization of this thesis is *theory*, *numerics* and then *computational results*. In particular, Chapter 2 gives a precise definition for LCS from FTLE fields for planar systems and proves some useful properties of these structures. Chapter 3 extends the results of Chapter 2 to n-dimensional systems. Chapter 4 describes the numerical implementation of computing FTLE fields and LCS, and associated practical issues. Chapters 5 through 8 contain applications of LCS to a range of practical problems and discuss the knowledge gained from the results.

Most of the chapters in this thesis were formed from a series of published papers or papers in preparation. However, an attempt has been made to integrate them as to prevent redundancy, yet keep the results independent to facilitate publication. A list of papers used to develop Chapters 2, 3, 5, 6, and 7 are listed below, along with my contribution to each paper.

Chapter 2

S. C. Shadden, F. Lekien and J.E. Marsden, Definition and properties of Lagrangian coherent

structures from finite-time Lyapunov exponents in two-dimensional aperiodic flows, *Physica D* **212**(3–4), 271-304, 2005.

My contributions to this paper were helping to develop the exact definition of LCS from FTLE fields; deriving the properties of these structures; analyzing the derived flux estimate on the double-gyre model; and helping to write the paper. Dr. Lekien and my contributions to this paper were comparable.

Chapter 3

F. Lekien, S. C. Shadden and J.E. Marsden, Lagrangian Coherent Structures in N-dimensional systems, In preparation.

My contributions to this paper were helping to develop the exact definition of LCS from FTLE fields; deriving the properties of these structures; and helping to write the paper. Dr. Lekien and my contributions to this paper were comparable.

Chapter 5

S. C. Shadden, J. O. Dabiri and J.E. Marsden, Lagrangian analysis of fluid transport in empirical vortex ring flows, *Physics of Fluids* **18**(4), 2006.

My contributions to this paper were the developments of the Analytical Methods and Results sections, and to help with the development of the Introduction and Conclusion sections.

Chapter 6

T. Inanc, S. C. Shadden and J. E. Marsden, Optimal trajectory generation in ocean flows, *Proc. of the American Control Conference*, June 2005, Portland, OR.

My main contributions to this paper were writing the draft of the paper; providing the LCS computations; helping to formulate the optimal control problem; and helping to edit the paper.

Chapter 7

S. C. Shadden, F. Lekien, J. D. Paduan and J.E. Marsden, Transport barriers in the ocean: Computation and verification, In preparation.

My main contributions to this paper were preparing the draft and running the computations to produce the results of all LCS computations.

Chapter 2

Definition and Properties of LCS from FTLE Fields in Two-Dimensional Flows

In collaboration with Francois Lekien and Jerrold E. Marsden

2.1 Introduction

The motivation for developing a precise definition of LCS is that numerous works, such as [110, 48, 38, 92], have demonstrated the usefulness of FTLE plots and their associated LCS for studying systems with arbitrary time-dependence. However, there has remained the issue of making the Lagrangian transport properties of LCS precise. Based on previous numerical results, it was thought that LCS are, at least approximately, transported as sets by the flow and so should be approximately Lagrangian. Additionally, in [30, 32], LCS as determined from FTLE fields were referred to as material lines, meaning that they should be advected by the flow. However, numerical studies have shown that ridges in the FTLE field (i.e., LCS) sometimes can exhibit non-Lagrangian behavior such as bifurcations and that they may have a small material flux. One such example can be found in [48] or at `http://www.lekien.com/~francois/papers/rsmas`.

The purpose of the present chapter is to fill some of the missing gaps in the question "How Lagrangian are LCS?". We do this by

1. Carefully analyzing the basic definition of LCS.
2. Deriving expressions for the exact flux across an LCS in a form that enables one to estimate its Lagrangian transport properties.
3. Verifying and illustrating the properties on both an analytic and empirical example.

We define LCS as ridges in the FTLE field. Ridges are *special gradient lines of the FTLE field that are transverse to the direction of minimum curvature.* We show that for a well-defined LCS (satisfying certain nondegeneracy conditions), the flux across the structure, while not necessarily zero, is usually negligible, and therefore these structures are effectively invariant manifolds and hence act as transport barriers. In particular, for a given FTLE field that admits an LCS, we construct a scalar function $L(\mathbf{x}, t)$ such that the LCS is given by the level set $L(\mathbf{x}, t) = 0$.

A key fact, established in §2.4.3 shows that the flux across an LCS is given by

$$\Phi(t) = \int_{\text{LCS}} \frac{\mathrm{d}L}{\mathrm{d}t}\, \mathrm{d}s\ . \tag{2.1}$$

The main result of the chapter, given in equation (2.66) of Theorem 2.4.4, is the following estimate for $\mathrm{d}L/\mathrm{d}t$ based on quantities derived from the FTLE and velocity fields:

$$\frac{\mathrm{d}L}{\mathrm{d}t} = \underbrace{\frac{\langle \hat{\mathbf{t}}, \nabla\sigma \rangle}{\langle \hat{\mathbf{n}}, \Sigma\hat{\mathbf{n}} \rangle}}_{\text{term A}} \underbrace{\left\langle \hat{\mathbf{t}}, \frac{\partial \hat{\mathbf{n}}}{\partial t} - J\hat{\mathbf{n}} \right\rangle}_{\text{term B}} + \underbrace{\mathcal{O}\left(\frac{1}{|T|}\right)}_{\text{term C}}\ . \tag{2.2}$$

Ignoring, for now, the precise definition of all the quantities in the right-hand-side of equation (2.2), here is what they roughly mean: Term A measures how well-defined the ridge is, and goes to zero the sharper the ridge; term B represents the difference in the local rotation rate of the LCS from the local rotation rate of the Eulerian velocity field; and term C is a term that scales as $1/|T|$, where $|T|$ is the length of time over which the FTLE is computed. Therefore, we can see that for well-defined ridges or ones that rotate at a rate comparable to the local Eulerian field and are computed from an FTLE field that has a sufficiently long integration time, the flux across the LCS is expected to be small.

The purpose of the definition proposed here is twofold: First, a precise definition is required to prove analytical results, and second, it was developed to permit computational means to extract the LCS from numerical and experimental data. The results of this chapter are applied to two examples: an analytical double-gyre and observed ocean current data. We carefully study the rate at which particles cross the LCS and find that the rate is indeed very small, in fact it is less than 0.05% of the average velocity of fluid particles near the LCS in both examples.

2.2 Notation and Definitions

Let the open set $D \subset \mathbb{R}^2$ be the domain of the fluid under study. Given a time-dependent velocity field $\mathbf{v}(\mathbf{x}, t)$ defined on D, define a trajectory $\mathbf{x}(t; t_0, \mathbf{x}_0)$ starting at point $\mathbf{x}_0 \in D$ at time t_0 to be

the solution of

$$\begin{cases} \dot{\mathbf{x}}(t;t_0,\mathbf{x}_0) &= \mathbf{v}(\mathbf{x}(t;t_0,\mathbf{x}_0),t)\ , \\ \mathbf{x}(t_0;t_0,\mathbf{x}_0) &= \mathbf{x}_0\ . \end{cases} \tag{2.3}$$

A trajectory is seen mainly as a function of time. However, its dependence on the initial position $\mathbf{x}_0$ and the initial time t_0 will be most important in this work and we want to emphasize this aspect by keeping an explicit reference to the parameters $\mathbf{x}_0$ and t_0 in the solution of equation (2.3).

In this work, we shall be making a number of basic assumptions. The first, on smoothness, is in accord with traditional assumptions in fluid mechanics [69, 107]:

A1. *The velocity field* $\mathbf{v}(x,t)$ *is at least* C^0 *in time and* C^2 *in space,*

from which it follows $\mathbf{x}(t;t_0,\mathbf{x}_0)$ is C^1 in time and C^3 in space.

Fixing the initial time t_0 and the final time t, we can view the solution of the dynamical system given in equation (2.3) as a map that takes points from their position $\mathbf{x}_0$ at time t_0 to their position at time t. This map, referred to as the *flow map*, is denoted by $\phi_{t_0}^t$ and satisfies

$$\phi_{t_0}^t : D \to D : \mathbf{x}_0 \mapsto \phi_{t_0}^t(\mathbf{x}_0) = \mathbf{x}(t;t_0,\mathbf{x}_0)\ . \tag{2.4}$$

It follows from standard theorems on *local existence and uniqueness of solutions* [36] of equation (2.3), that the map $\phi_{t_0}^t$ satisfies the following properties:

$$\begin{cases} \phi_{t_0}^{t_0}(\mathbf{x}) &= \mathbf{x}\ , \\ \phi_{t_0}^{t+s}(\mathbf{x}) &= \phi_s^{t+s}(\phi_{t_0}^s(\mathbf{x})) = \phi_t^{t+s}(\phi_{t_0}^t(\mathbf{x}))\ . \end{cases} \tag{2.5}$$

2.2.1 Finite-Time Lyapunov Exponents

Roughly speaking, the FTLE is a finite time average of the maximum expansion rate for a pair of particles advected in the flow. For example, consider a point located at $\mathbf{x} \in D$ at time t_0. When advected, this point moves to $\phi_{t_0}^{t_0+T}(\mathbf{x})$ after a time interval T. To understand the amount of stretching about this trajectory, consider the evolution of the perturbed point $\mathbf{y} = \mathbf{x} + \delta\mathbf{x}(0)$ where $\delta\mathbf{x}(0)$ is infinitesimal and, for now, arbitrarily oriented. After a time interval T, this perturbation becomes

$$\delta\mathbf{x}(T) = \phi_{t_0}^{t_0+T}(\mathbf{y}) - \phi_{t_0}^{t_0+T}(\mathbf{x}) = \frac{\mathrm{d}\phi_{t_0}^{t_0+T}(\mathbf{x})}{\mathrm{d}\mathbf{x}}\delta\mathbf{x}(0) + \mathcal{O}\left(\|\delta\mathbf{x}(0)\|^2\right)\ . \tag{2.6}$$

This equation employs the *Landau* notation [56]; that is, $f(x) = \mathcal{O}(g)$ for a positive function g means that $f(x)/g(x)$ remains bounded for all $x \in \mathbb{R}$. The growth of linearized perturbations are obtained by dropping the $\mathcal{O}\left(\|\delta\mathbf{x}(0)\|^2\right)$ terms and so using the standard Euclidean norm, the magnitude of

the perturbation is given by

$$\|\delta\mathbf{x}(T)\| = \sqrt{\left\langle \delta\mathbf{x}(0),\ \frac{\mathrm{d}\phi_{t_0}^{t_0+T}(\mathbf{x})}{\mathrm{d}\mathbf{x}}^{*} \frac{\mathrm{d}\phi_{t_0}^{t_0+T}(\mathbf{x})}{\mathrm{d}\mathbf{x}}\delta\mathbf{x}(0) \right\rangle}\,, \tag{2.7}$$

where M^* denotes the adjoint (transpose) of M. The symmetric matrix

$$\Delta = \frac{\mathrm{d}\phi_{t_0}^{t_0+T}(\mathbf{x})}{\mathrm{d}\mathbf{x}}^{*} \frac{\mathrm{d}\phi_{t_0}^{t_0+T}(\mathbf{x})}{\mathrm{d}\mathbf{x}} \tag{2.8}$$

is a *finite-time* version of the (right) Cauchy-Green deformation tensor. Although Δ is a function of $\mathbf{x}$, t_0, and T, we suppress writing these explicit dependencies to avoid notational clutter.

Maximum stretching occurs when $\delta\mathbf{x}(0)$ is chosen such that it is aligned with the eigenvector associated with the maximum eigenvalue of Δ. That is, if $\lambda_{\max}(\Delta)$ is the maximum eigenvalue of Δ, thought of as an operator, then

$$\max_{\delta\mathbf{x}(0)} \|\delta\mathbf{x}(T)\| = \sqrt{\lambda_{\max}(\Delta)}\, \left\|\overline{\delta\mathbf{x}}(0)\right\|\,, \tag{2.9}$$

where $\overline{\delta\mathbf{x}}(0)$ is aligned with the eigenvector associated with $\lambda_{\max}(\Delta)$. Then, equation (2.9) can be recast as

$$\max_{\delta\mathbf{x}(0)} \|\delta\mathbf{x}(T)\| = e^{\sigma_{t_0}^{T}(\mathbf{x})|T|}\ \left\|\overline{\delta\mathbf{x}}(0)\right\|\,, \tag{2.10}$$

where

$$\sigma_{t_0}^{T}(\mathbf{x}) = \frac{1}{|T|} \ln \sqrt{\lambda_{\max}(\Delta)}\,. \tag{2.11}$$

Equation (7.3) represents the (largest) finite-time Lyapunov exponent with a finite integration time T, which is associated to point $\mathbf{x} \in D$ at time t_0. Notice that the absolute value of the integration time is used in equation (7.3). This work permits both positive and negative integration times T. Earlier work [30] motivates the use of backward-time integration for locating *attracting Lagrangian coherent structures* (e.g., unstable manifolds for time-independent vector fields), and forward-time integration for revealing *repelling Lagrangian coherent structures* (e.g., stable manifolds for time-independent vector fields). For brevity, we often refer to the FTLE as just $\sigma(\mathbf{x})$, or more simply σ, when the extra notation can be dropped without causing ambiguity.

Early work in the area of Lyapunov exponents [68] motivates the importance of restricting the study to flows satisfying the following condition:

A2. *There is a constant k such that*

$$\left\| \frac{d\phi_{t_0}^{t}(\mathbf{x})}{d\mathbf{x}} \right\| \leq e^{k|t-t_0|}\,, \tag{2.12}$$

for all t.

This assumption is reasonable assuming the velocity field is Lipschitz continuous, cf. Theorem 3.2.1.

In this chapter, we restrict the domain of the fluid D to be a subset of $\mathbb{R}^2$. There is no conceptual problem with working in higher dimensions, as we will see in Chapter 3, but the definitions and analysis presented in this chapter become somewhat more complicated.

In this work, we are concerned with trajectories that satisfy the property:

A3.

$$\ln \lambda_{\min}(\Delta) < 0 < \ln \lambda_{\max}(\Delta) \ . \tag{2.13}$$

Notice that for finite T, Δ measures the average deformation of a perturbation over the interval T. So for instance, if an (infinitesimal) circular blob of particles is placed about a trajectory that satisfies **A3**, then after an amount of time T, the blob will have expanded in one direction and compressed in the other to form an elliptical shape. We refer to such trajectories as finite-time hyperbolic [112].

If we were to take $T \to \infty$, we should assume that there exist arbitrary constants $\mu_{\min}$ and $\mu_{\max}$ such that the eigenvalues satisfy

$$\ln \lambda_{\min}(\Delta) \leq \mu_{\min} < 0 < \mu_{\max} \leq \ln \lambda_{\max}(\Delta) \ , \tag{2.14}$$

so that the logarithms of the eigenvalues are uniformly bounded away from zero. For most practical applications, the dynamical system is only defined on a finite interval of time and therefore, to consider $T \to \infty$, we can follow [39] and assume that the finite-time field is extended using bump functions, in which case uniform boundedness is equivalent to boundedness. However, this uniform boundedness property is not a problem in the finite time context.

All trajectories satisfying equation (2.13) are contained within an open set (not necessarily connected) of the extended phase space $D \times \mathbb{R}$. In the rest of this work, we assume that everything is done in this subset only. This restriction allows us to work only in regions where the Lagrangian Coherent Structures are co-dimension 1 manifolds. Hyperbolic trajectories for which the logarithm of both eigenvalues of the Cauchy-Green deformation tensor have the same sign correspond to *areas* of expansion or compression (source/sinks). These regions are of less importance in studying the Lagrangian barrier properties of the flow because there is no co-dimension 1 structure separating regions of different dynamics.

As mentioned in [29, 32, 109], flows that have lines of high shear can produce particle separation plots (e.g., FTLE fields) that will have ridges along the shear lines. The problem with this is that it is then hard to distinguish lines of high shear from "hyperbolic lines", i.e., lines about which there is exponential stretching orthogonal to the line. Assumption **A3.** precludes lines of pure shear and hence this chapter does not address the properties of LCS that result from such behavior.

Lemma 2.2.1 *The field $\sigma_t^T(\mathbf{x})$ is C^2 in space and C^1 in time.*

Proof. Since $\phi_{t_0}^{t_0+T}(\mathbf{x})$ is a C^3 in space (C^1 in time) diffeomorphism, the Cauchy-Green deformation tensor Δ is C^2 in space (C^1 in time) and invertible. Since equation (2.13) requires that the two eigenvalues are distinct, they are also C^2 in space (C^1 in time) functions. Also, Δ is a real symmetric matrix, so its two eigenvalues are real and positive. Hence the logarithm of the largest eigenvalue is C^2 in space and C^1 in time. □

2.2.2 Objectivity of the FTLE

A quantity is called **objective** if it remains invariant under coordinate transformations of the form

$$\mathbf{y} = Q(t)\ \mathbf{x}(\mathbf{x_0}, t_0, t) + \mathbf{b}(t)\ , \tag{2.15}$$

where $Q(t)$ is a time-dependent proper orthogonal matrix and $\mathbf{b}(t)$ represents a time-dependent translation. Equation (2.15) takes care of most physical transformations. We next show that the FTLE, σ, is objective. For an infinitesimal $\delta\mathbf{x_0}$,

$$\mathbf{x}(\mathbf{x_0} + \delta\mathbf{x_0}, t_0, t) = \mathbf{x}(\mathbf{x_0}, t_0, t) + \frac{\partial \mathbf{x}(\mathbf{x_0}, t_0, t)}{\partial \mathbf{x_0}} \delta\mathbf{x_0}\ . \tag{2.16}$$

Let

$$\delta\mathbf{x}(t) = \mathbf{x}(\mathbf{x_0} + \delta\mathbf{x_0}, t_0, t) - \mathbf{x}(\mathbf{x_0}, t_0, t) \tag{2.17}$$

and recall that

$$\max_{\delta\mathbf{x_0}} \|\delta\mathbf{x}(t)\| = e^{\sigma|t-t_0|}\ \left\|\overline{\delta\mathbf{x_0}}\right\| \tag{2.18}$$

where $\overline{\delta\mathbf{x_0}}$ is in the max eigenvalue direction and σ is the FTLE. After, applying a transformation of coordinates according to equation (2.15), then equation (2.17) becomes

$$\begin{aligned} \delta\mathbf{y}(t) &\doteq Q(t)\ \mathbf{x}(\mathbf{x_0} + \delta\mathbf{x_0}, t_0, t) - Q(t)\ \mathbf{x}(\mathbf{x_0}, t_0, t) && (2.19)\\ &= Q(t)\ \delta\mathbf{x}(t)\ . && (2.20) \end{aligned}$$

However, $Q(t)$ is an isometry, so the norm of $\delta\mathbf{y}(t)$ changes identically to the norm of $\delta\mathbf{x}(t)$, hence σ is objective, cf. equation (2.18).

Not surprisingly most Eulerian criteria fail to be objective. The reason is because these methods rely solely on the vector field. However, transformations are not done on the vector field, they are done on the coordinates. For example, the vorticity tensor, rate-of-strain tensor, and streamlines are not objective.

2.2.3 Ridges and LCS

FTLE fields for a wide variety of flows reveal distinguished lines of high FTLE. While detecting these structures is usually obvious by inspection, an exact definition is required to facilitate proving properties of the structures and for building efficient numerical algorithms to extract these curves. For an FTLE field, $\sigma_{t_0}^T(\mathbf{x})$, we define Lagrangian Coherent Structures as *ridges* of the field. In this section, we make this definition precise.

As a small point, from a geometric point of view, a ridge of an arbitrary surface should lie *within* that surface. However for our application we are concerned with extracting ridges of the *graph* of the function $\sigma : D \subset \mathbb{R}^2 \to \mathbb{R}$, where the graph is thought of as a surface in $\mathbb{R}^3$. Since the motion of the fluid is confined to the domain $D \subset \mathbb{R}^2$, it only makes sense to define the parametrization of the ridge over D, that is, the ridge lies within the domain D and not within the graph of σ.

Below, we give two alternative, but similar, definitions of a ridge, the first being a *curvature ridge* of an FTLE field. Key concepts in this geometric definition are that of principal curvatures and principal directions [67]. Our definition of a curvature ridge can easily be generalized for an arbitrary orientable surface. We then present a more convenient and somewhat simpler definition of a ridge known as a *second-derivative ridge*, which does not rely on the geometric notions of principal curvatures and directions, but instead on Σ, the Hessian of the FTLE field, i.e.,

$$\Sigma = \frac{d^2\sigma_{t_0}^T(\mathbf{x})}{d\mathbf{x}^2} \, . \tag{2.21}$$

It is instructive to keep in mind the intuition behind each definition. For example, if hiking along a "ridge" one would expect, 1) to be *locally* at the highest point in the field transverse to the ridge; that is if the hiker stepped to the right or left of the path, they would be stepping down, and 2) for the topography to drop off steepest in the direction transverse to the ridge; that is at each point on the ridge, the direction the topography decreases most rapidly should be transverse to the ridge. The two definitions below formally state these two conditions, however, they differ in the reference direction they use for "down." In the first definition, the downward direction is always parallel to the normal vector field of the graph, whereas in the second definition, the downward direction is fixed and points toward the xy-plane.[1]

Definition 2.2.1 *Let $\mathcal{G} \subset \mathbb{R}^3$ denote the graph of $\sigma : D \subset \mathbb{R}^2 \to \mathbb{R}$. Let $\pi : \mathcal{G} \to D$ be the standard projection map, with its associated tangent map $T\pi$. A* ***curvature ridge*** *of the graph $\mathcal{G}$ is an injective curve $\mathbf{c} : (a, b) \to D$, satisfying the following conditions for each s in the open interval (a, b):*

CR1. *The vectors $\mathbf{c}'(s) = \frac{d\mathbf{c}}{ds}$ and $\nabla\sigma(\mathbf{c}(s))$ are parallel.*

[1] We assume $D \subset xy$-plane.

CR2. *Regard $\mathcal{G}$ as an orientated surface in $\mathbb{R}^3$. Let $\mathbf{p} = \mathbf{c}(s)$ and $\tilde{\mathbf{p}} = \pi^{-1}(\mathbf{p}) \in \mathcal{G}$. Let $k^u_{\tilde{\mathbf{p}}}$ and $k^l_{\tilde{\mathbf{p}}}$ denote the maximum and minimum principal curvatures of $\mathcal{G}$ at the point $\tilde{\mathbf{p}}$ with corresponding unit principal vectors $\tilde{\mathbf{u}}^u_{\tilde{\mathbf{p}}}$ and $\tilde{\mathbf{u}}^l_{\tilde{\mathbf{p}}}$. We require that $k^l_{\tilde{\mathbf{p}}} < 0$ and that $T\pi(\tilde{\mathbf{u}}^l_{\tilde{\mathbf{p}}})$ be normal to $\mathbf{c}'(s)$.*

Definition 2.2.2 *A **second-derivative ridge** of σ is an injective curve $\mathbf{c} : (a, b) \to D$ satisfying the following conditions for each $s \in (a, b)$:*

SR1. *The vectors $\mathbf{c}'(s)$ and $\nabla\sigma(\mathbf{c}(s))$ are parallel.*

SR2. *$\Sigma(\mathbf{n}, \mathbf{n}) = \min_{\|\mathbf{u}\|=1} \Sigma(\mathbf{u}, \mathbf{u}) < 0$, where $\mathbf{n}$ is a unit normal vector to the curve $\mathbf{c}(s)$ and Σ is thought of as a bilinear form evaluated at the point $\mathbf{c}(s)$.*

Since the FTLE field, $\sigma^T_t(\mathbf{x})$, varies with time, t, it is often convenient to append a subscript on $\mathbf{c}(s)$ to refer to the time at which the FTLE is computed. Therefore, we write $\mathbf{c}_t(s)$ for a ridge in the FTLE field at time t. The objective of this chapter is to investigate how ridges of the FTLE field evolve over time. In particular, our goal is to show that $\mathbf{c}_t(s)$ behaves approximatively like a line of Lagrangian particles, i.e., a *material line*, when t is varied.

Theorem 2.2.1 *The curves $\mathbf{c}(s)$ given in the above definitions are C^2.*

Proof. By Lemma 2.2.1, $\nabla\sigma(\mathbf{c}(s))$ is C^1. By **SR2**, $\mathbf{c}'(s)$ is necessarily parallel to $\nabla\sigma(\mathbf{c}(s))$, hence we can always find a parametrization such that $\mathbf{c}'(s)$ is C^1, which implies that $\mathbf{c}(s)$ is C^2. □

The main difference between the two definitions lies in the following: In **CR2** the curvature is measured with respect to the tangent plane to the graph of σ at each point, whereas in **SR2**, the curvature is always with respect to the xy-plane. The first definition is more intrinsic, whereas the second is more intuitive. As expected, one can prove the two measures are equal at local extrema, at which the two planes are parallel. In the next section, we show that a second-derivative ridge is always a subset of a curvature ridge.

2.2.4 Equivalence between Ridges

The relationships between the curvature measures used in the two previous definitions can be summarized as follows:

Theorem 2.2.2 *For each point $\mathbf{p} \in D$, let $\mathbf{t}$ be a vector of arbitrary length oriented along $\nabla\sigma$ and $\mathbf{n}$ be a vector of arbitrary length oriented orthogonal to $\mathbf{t}$ (if $\nabla\sigma = 0$, $\mathbf{t}$ can be arbitrarily oriented). Let $\gamma_n = \Sigma(\mathbf{n}, \mathbf{n})$ and $\gamma_t = \Sigma(\mathbf{t}, \mathbf{t})$. As before, let $\tilde{\mathbf{t}} = (T\pi)^{-1}\mathbf{t}$ and $\tilde{\mathbf{n}} = (T\pi)^{-1}\mathbf{n}$. Then we have the*

following relations:

$$\gamma_n = \kappa\, k(\tilde{\mathbf{n}})$$
$$\gamma_t = \kappa^3\, k(\tilde{\mathbf{t}}),$$

where $\kappa = \sqrt{1 + \left(\frac{\partial\sigma}{\partial x}\right)^2 + \left(\frac{\partial\sigma}{\partial y}\right)^2}$.

Proof. Let the FTLE field be given by the function $\sigma(x, y)$ and $\mathcal{G}$ denote the graph $z = \sigma(x, y)$. The unit normal field to $\mathcal{G}$ is given by

$$\mathbf{u} = \frac{1}{\kappa}\left(-\frac{\partial\sigma}{\partial x}, -\frac{\partial\sigma}{\partial y}, 1\right) . \tag{2.22}$$

By definition [67], the normal curvature in the direction $\tilde{\mathbf{n}}$ is given by

$$k(\tilde{\mathbf{n}}) = \tilde{\mathbf{n}} \cdot \nabla_{\tilde{\mathbf{n}}}\mathbf{u} \tag{2.23}$$

where $\nabla_{\tilde{\mathbf{n}}}\mathbf{u}$ is the covariant derivative of $\mathbf{u}$ with respect to $\tilde{\mathbf{n}}$.

Using the preceding formula for an arbitrary vector $\mathbf{w} = (w_x, w_y, w_z)$, the curvature along $\mathbf{w}$ is given by

$$\begin{aligned} k(\mathbf{w}) \quad = \quad & \tfrac{1}{\kappa}\left(w_x^2 \tfrac{\partial^2\sigma}{\partial x^2} + 2w_x w_y \tfrac{\partial^2\sigma}{\partial x\partial y} + w_y^2 \tfrac{\partial^2\sigma}{\partial y^2}\right) \\ & -\tfrac{1}{\kappa^3}\left(\tfrac{\partial\sigma}{\partial x}\left(\tfrac{\partial\sigma}{\partial x}\tfrac{\partial^2\sigma}{\partial x\partial y} + \tfrac{\partial\sigma}{\partial y}\tfrac{\partial^2\sigma}{\partial y^2}\right) + \tfrac{\partial\sigma}{\partial y}\left(\tfrac{\partial\sigma}{\partial y}\tfrac{\partial^2\sigma}{\partial x\partial y} + \tfrac{\partial\sigma}{\partial x}\tfrac{\partial^2\sigma}{\partial x^2}\right)\right) w_x w_y \\ & -\tfrac{1}{\kappa^3}\left(\tfrac{\partial\sigma}{\partial x}\left(\tfrac{\partial\sigma}{\partial y}\tfrac{\partial^2\sigma}{\partial x\partial y} + \tfrac{\partial\sigma}{\partial x}\tfrac{\partial^2\sigma}{\partial x^2}\right) w_x^2 + \tfrac{\partial\sigma}{\partial y}\left(\tfrac{\partial\sigma}{\partial x}\tfrac{\partial^2\sigma}{\partial x\partial y} + \tfrac{\partial\sigma}{\partial y}\tfrac{\partial^2\sigma}{\partial y^2}\right) w_y^2\right) . \end{aligned} \tag{2.24}$$

Plugging in $\tilde{\mathbf{n}}$ for $\mathbf{w}$ in equation (2.24) and using the fact that

$$\nabla\sigma \cdot \mathbf{n} = 0 , \tag{2.25}$$

we get

$$k(\tilde{\mathbf{n}}) = \frac{1}{\kappa}\left(n_x^2\frac{\partial^2\sigma}{\partial x^2} + 2n_x n_y\frac{\partial^2\sigma}{\partial x\partial y} + n_y^2\frac{\partial^2\sigma}{\partial y^2}\right) = \frac{1}{\kappa}\Sigma\left(\mathbf{n}, \mathbf{n}\right). \tag{2.26}$$

Now let $\tilde{\mathbf{t}} = \mathbf{u} \times \tilde{\mathbf{n}}$. As above, define

$$k(\tilde{\mathbf{t}}) = \tilde{\mathbf{t}} \cdot \nabla_{\tilde{\mathbf{t}}}\mathbf{u}. \tag{2.27}$$

If $k(\tilde{\mathbf{t}})$ is expanded out and reduced, some algebra shows that

$$k(\tilde{\mathbf{t}}) = \frac{1}{\kappa^3}\left(t_x^2\frac{\partial^2\sigma}{\partial x^2} + 2t_x t_y\frac{\partial^2\sigma}{\partial x\partial y} + t_y^2\frac{\partial^2\sigma}{\partial y^2}\right) = \frac{1}{\kappa^3}\Sigma\left(\mathbf{t}, \mathbf{t}\right) . \tag{2.28}$$

□

Notice that $\kappa \geq 1$. Therefore, equality of the two curvature measures holds when $\kappa = 1$ which implies that $\nabla\sigma = 0$ (i.e., the tangent plane of $\mathcal{G}$ is parallel to the xy-plane).

Theorem 2.2.3 *A second-derivative ridge is always identical to or a subset of a curvature ridge.*

Proof. We must show that all points along a second-derivative ridge satisfy the conditions of a curvature ridge. Notice that **CR1** is trivially satisfied if **SR1** is true. Hence we must show **CR2**, that is, $k(\tilde{\mathbf{n}})$ is a minimum and less than zero, where $\tilde{\mathbf{n}}$ is the lift of $\mathbf{n}$, and $\mathbf{n}$ satisfies **SR2**, i.e.,

$$\Sigma(\mathbf{n}, \mathbf{n}) = \min_{\|\mathbf{u}\|=1} \Sigma(\mathbf{u}, \mathbf{u}) < 0 \tag{2.29}$$

with $\mathbf{n}$ orthogonal to $\nabla\sigma$.

From Theorem 2.2.2, $k(\tilde{\mathbf{n}})$ is necessarily less than zero if equation (2.29) is satisfied. Thus, it is left to show that $k(\tilde{\mathbf{n}})$ is minimized in the (lifted) direction orthogonal to the second-derivative ridge. It should be clear that the scaling introduced in Theorem 2.2.2 will not affect the difference in ridge definitions for all points in which Σ has a non-negative eigenvalue. Therefore, assume that the eigenvalues of Σ satisfy $\lambda_{\min} < \lambda_{\max} < 0$. Without loss of generality we can assume the second-derivative ridge is locally aligned with the x-axis, i.e., that $\frac{\partial\sigma}{\partial y} = 0$. This, along with equation (2.29), puts Σ in canonical form

$$\Sigma = \begin{bmatrix} \lambda_{\max} & 0 \\ 0 & \lambda_{\min} \end{bmatrix}. \tag{2.30}$$

Using this relation in equation (2.24) gives

$$k(\hat{\mathbf{u}}) = \frac{1}{\kappa}\left(u_x^2\lambda_{\max} + u_y^2\lambda_{\min}\right) - \frac{1}{\kappa^3}\left(|\nabla\sigma|^2\,\lambda_{\max}u_x^2\right) \tag{2.31}$$

for an arbitrary unit vector $\hat{\mathbf{u}} = (u_x, u_y, 0)$. Since $\lambda_{\min} < \lambda_{\max} < 0$, $k(\hat{\mathbf{u}})$ is minimized if $\hat{\mathbf{u}}$ is in the y-direction (i.e., $\hat{\mathbf{u}} = (0, 1, 0)$), which is the direction orthogonal to the second-derivative ridge. □

2.2.5 Ridge Example

Here we present an example to demonstrate the notions of curvature ridges and second-derivative ridges. Panels (a) and (b) of Figure 2.1 show the graph of an analytical test field σ. It seems intuitive to call the line $y = 0$ a ridge except along the "valley" of the graph, centered around the point $(2, 0)$ in the domain.

It is easily verified that **CR1**, and hence **SR1**, is satisfied for the line $y = 0$. The principal curvatures and second-derivative values given in **CR2** and **SR2** are plotted in Panel (c) of Figure 2.1. Panel (d) of Figure 2.1 shows a close-up around the value $x = 1.2$. Notice that **SR2** is satisfied for all x less than $x \approx 1.195$ (i.e., up to the 2nd-derivative curvature intersection point shown in

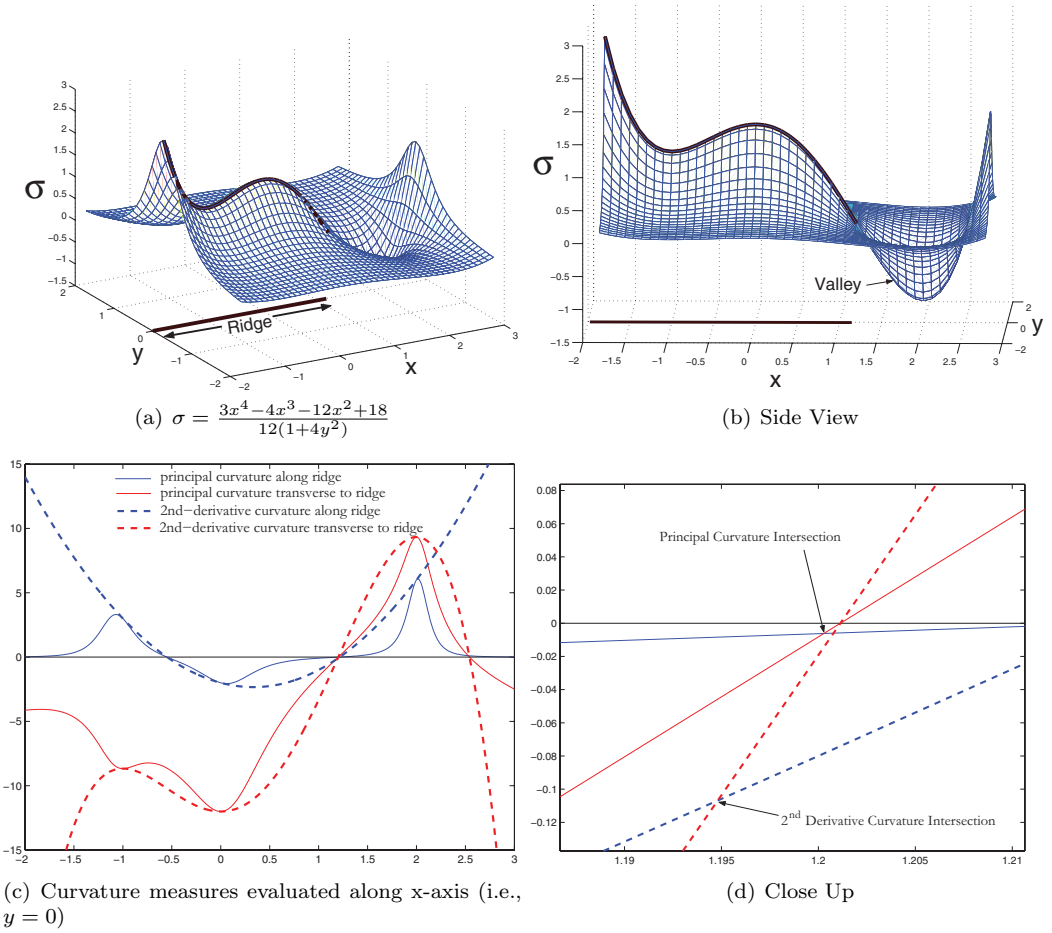

(a) $\sigma = \frac{3x^4-4x^3-12x^2+18}{12(1+4y^2)}$

(b) Side View

(c) Curvature measures evaluated along x-axis (i.e., $y = 0$)

(d) Close Up

Figure 2.1: Comparison between ridge definitions. Notice that the second-derivative ridge is slightly shorter than the curvature ridge

Panel (d)) whereas **CR2** is satisfied for all x less than $x \approx 1.2$ (i.e., up to the principal curvature intersection point shown on Panel (d) of Figure 2.1). Therefore we see that the second-derivative ridge is a subset of the curvature ridge, which is of course in agreement with Theorem 2.2.3. In addition, this example shows how the two measures produce near identical results in this case.

The functional form for σ in this example was chosen to produce an interesting test-case. For actual FTLE fields, σ typically does not vary much along the ridges of the field—in fact, much less than shown in this example. Therefore we can expect the difference between the two measures to be identically zero or non-existent for all practical purposes. For autonomous systems, σ is constant along a ridge (asymptotically), hence the two definitions of a ridge are always identical for such systems.

2.2.6 Lagrangian Coherent Structures

Given the graph of a function, the Hessian only represents the curvature of the graph at local extrema, therefore defining a ridge in terms of principal curvatures gives a better physical interpretation and is more intrinsic. However, the notion of a second-derivative ridge is somewhat simpler and more convenient, as we shall see later in this work. Also, we have shown that a second-derivative ridge is always a subset of a principal curvature ridge, and moreover the two definitions are nearly identical for all practical purposes. In addition, the second-derivative definition facilitates computational implementation. Therefore, we define LCS as follows:

Definition 2.2.3 *At each time t, a **Lagrangian Coherent Structure** (LCS) is a second-derivative ridge of the scalar field $\sigma_t^T(\mathbf{x})$.*

As evidenced from numerical results [76, 77, 110, 48, 38, 92], it is well-known that LCS can reveal an underlying flow structure in time-dependent systems that is typically not evident from the Eulerian field. In addition, these structures divide dynamically distinct regions in the flow, which allow for the easy analysis of transport. However, it is not clear from their definition that LCS are *material lines*. That is, notice that we are not distinguishing the trajectory of a given particle as an LCS, which of course by definition would be strictly advected by the flow. We are instead plotting the FTLE field and saying that ridges in the field are LCS. Therefore, it is not necessarily obvious that this curve we define should be advected by the flow. We shall address this issue in §2.4.

Recall that the FTLE field, $\sigma_t^T(\mathbf{x})$, is a Lagrangian measure over a *finite* interval of time. Therefore, we might expect the flux over an LCS to be inversely proportional to the integration time T. Also, we might expect that sharp, well-defined ridges are more Lagrangian than poorly defined ridges. Both parts of this intuition turn out to be true and are made precise in §2.4 where we derive a formula for the flux across the LCS and later show that in most cases the flux is negligible. In the next section, we evaluate the Lagrangian properties of the FTLE field itself.

2.3 Lagrangian FTLE Field

In this section we show that the finite-time Lyapunov exponent, $\sigma_t^T(\mathbf{x})$, is Lagrangian in the limit of large integration times T. Notice that this does not guarantee that the LCS are Lagrangian; they rely on higher derivatives of σ or on its curvature, which are generally not Lagrangian.

For an arbitrary 2×2 matrix, A, the natural matrix norm induced from the L_2-norm on $\mathbb{R}^2$ is defined as the largest eigenvalue of the matrix $\sqrt{A^*A}$. Therefore, the definition of $\sigma_{t_0}^T(\mathbf{x})$ can be conveniently recast as

$$\sigma_{t_0}^T(\mathbf{x}) = \frac{1}{|T|} \ln \left\| \frac{d\phi_{t_0}^{t_0+T}(\mathbf{x})}{d\mathbf{x}} \right\| . \tag{2.32}$$

Recalling that the traditional Lyapunov exponent is defined by equation (2.32) for $T \to \infty$, we then have:

Theorem 2.3.1 *The traditional Lyapunov exponent is constant along trajectories.*

This theorem could be restated as: *The finite-time Lyapunov exponent becomes constant along trajectories for large integration times T.*

Proof. We compare the value of the Lyapunov exponent computed at two different points of the same trajectory. Without loss of generality, to reduce notational clutter we assume that the initial time is $t_0 = 0$. Let $\mathbf{y} = \phi_0^s(\mathbf{x})$ for some arbitrary, but fixed, $s \in \mathbb{R}$. We have

$$
\begin{aligned}
|T| \left(\sigma_0^T(\mathbf{x}) - \sigma_s^T(\mathbf{y})\right) &= \ln \left\| \frac{\mathrm{d}\phi_0^T(\mathbf{x})}{\mathrm{d}\mathbf{x}} \right\| - \ln \left\| \frac{\mathrm{d}\phi_s^{s+T}(\mathbf{y})}{\mathrm{d}\mathbf{y}} \right\| \\
&= \ln \left\| \frac{\mathrm{d}(\phi_{T+s}^T(\phi_T^{T+s}(\phi_s^T(\phi_0^s(\mathbf{x})))))}{\mathrm{d}\mathbf{x}} \right\| - \ln \left\| \frac{\mathrm{d}(\phi_T^{s+T}(\phi_s^T(\mathbf{y})))}{\mathrm{d}\mathbf{y}} \right\| \\
&= \ln \left\| \frac{\mathrm{d}\phi_{T+s}^T(\hat{\mathbf{y}})}{\mathrm{d}\hat{\mathbf{y}}} \frac{\mathrm{d}\phi_T^{T+s}(\hat{\mathbf{x}})}{\mathrm{d}\hat{\mathbf{x}}} \frac{\mathrm{d}\phi_s^T(\mathbf{y})}{\mathrm{d}\mathbf{y}} \frac{\mathrm{d}\phi_0^s(\mathbf{x})}{\mathrm{d}\mathbf{x}} \right\| - \ln \left\| \frac{\mathrm{d}\phi_T^{s+T}(\hat{\mathbf{x}})}{\mathrm{d}\hat{\mathbf{x}}} \frac{\mathrm{d}\phi_s^T(\mathbf{y})}{\mathrm{d}\mathbf{y}} \right\| \\
&\leq \ln \left(\left\| \frac{\mathrm{d}\phi_{T+s}^T(\hat{\mathbf{y}})}{\mathrm{d}\hat{\mathbf{y}}} \right\| \left\| \frac{\mathrm{d}\phi_T^{T+s}(\hat{\mathbf{x}})}{\mathrm{d}\hat{\mathbf{x}}} \frac{\mathrm{d}\phi_s^T(\mathbf{y})}{\mathrm{d}\mathbf{y}} \right\| \left\| \frac{\mathrm{d}\phi_0^s(\mathbf{x})}{\mathrm{d}\mathbf{x}} \right\| \right) - \ln \left\| \frac{\mathrm{d}\phi_T^{s+T}(\hat{\mathbf{x}})}{\mathrm{d}\hat{\mathbf{x}}} \frac{\mathrm{d}\phi_s^T(\mathbf{y})}{\mathrm{d}\mathbf{y}} \right\| \\
&= \ln \left\| \frac{\mathrm{d}\phi_{T+s}^T(\hat{\mathbf{y}})}{\mathrm{d}\hat{\mathbf{y}}} \right\| + \ln \left\| \frac{\mathrm{d}\phi_0^s(\mathbf{x})}{\mathrm{d}\mathbf{x}} \right\| \leq 2k|s| \ ,
\end{aligned}
$$

where we have used properties of the flow map given in equation (2.5) and the maximum exponential stretching hypothesis of equation (2.12). Similarly,

$$
\begin{aligned}
|T| \left(\sigma_s^T(\mathbf{y}) - \sigma_0^T(\mathbf{x})\right) &= \ln \left\| \frac{\mathrm{d}\phi_s^{s+T}(\mathbf{y})}{\mathrm{d}\mathbf{y}} \right\| - \ln \left\| \frac{\mathrm{d}\phi_0^T(\mathbf{x})}{\mathrm{d}\mathbf{x}} \right\| \\
&= \ln \left\| \frac{\mathrm{d}(\phi_T^{s+T}(\phi_0^T(\phi_s^0(\mathbf{y})))))}{\mathrm{d}\mathbf{y}} \right\| - \ln \left\| \frac{\mathrm{d}(\phi_0^T(\mathbf{x}))}{\mathrm{d}\mathbf{x}} \right\| \\
&= \ln \left\| \frac{\mathrm{d}\phi_T^{s+T}(\hat{\mathbf{x}})}{\mathrm{d}\hat{\mathbf{x}}} \frac{\mathrm{d}\phi_0^T(\mathbf{x})}{\mathrm{d}\mathbf{x}} \frac{\mathrm{d}\phi_s^0(\mathbf{y})}{\mathrm{d}\mathbf{y}} \right\| - \ln \left\| \frac{\mathrm{d}\phi_0^T(\mathbf{x})}{\mathrm{d}\mathbf{x}} \right\| \\
&\leq \ln \left(\left\| \frac{\mathrm{d}\phi_T^{s+T}(\hat{\mathbf{x}})}{\mathrm{d}\hat{\mathbf{x}}} \right\| \left\| \frac{\mathrm{d}\phi_0^T(\mathbf{x})}{\mathrm{d}\mathbf{x}} \right\| \left\| \frac{\mathrm{d}\phi_s^0(\mathbf{y})}{\mathrm{d}\mathbf{y}} \right\| \right) - \ln \left\| \frac{\mathrm{d}\phi_0^T(\mathbf{x})}{\mathrm{d}\mathbf{x}} \right\| \\
&= \ln \left\| \frac{\mathrm{d}\phi_T^{s+T}(\hat{\mathbf{x}})}{\mathrm{d}\hat{\mathbf{x}}} \right\| + \ln \left\| \frac{\mathrm{d}\phi_s^0(\mathbf{y})}{\mathrm{d}\mathbf{y}} \right\| \leq 2k|s| \ ,
\end{aligned}
$$

so we have

$$\left\|\sigma_0^T(\mathbf{x}) - \sigma_s^T(\mathbf{y})\right\| \leq 2k\frac{|s|}{|T|}\ . \tag{2.33}$$

Therefore

$$\left\|\frac{\mathrm{d}\sigma_t^T(\mathbf{x})}{\mathrm{d}t}\right\| = \lim_{s\to 0}\frac{\left\|\sigma_{t+s}^T(\mathbf{y}) - \sigma_t^T(\mathbf{x})\right\|}{|s|} \leq \frac{2k}{|T|} = \mathcal{O}(1/|T|)\ . \tag{2.34}$$

Taking the limit as $|T| \to \infty$ gives

$$\limsup_{|T|\to\infty}\left\|\frac{\mathrm{d}\sigma_t^T(\mathbf{x})}{\mathrm{d}t}\right\| = 0\ , \tag{2.35}$$

which implies

$$\lim_{|T|\to\infty}\left\|\frac{\mathrm{d}\sigma_t^T(\mathbf{x})}{\mathrm{d}t}\right\| = 0\ , \tag{2.36}$$

□

The following corollary provides a bound on the variation of $\nabla\sigma$ in time.

Corollary 2.3.1 *We have*

$$\frac{\partial\nabla\sigma}{\partial t} = -J^*\nabla\sigma - \Sigma\mathbf{v} + \mathcal{O}\left(1/|T|\right), \tag{2.37}$$

where J is the Jacobian matrix of the velocity field $\mathbf{v}$.

Proof. From equation (2.34), the material derivative of σ satisfies

$$\frac{\mathrm{d}}{\mathrm{d}t}\sigma_t^T(\mathbf{x}) = \mathcal{O}\left(1/|T|\right).$$

As a result,

$$\frac{\partial\sigma}{\partial t} = -\left\langle\mathbf{v}, \nabla\sigma\right\rangle + \mathcal{O}\left(1/|T|\right)\ . \tag{2.38}$$

Lemma 2.2.1 guarantees that $\nabla\sigma$ is C^1 in time. Therefore, we have $\left|\frac{\partial\nabla\sigma}{\partial t}\right| < \infty$ and the (spatial) derivative of equation (2.38) yields

$$\nabla\frac{\partial\sigma}{\partial t} = \frac{\partial\nabla\sigma}{\partial t} = -J^*\nabla\sigma - \Sigma\mathbf{v} + \mathcal{O}\left(1/|T|\right)\ , \tag{2.39}$$

□

We will use Corollary 2.3.1 in the next section to derive an estimate for the flux across an LCS. Notice that although Σ is technically a bilinear form, in Cor. 2.3.1 we made use of Riesz's representation theorem and represented Σ as a linear operator by defining $\Sigma\mathbf{u}$ (for any $\mathbf{u}$) as the unique vector that satisfies

$$\left\langle\mathbf{v}, \Sigma\mathbf{u}\right\rangle = \Sigma(\mathbf{v}, \mathbf{u})\ , \tag{2.40}$$

for all $\mathbf{v}$. This will be encountered again for Σ and similar bilinear forms when needed.

2.4 Lagrangian Ridges

The purpose of this section is to derive the flux through an LCS based only on the geometry of the FTLE field and the given dynamical system. To simplify the derivations, in §2.4.1 we define a function $L(\mathbf{x}, t)$ such that the LCS is given by the level set $L(\mathbf{x}, t) = 0$. Some useful properties of $L(\mathbf{x}, t)$ and its derivatives are then derived in §2.4.2, including an expression for $\mathrm{d}L/\mathrm{d}t$ given in equation (2.66). We show that the infinitesimal flux at any point on the LCS is given by

$$\mathrm{d}\Phi = \left.\frac{\mathrm{d}L}{\mathrm{d}t}\right|_{L=0} \mathrm{d}s$$

where $\mathrm{d}s$ is the infinitesimal arc length along the LCS and the right-hand side is to be replaced with equation (2.66), which contains values that can be obtained from the geometry of the FTLE field and the dynamical system. We then analyze and discuss the interpretation of this estimate in §2.4.3.

2.4.1 Representation

Suppose that we are given an FTLE field, $\sigma_t^T(\mathbf{x})$ for $t \in [t_1, t_2]$ that admits an LCS in the sense of Def. 2.2.3. We define a scalar function L of space and time as follows:

Definition 2.4.1 *For every time t, let $L(\mathbf{x}, t)$ be the function of $\mathbf{x} \in D$ defined by the conditions*

1. $|L(\mathbf{x}, t)| = \|\mathbf{x} - \mathbf{x}_q\|$, *where $\mathbf{x}_q$ is the point on the closure of the path representing the LCS closest to the point $\mathbf{x}$,*
2. $L(\mathbf{x}, t)(((\mathbf{x} - \mathbf{x}_q) \times \mathbf{c}_t'(s)) \cdot \hat{\mathbf{k}}) \geq 0$,

where $\hat{\mathbf{k}}$ is the unit basis vector pointing "up" from the domain D. Notice that $L(\mathbf{x}, t)$ simply gives the "signed distance" from $\mathbf{x}$ to the nearest point on the LCS. If moving along the curve $\mathbf{c}(s)$ in the positive $\mathbf{c}'(s)$ direction, then at least locally, points on the right have a positive value of L, and points on the left a negative value. Also note that the LCS is trivially given by the zero set $L = 0$.

2.4.2 Properties

There may exist points in the domain that have multiple possible values for $\mathbf{x_q}$. However, by the following theorem, we can always find an open set, $\mathcal{U}_t$, which contains the LCS and excludes any of these points.

Theorem 2.4.1 *Let $\mathcal{B} \subset D$ be the set of points with non-unique $\mathbf{x}_q$. This set is at a strictly positive distance from $\mathbf{c}(s)$.*

Proof. Since the curve $\mathbf{c}(s)$ is C^2 in s by Theorem 2.2.1, its curvature must remain finite. We will first show that $\mathcal{B}$ must be at a finite distance from $\mathbf{c}(s)$ by contradiction. Suppose that the set $\mathcal{B}$ is not a finite distance from $\mathbf{c}(s)$. In this case, we can find a sequence $\mathbf{x}_n \in \mathcal{B}$ such that $\mathbf{x}_n \to \mathbf{p} \in \mathbf{c}(s)$. By definition of $\mathcal{B}$, for each $\mathbf{x}_n$, there exist at least two points $\mathbf{x}_n^{(1)}$ and $\mathbf{x}_n^{(2)}$ on $\mathbf{c}(s)$ that are equidistant from $\mathbf{x}_n$ and every other point on the LCS is located at the same distance from $\mathbf{x}_n$ as these points or further. Since the curve $\mathbf{c}(s)$ is an injection, there are unique $s_n^{(1)}$ and $s_n^{(2)}$ such that $\mathbf{c}(s_n^{(1)}) = \mathbf{x}_n^{(1)}$ and $\mathbf{c}(s_n^{(2)}) = \mathbf{x}_n^{(2)}$.

Notice that

$$\|\mathbf{x}_n - \mathbf{p}\| \xrightarrow[n\to\infty]{} 0 \tag{2.41}$$

and

$$\left\|\mathbf{x}_n^{(1)} - \mathbf{x}_n\right\| = \left\|\mathbf{x}_n^{(2)} - \mathbf{x}_n\right\| \leq \|\mathbf{p} - \mathbf{x}_n\| \ , \tag{2.42}$$

so we must have

$$\left.\begin{aligned} &\mathbf{x}_n^{(1)} \xrightarrow[n\to\infty]{} \mathbf{p} \ , \\ &\mathbf{x}_n^{(2)} \xrightarrow[n\to\infty]{} \mathbf{p} \ , \\ &\mathbf{x}_n^{(1)} \neq \mathbf{x}_n^{(2)} \ \text{ for all } n \ . \end{aligned}\right\} \tag{2.43}$$

This allows us to define the curvature at $\mathbf{p}$ as the limit of the difference between the normal vectors at points $\mathbf{x}_n^{(1)}$ and $\mathbf{x}_n^{(2)}$. Let us denote by $\hat{\mathbf{n}}_n^{(1)}$ and $\hat{\mathbf{n}}_n^{(2)}$ the unit vectors normal to $\mathbf{c}(s)$ at respectively $\mathbf{x}_n^{(1)}$ and $\mathbf{x}_n^{(2)}$, cf. Figure 2.2(a). The curvature κ is defined as the norm of the derivative with respect to s of the normal vector. From equation (2.43), we get

$$\kappa(\mathbf{p}) = \lim_{n\to\infty} \left\| \frac{\hat{\mathbf{n}}_n^{(2)} - \hat{\mathbf{n}}_n^{(1)}}{s_n^{(2)} - s_n^{(1)}} \right\| \tag{2.44}$$

Since $\kappa(\mathbf{p})$ is bounded, the limit of the right-hand side of equation (2.44) must remain bounded. We will show that if $\mathcal{B}$ is not at a finite distance from $\mathbf{c}(s)$, then this limit goes unbounded, providing the contradiction.

Notice that the points $\mathbf{x}_n^{(1)}$ and $\mathbf{x}_n^{(2)}$ are the points on $\mathbf{c}(s)$ that are the closest to $\mathbf{x}_n$, hence the vectors $\mathbf{x}_n^{(1)} - \mathbf{x}_n$ and $\mathbf{x}_n^{(2)} - \mathbf{x}_n$ must be *tangent* to respectively $\hat{\mathbf{n}}_n^{(1)}$ and $\hat{\mathbf{n}}_n^{(2)}$. Therefore the difference between the normal vectors can be written

$$\left\|\hat{\mathbf{n}}_n^{(2)} - \hat{\mathbf{n}}_n^{(1)}\right\| = \left\| \frac{\mathbf{x}_n^{(2)} - \mathbf{x}_n}{\left\|\mathbf{x}_n^{(2)} - \mathbf{x}_n\right\|} - \frac{\mathbf{x}_n^{(1)} - \mathbf{x}_n}{\left\|\mathbf{x}_n^{(1)} - \mathbf{x}_n\right\|} \right\| = \frac{\left\|\mathbf{x}_n^{(2)} - \mathbf{x}_n^{(1)}\right\|}{\left\|\mathbf{x}_n^{(2)} - \mathbf{x}_n\right\|} \ . \tag{2.45}$$

We also have

$$\|\mathbf{c}'(s_\mathbf{p})\| = \lim_{n\to\infty} \frac{\left\|\mathbf{x}_n^{(2)} - \mathbf{x}_n^{(1)}\right\|}{\left|s_n^{(2)} - s_n^{(1)}\right|} = D_p > 0 \ , \tag{2.46}$$

because the ridge is C^1 and $\mathbf{c}'(s) \neq 0$, so there is an n^* such that for all $n > n^*$,

$$\frac{\left\|\mathbf{x}_n^{(2)} - \mathbf{x}_n^{(1)}\right\|}{\left|s_n^{(2)} - s_n^{(1)}\right|} \geq \frac{D_p}{2} > 0 \,, \tag{2.47}$$

by definition of the limit.

Equations (2.44), (2.45) and (2.47) give

$$\kappa(\mathbf{p}) = \lim_{n\to\infty} \frac{1}{\left\|\mathbf{x}_n^{(2)} - \mathbf{x}_n\right\|} \frac{\left\|\mathbf{x}_n^{(2)} - \mathbf{x}_n^{(1)}\right\|}{\left|s_n^{(2)} - s_n^{(1)}\right|} \geq \frac{D_p}{2} \lim_{n\to\infty} \frac{1}{\left\|\mathbf{x}_n^{(2)} - \mathbf{x}_n\right\|} = +\infty \,, \tag{2.48}$$

which contradicts the fact that $\mathbf{c}(s)$ has a finite curvature at point $\mathbf{p}$. □

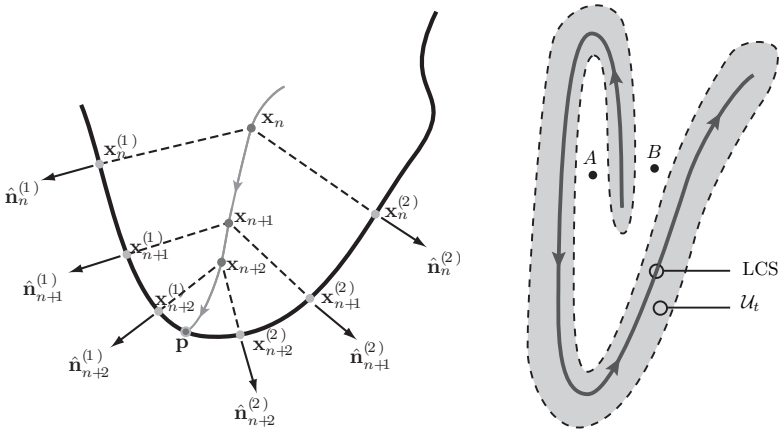

(a) Setting for the proof of Theorem 3.1 (b) Neighborhood $\mathcal{U}_t$ in which L is C^2

Figure 2.2: For an LCS represented as a curve $\mathbf{c}(s)$, we can always find an open set containing it that excludes points of discontinuity of L. In panel (b), notice that even though for points **A** and **B** there are multiple values of $\mathbf{x_q}$ defined, the function $L(x,t)$ is still continuous at point **A**, however ∇L is not continuous at **A**.

The theorem above allows us to define an open set $\mathcal{U}_t$ that completely contains the LCS. The fact that each $\mathbf{x} \in \mathcal{U}_t$ has a unique $\mathbf{x}_q$, allows us to show that the function L must be C^2 on and near the LCS.

Theorem 2.4.2 *$L(x,t)$ is C^2 over the open set $\mathcal{U}_t$.*

Proof. Since

$$L(\mathbf{x},t) = \pm \left\|\mathbf{x} - \mathbf{x}_q\right\| \,, \tag{2.49}$$

we have

$$\nabla L = \frac{\pm 1}{\|\mathbf{x} - \mathbf{x}_q\|} \left\langle I - \frac{d\mathbf{x}_q}{d\mathbf{x}}, \mathbf{x} - \mathbf{x}_q \right\rangle \,. \tag{2.50}$$

However

$$\left\langle \frac{d\mathbf{x}_q}{d\mathbf{x}}, \mathbf{x} - \mathbf{x}_q \right\rangle = 0 \tag{2.51}$$

in $\mathcal{U}_t$ because the closest point on the LCS does not change with variations in the direction normal to the curve. As a result,

$$\nabla L = \frac{\mathbf{x} - \mathbf{x}_q}{\pm \|\mathbf{x} - \mathbf{x}_q\|} = \frac{\mathbf{x} - \mathbf{x}_q}{L} = \hat{\mathbf{n}}(\mathbf{x}, t) \ , \tag{2.52}$$

where we have used the fact that $\mathbf{x}_q$ is the point on the LCS closest to $\mathbf{x}$, hence $\hat{\mathbf{n}}(\mathbf{x}, t)$ must be parallel to $\mathbf{x} - \mathbf{x}_q$. Recall that there is a unique $\mathbf{x}_q$ for each $\mathbf{x} \in \mathcal{U}_t$, by virtue of Theorem 2.4.1. As a result, $\hat{\mathbf{n}}(\mathbf{x}, t)$ is a well-defined function of $\mathbf{x}$. Moreover, $\mathbf{c}(s)$ is C^2 by Theorem 2.2.1. This implies that $\mathbf{c}'(s)$ is C^1, and hence so is $\nabla L = \hat{\mathbf{n}} = \hat{\mathbf{k}} \times \mathbf{c}' / \|\mathbf{c}'\|$ since $\mathbf{c}' \neq 0$.

□

Define the unit vector $\hat{\mathbf{t}}$ orthogonal to $\hat{\mathbf{n}}$ by $\hat{\mathbf{t}} = \hat{\mathbf{k}} \times \hat{\mathbf{n}}$. Notice that $\hat{\mathbf{t}}$ and $\hat{\mathbf{n}}$ are defined everywhere in $\mathcal{U}_t$, not just on the LCS. On the LCS, $\hat{\mathbf{t}}$ and $\hat{\mathbf{n}}$ correspond to, respectively, the tangent and orthogonal directions to the LCS. Therefore, on the LCS, $\hat{\mathbf{t}}$ is parallel to $\nabla\sigma$. But since $\nabla\sigma$ can be oriented either along $\dot{\mathbf{c}}(s)$ or $-\dot{\mathbf{c}}(s)$ and can even vanish, we prefer to use $\hat{\mathbf{t}}$ on the ridge instead of $\nabla\sigma$. Let $\mathcal{L}$ be the Hessian of L and note the following properties of $\mathcal{L}$ and Σ:

Lemma 2.4.1 *Σ and $\mathcal{L}$ are self-adjoint.*

Proof. This result holds due to the symmetry of mixed partials. From $\Sigma(\mathbf{u}, \mathbf{v}) = \Sigma(\mathbf{v}, \mathbf{u})$, we deduce immediately that $\langle \mathbf{u}, \Sigma\mathbf{v} \rangle = \langle \mathbf{v}, \Sigma\mathbf{u} \rangle = \langle \Sigma\mathbf{u}, \mathbf{v} \rangle$ because the derivatives are necessarily real numbers. □

Theorem 2.4.3 *For $L = 0$, we have $\left\langle \hat{\mathbf{t}}, \Sigma\hat{\mathbf{n}} \right\rangle = \left\langle \hat{\mathbf{n}}, \Sigma\hat{\mathbf{t}} \right\rangle = 0$.*

Proof. From Def. 2.2.2, **SR2** implies that $\nabla L = \hat{\mathbf{n}}$ is an eigenvector of Σ. Hence, $\left\langle \hat{\mathbf{t}}, \Sigma\hat{\mathbf{n}} \right\rangle = \lambda_{\min}(\Sigma) \left\langle \hat{\mathbf{t}}, \hat{\mathbf{n}} \right\rangle = 0$, where $\lambda_{\min}(\Sigma)$ is the smallest eigenvalue of Σ. □

Corollary 2.4.1 *For $L = 0$ and an arbitrary vector $\mathbf{v}$, we have $\langle \hat{\mathbf{n}}, \Sigma\mathbf{v} \rangle = \langle \hat{\mathbf{n}}, \Sigma\hat{\mathbf{n}} \rangle \langle \hat{\mathbf{n}}, \mathbf{v} \rangle$.*

Proof. Developing $\mathbf{v}$ in the orthonormal basis $(\hat{\mathbf{t}}, \hat{\mathbf{n}})$ gives

$$\mathbf{v} = \left\langle \hat{\mathbf{t}}, \mathbf{v} \right\rangle \hat{\mathbf{t}} + \langle \hat{\mathbf{n}}, \mathbf{v} \rangle \hat{\mathbf{n}} \ . \tag{2.53}$$

Computing $\langle \hat{\mathbf{n}}, \Sigma\mathbf{v} \rangle$ in this basis and applying Theorem 2.4.3 gives the desired result.

□

Lemma 2.4.2 *$\mathcal{L}\hat{\mathbf{n}} = 0$ everywhere in $\mathcal{U}_t$.*

Proof. Everywhere in $\mathcal{U}_t$, L is C^2, so the gradient ∇L exists and is differentiable. In particular, $\|\nabla L\| = 1$, therefore

$$0 = \nabla \left(\|\nabla L\|^2 \right) = 2\, \mathcal{L} \nabla L = 2\, \mathcal{L} \hat{\mathbf{n}} \,. \tag{2.54}$$

□

Lemma 2.4.3 *On the LCS, i.e., for $L = 0$,*

$$\langle \hat{\mathbf{n}}, \Sigma \hat{\mathbf{n}} \rangle \frac{\partial L}{\partial t} = \frac{\partial \langle \hat{\mathbf{n}}, \nabla \sigma \rangle}{\partial t} \,. \tag{2.55}$$

Proof. Take $\mathbf{x}$ on the LCS at time t, i.e., $L(\mathbf{x}, t) = 0$. Define $\mathbf{y} = \mathbf{x} + \alpha(\delta t)\hat{\mathbf{n}}$ such that $L(\mathbf{y}, t+\delta t) = 0$. In other words, $\mathbf{y}$ is at the intersection of the LCS at time $t+\delta t$ and the line starting at $\mathbf{x}$, orthogonal to the LCS at time t (see Figure 2.3). Since we require $\mathbf{y} = \mathbf{x}$ for $\delta t = 0$, it follows that $\alpha(\delta t)$ is $\mathcal{O}(\delta t)$. Expanding L to second order in δt gives the following (where all derivatives on the right-hand side of equations (2.56)–(2.64) are evaluated at $\mathbf{x}$ and t unless otherwise specified):

$$0 = L(\mathbf{y}, t + \delta t) = L(\mathbf{x}, t) + \alpha + \frac{\partial L}{\partial t}\delta t + \mathcal{O}(\delta t^2) \,, \tag{2.56}$$

$$= \alpha + \frac{\partial L}{\partial t}\delta t + \mathcal{O}(\delta t^2) \,. \tag{2.57}$$

Therefore,

$$\alpha = -\frac{\partial L}{\partial t}\delta t + \mathcal{O}(\delta t^2) \,. \tag{2.58}$$

Now expanding ∇L, and plugging in Lemma 2.4.2, gives

$$\nabla L|_{\mathbf{y}, t+\delta t} = \nabla L + \frac{\partial \nabla L}{\partial t}\delta t + \mathcal{O}(\delta t^2) \,. \tag{2.59}$$

Taylor expanding $\nabla \sigma|_{\mathbf{y}, t+\delta t}$ gives

$$\nabla \sigma|_{\mathbf{y}, t+\delta t} = \nabla \sigma + \alpha \Sigma \hat{\mathbf{n}} + \frac{\partial \nabla \sigma}{\partial t}\delta t + \mathcal{O}(\delta t^2) \,. \tag{2.60}$$

From equations (2.52) and (2.58) we have

$$\nabla \sigma|_{\mathbf{y}, t+\delta t} = \nabla \sigma - \frac{\partial L}{\partial t}\Sigma \nabla L \delta t + \frac{\partial \nabla \sigma}{\partial t}\delta t + \mathcal{O}(\delta t^2) \,. \tag{2.61}$$

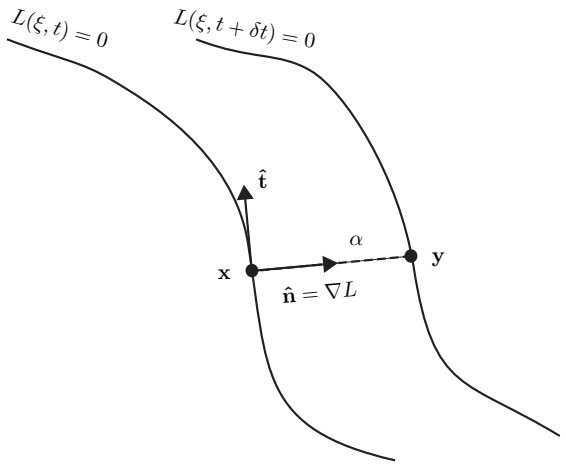

Figure 2.3: Geometry of quantities discussed in Lemma 2.4.3.

Since $\mathbf{y}$ is on the LCS at time $t+\delta t$, we must have

$$\begin{aligned} 0 &= \left\langle \nabla L|_{\mathbf{y},t+\delta t}\,,\, \nabla\sigma|_{\mathbf{y},t+\delta t} \right\rangle && (2.62)\\ &= \langle \nabla L, \nabla\sigma\rangle + \delta t\left(-\frac{\partial L}{\partial t}\langle \nabla L, \Sigma\nabla L\rangle + \frac{\partial\langle \nabla L,\nabla\sigma\rangle}{\partial t}\right) + \mathcal{O}(\delta t^2) && (2.63)\\ &= \delta t\left(-\langle \hat{\mathbf{n}},\Sigma\hat{\mathbf{n}}\rangle\frac{\partial L}{\partial t} + \frac{\partial\langle \hat{\mathbf{n}},\nabla\sigma\rangle}{\partial t}\right) + \mathcal{O}(\delta t^2)\,. && (2.64)\end{aligned}$$

Hence, we get the desired result, since δt is arbitrary. □

As stated above, and derived in the next section, the flux over the LCS, i.e., the level set $L=0$, is given by

$$\Phi(t) = \int_{\mathrm{LCS}} \frac{\mathrm{d}L}{\mathrm{d}t}\,\mathrm{d}s\,, \tag{2.65}$$

The next theorem contains an expression for $\mathrm{d}L/\mathrm{d}t$ based on quantities defining the FTLE and velocity fields.

Theorem 2.4.4 *For $L=0$, we have*

$$\frac{\mathrm{d}L}{\mathrm{d}t} = \frac{\langle \hat{\mathbf{t}},\nabla\sigma\rangle}{\langle \hat{\mathbf{n}},\Sigma\hat{\mathbf{n}}\rangle}\left\langle \hat{\mathbf{t}}, \frac{\partial\hat{\mathbf{n}}}{\partial t} - J\hat{\mathbf{n}}\right\rangle + \mathcal{O}\left(1/|T|\right)\,. \tag{2.66}$$

Proof. Lemma 2.4.3 gives

$$\langle \hat{\mathbf{n}},\Sigma\hat{\mathbf{n}}\rangle\frac{\mathrm{d}L}{\mathrm{d}t} = \frac{\partial\langle \hat{\mathbf{n}},\nabla\sigma\rangle}{\partial t} + \langle \hat{\mathbf{n}},\Sigma\hat{\mathbf{n}}\rangle\langle \hat{\mathbf{n}},\mathbf{v}\rangle\,. \tag{2.67}$$

Applying Cor. 2.4.1 and the chain rule for the derivative gives

$$\langle \hat{\mathbf{n}},\Sigma\hat{\mathbf{n}}\rangle\frac{\mathrm{d}L}{\mathrm{d}t} = \left\langle \nabla\sigma, \frac{\partial\hat{\mathbf{n}}}{\partial t}\right\rangle + \left\langle \hat{\mathbf{n}}, \frac{\partial\nabla\sigma}{\partial t}\right\rangle + \langle \hat{\mathbf{n}},\Sigma\mathbf{v}\rangle\,. \tag{2.68}$$

Using Cor. 2.3.1 in equation (2.68) gives

$$\langle \hat{\mathbf{n}}, \Sigma\hat{\mathbf{n}} \rangle \frac{\mathrm{d}L}{\mathrm{d}t} = \left\langle \nabla\sigma, \frac{\partial \hat{\mathbf{n}}}{\partial t} - J\hat{\mathbf{n}} \right\rangle + \mathcal{O}\left(1/|T|\right) \tag{2.69}$$

and the result follows by noticing that for $L = 0$, $\hat{\mathbf{t}}$ is proportional to $\nabla\sigma$, hence $\nabla\sigma = \langle \hat{\mathbf{t}}, \nabla\sigma \rangle \hat{\mathbf{t}}$. □

2.4.3 Analysis

Now we are in the position to analyze the flux across the LCS. Recall that

$$L(\mathbf{x}(t), t) = \pm \|\mathbf{x}(t) - \mathbf{x}_q(\mathbf{x}(t), t)\| \,,$$

where we have indicated the explicit functional dependencies of each variable. Therefore we have

$$\frac{\mathrm{d}L}{\mathrm{d}t} = \frac{\partial L}{\partial \mathbf{x}} \cdot \frac{\mathrm{d}\mathbf{x}}{\mathrm{d}t} + \frac{\partial L}{\partial \mathbf{x_q}} \cdot \frac{\mathrm{d}\mathbf{x}_q}{\mathrm{d}t} \,. \tag{2.70}$$

However,

$$\frac{\partial L}{\partial \mathbf{x_q}} = \frac{\mathbf{x}_q - \mathbf{x}}{L} = -\nabla L \,,$$

and so

$$\frac{\mathrm{d}L}{\mathrm{d}t} = \nabla L \cdot \left(\frac{\mathrm{d}\mathbf{x}}{\mathrm{d}t} - \frac{\mathrm{d}\mathbf{x}_q}{\mathrm{d}t} \right) \,. \tag{2.71}$$

On the LCS, the two points $\mathbf{x}$ and $\mathbf{x}_q$ are equal; however, we think of $\mathbf{x}$ as being a *Lagrangian*, or material, point while $\mathbf{x}_q$ is viewed as a point that moves with the LCS. Notice the right-hand side of equation (2.71) represents the difference in the velocity of the two points, projected in the direction normal to the LCS. This projected difference in velocities is precisely what contributes to particles crossing the LCS. Therefore, the total flux across the LCS is given by

$$\Phi(t) = \int_{\mathrm{LCS}} \frac{\mathrm{d}L}{\mathrm{d}t} \, \mathrm{d}s \,, \tag{2.72}$$

where the integral is taken over the length of the LCS. Of course $\mathrm{d}L/\mathrm{d}t$, which is not directly obtainable, is to be replaced by its value given in equation (2.66), which can be computed from the FTLE field. If we normalize by the length of the LCS, we can define the *average escape rate* as

$$\eta(t) = \frac{\Phi(t)}{\int_{\mathrm{LCS}} \mathrm{d}s}. \tag{2.73}$$

Now we analyze the terms in the right-hand side of equation (2.66), starting first with the factor

$$\frac{\langle \hat{\mathbf{t}}, \nabla\sigma \rangle}{\langle \hat{\mathbf{n}}, \Sigma\hat{\mathbf{n}} \rangle} \,. \tag{2.74}$$

Recall that all terms in equation (2.66) are evaluated along the LCS. The numerator of equation (2.74) can be re-written as $\left\langle \hat{\mathbf{t}}, \nabla\sigma \right\rangle = \|\nabla\sigma\|$. For time-independent flows, σ is constant along trajectories (asymptotically). Hence for any ridge in the FTLE field, $\nabla\sigma = 0$ along the ridge, and therefore the flux is zero. This is expected since for time-independent flows, streamlines and trajectories coincide. Experience dictates that even for highly time-dependent flows the value of σ does not vary much along ridges in the FTLE field and hence we can expect this term typically to be quite small. More precisely though, taking the derivative in the orthogonal direction (i.e, $\langle \hat{\mathbf{n}}, \nabla\|\nabla\sigma\| \rangle$) reveals that the numerator in equation (2.74) is indeed a minimum on the LCS.

Referring to Def. 2.2.2, we notice that the denominator of equation (2.74) is less than zero and is locally minimized (i.e., its norm is maximized). Therefore, for a well-defined ridge, we expect the magnitude of this term to be large, with a larger value the sharper the ridge. Since the numerator of equation (2.74) is locally minimized and the magnitude of the denominator is locally maximized, this implies that the magnitude of the factor given in equation (2.74) is locally minimized in the direction normal to the LCS, hence this multiplying factor is expected to be small for well-defined ridges.

Now consider the term

$$\left\langle \hat{\mathbf{t}}, \frac{\partial \hat{\mathbf{n}}}{\partial t} - J\hat{\mathbf{n}} \right\rangle \tag{2.75}$$

from equation (2.66). The quantity $\left\langle \hat{\mathbf{t}}, \frac{\partial \hat{\mathbf{n}}}{\partial t} \right\rangle$ represents how fast the LCS is locally rotating, which we think of as a *Lagrangian* rotation. This is easily seen since for an appropriate θ, we can write $\hat{\mathbf{n}} = (\cos\theta,\ \sin\theta)$ and $\hat{\mathbf{t}} = (-\sin\theta,\ \cos\theta)$ so

$$\left\langle \hat{\mathbf{t}}, \frac{\partial \hat{\mathbf{n}}}{\partial t} \right\rangle = \begin{bmatrix} -\sin\theta & \cos\theta \end{bmatrix} \begin{bmatrix} -\dot{\theta}\sin\theta \\ \dot{\theta}\cos\theta \end{bmatrix} = \dot{\theta}\ ,$$

which is the local rotation rate of the LCS. Now notice $J\hat{\mathbf{n}}$ is the linearized velocity field applied to a unit vector normal to the LCS; and taking the inner product of this with the tangent to the LCS, $\hat{\mathbf{t}}$, gives the component in the direction of the LCS. That is, the term $\left\langle \hat{\mathbf{t}}, J\hat{\mathbf{n}} \right\rangle$ measures how much the local Eulerian field rotates vectors normal to the LCS. We therefore view this term as a local *Eulerian* rotation rate and hence equation (2.75) is a local measure of *the difference in the rotation rate of the LCS from the rotation rate induced by the (instantaneous) velocity field.*

If the linearized flow about the LCS turns at a sufficiently uniform speed, then the LCS will follow that rotation. On the other hand, if there is a sudden increase or decrease of the local vorticity in the field (i.e., a short-term error or a short-term vortex), the LCS may become less Lagrangian. In the second example studied below, we extract a strong LCS from high-frequency radar data near the coast of Florida. Small vortices in the domain can be observed and eventually degrade the LCS, as observed by Lekien et al. [48].

The last term in the right-hand side of equation (2.66) scales inversely to the integration time. Notice, that if $T \to 0$, then the FTLE is an instantaneous, or Eulerian, measure of separation, which is often not very enlightening for aperiodic systems [29]. However, for T finite, we obtain a Lagrangian measure of separation because the FTLE considers the integrated effect of the flow over the interval T. Thus the $\mathcal{O}(1/T)$ term in equation (2.66), which states that the LCS becomes more Lagrangian as T increases should seem reasonable. However, it is important to keep in mind that, based on the time-scales of the system dynamics, ridges in the FTLE field can become more or less pronounced as T increases; that is, the term given by equation (2.74) can become smaller *or* larger as T increases even though the $\mathcal{O}(1/T)$ term in equation (2.66) is tending to zero. This is because for aperiodic flows, strongly hyperbolic lines can lose their hyperbolicity as time evolves; or restating, some LCS exist only over strictly finite-time intervals. So for example, as T initially is increased a ridge (LCS) in the FTLE field may sharpen, but as T extends beyond the interval of existence of the LCS, the ridge may disappear. Ch. 4 discusses the effects of choosing an appropriate T.

Notice that $\hat{\mathbf{t}} \cdot \nabla\sigma$ is used in equation (2.66) instead of equivalently using $\|\nabla\sigma\|$. This is for numerical purposes. The norm of the gradient can increase rapidly if we are slightly off the ridge because the curvature has been maximized, so $\hat{\mathbf{t}} \cdot \nabla\sigma$ should be less sensitive to numerical errors on the position of the ridge. In the next two sections, the flux estimate of equation (2.66) are tested on two examples.

2.5 Example 1: Analytical Model of a Double-Gyre Flow

In this section we apply some of the preceding results to a periodically varying double-gyre. This flow is described by the stream-function

$$\psi(x, y, t) = A \sin(\pi f(x, t)) \sin(\pi y) \ , \tag{2.76}$$

where

$$\begin{aligned} f(x,t) &= a(t)x^2 + b(t)x \\ a(t) &= \epsilon \sin(\omega t) \\ b(t) &= 1 - 2\epsilon \sin(\omega t) \end{aligned} \tag{2.77}$$

over the domain $[0, 2] \times [0, 1]$. This model should not be seen as the approximate solution to a real fluid flow, but rather a simplification of a double-gyre pattern that occurs frequently in geophysical flows [14]. The analytical form of equation (2.77) were chosen to produce a simple time-dependent flow with fixed boundaries, not to approach a solution of Navier-Stokes' equation.

The velocity field is given by

$$u = -\frac{\partial \psi}{\partial y} = -\pi A \sin(\pi f(x)) \cos(\pi y) \ , \tag{2.78}$$

$$v = \frac{\partial \psi}{\partial x} = \pi A \cos(\pi f(x)) \sin(\pi y) \frac{\mathrm{d}f}{\mathrm{d}x} \ . \tag{2.79}$$

For $\epsilon = 0$ the flow is time-independent and has the same pattern as Figure 2.4(a). However, for $\epsilon \neq 0$ the flow is time-dependent and the gyres conversely expand and contract periodically in the x-direction such that the rectangle enclosing the gyres remains invariant. In equation (2.76), A determines the magnitude of the velocity vectors, $\omega/2\pi$ is the frequency of oscillation, and ϵ is *approximately* how far the line separating the gyres moves to the left or right, that is, the amplitude of the motion of the separation point $\tilde{x}$ on the x axis about the point $(1, 0)$ is

$$\begin{aligned} \tilde{x} - 1 &= \frac{\sqrt{1 + 4\epsilon^2 \sin^2(\omega t)} - 1}{2\epsilon \sin(\omega t)} \\ &\approx \frac{1 + 2\epsilon^2 \sin^2(\omega t) - 1}{2\epsilon \sin(\omega t)} \ , \text{ for small } \epsilon \\ &= \epsilon \sin(\omega t) \ . \end{aligned} \tag{2.80}$$

Figure 2.4 shows the velocity field of the periodic double-gyre at various times for $A = 0.1$, $\omega = 2\pi$, and $\epsilon = 0.25$. Notice that the period of motion is equal to 1 for this case, hence at time 0 both gyres are equal in size, at time 0.25 the line separating the gyres is offset furthest to the right a distance $\approx \epsilon$, at time 0.5 the line has returned to the middle, at time 0.75 the line is offset furthest to the left a distance $\approx \epsilon$, and at time 1 the velocity field completes one period.

For $\epsilon = 0$ the system can be thought of as a time-independent 2-D Hamiltonian system. For this case there is a heteroclinic connection of the unstable manifold of the fixed point $(1, 1)$ with the stable manifold of the fixed point $(1, 0)$. The FTLE field for the double-gyre flow is shown in Figure 2.5(a) for $\epsilon = 0$. The LCS, given by the red line of high FTLE, represents this heteroclinic connection, which in this case is an invariant manifold.

For $\epsilon \neq 0$, but small, we can think of the system as perturbed from the time-independent case. We might expect this perturbation to cause a classic entanglement of the unstable and stable manifolds [28]. This is exactly what is indicated by the plot of the FTLE field for the system with $\epsilon = 0.25$, which is shown in Figure 2.5(b) for $T > 0$ and Figure 2.5(c) for $T < 0$. For Figure 2.5(b), there is an LCS that extends from the bottom of the domain and loops back and forth near the top. The integration time used for Figure 2.5(b) was $T = 1.5$ periods. If the integration is extended in time, further looping would be revealed, cf. §4.2. For Figure 2.5(c) an LCS extending from the top of the domain and analogously looping back and forth near the bottom of the domain. The intersection of these LCS gives the classic entanglement geometry that is well-documented in the dynamical

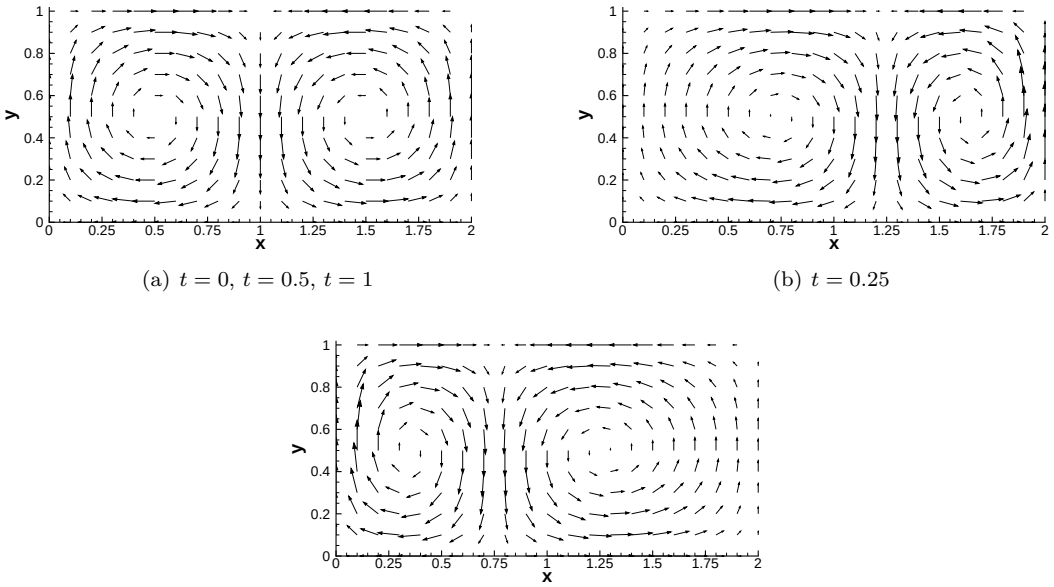

(a) $t = 0$, $t = 0.5$, $t = 1$

(b) $t = 0.25$

(c) $t = 0.75$

Figure 2.4: The double-gyre velocity field for $A = 0.1$, $\omega = 2\pi$, and $\epsilon = 0.25$ at several different times.

systems literature for perturbed Hamiltonian systems. It should be noted that Figures 2.5(b) and (c) shows FTLE computed from the flow map and not for a Poincaré map.

An interesting observation is that from viewing the Eulerian velocity field in Figure 2.4 it appears that the flow is separating at the coordinate $(1, 1)$ at time $t = 0$. However, from inspection of the LCS shown in Figure 2.5(c) it is clear that separation is occurring closer to the coordinate $(0.9, 1)$. This motivates the shortcomings of the Eulerian perspective for interpreting unsteady flows.

2.5.1 Flux over the LCS

Here we show that the LCS in Figure 2.5(b) is indeed nearly Lagrangian. In Figure 2.6(a) we have highlighted the LCS shown in the FTLE field of Figure 2.5(b) and used an **X** to represent a Lagrangian tracer, which is located on the LCS at time $t = 0$. Figures 2.6(b), (c), and (d) show the location of the LCS and the tracer at later times. From this plot, the LCS is indistinguishably Lagrangian, that is, the tracer seems to move perfectly *along* the structure. However, if we refine the calculation, and take a closer look, we can see that there is a very slight flux across the LCS.

Figure 2.7 shows a highly refined computation of the LCS and the location of the Lagrangian tracer. The grid spacing that was used for the computation of FTLE was 1×10^{-5}. Computations reveal that the tracer moves at an average rate of 5×10^{-5} normal to the LCS over the interval considered. This rate is about 0.05% of the magnitude of the velocity field in that region. It is important to note that this rate persists with further refinement of the computational mesh.

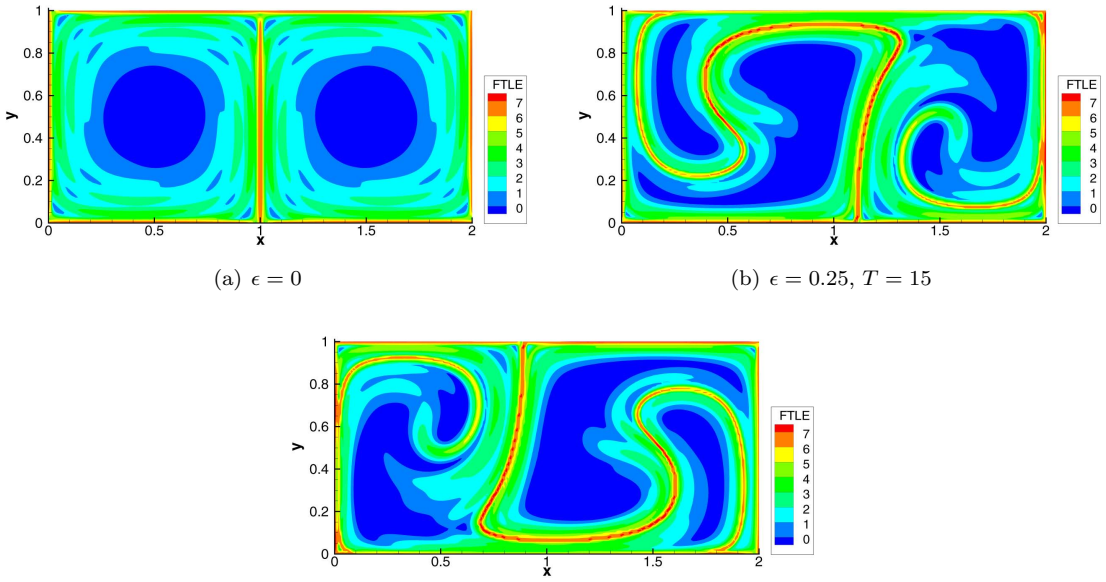

(a) $\epsilon = 0$

(b) $\epsilon = 0.25$, $T = 15$

(c) $\epsilon = 0.25$, $T = -15$

Figure 2.5: FTLE plots for the double-gyre flow for $t = 0$. In both cases, $A = 0.1$. For the time-dependent cases, shown in panel (b) and (c), $\omega = 2\pi/10$.

To verify Theorem 2.4.4, the terms in the right-hand side of equation (2.66) were computed from a first-order approximation. The $\mathcal{O}(1/T)$ term dominates for this example with $1/T \approx 0.03$. This confirms equation (2.66) since the "directly computed" flux of 5×10^{-5} is well below $\mathcal{O}(1/T)$.

2.6 Example 2: VHF Radar Data off the Coast of Florida

High-resolution ocean velocity data has become readily available since the introduction of Very High Frequency (VHF) radar technology. In this section, we use data collected along the Florida coast to compute the FTLE field and extract the LCS in this area. To validate Theorem 2.4.4, we compute the flux across the LCS using both a direct computation and an evaluation of the flux given in equation (2.66). We show that the rate at which particles cross the LCS is less than 0.05% of the average magnitude of the velocity field in the region. This confirms Theorem 2.4.4 and validates the fact that ridges in the FTLE field (that reveal the Lagrangian behavior of the flow) are also Lagrangian (i.e., their motion obeys the equation of motion of the fluid).

2.6.1 Very High Frequency Radar Data

The use of radio frequencies to measure ocean surface currents has received attention in recent coastal oceanographic experiments [103, 80]. The Ocean Surface Current Radar (OSCR) VHF system was deployed for the Southern Florida Ocean Measurement Center (SFOMC) Four-Dimensional

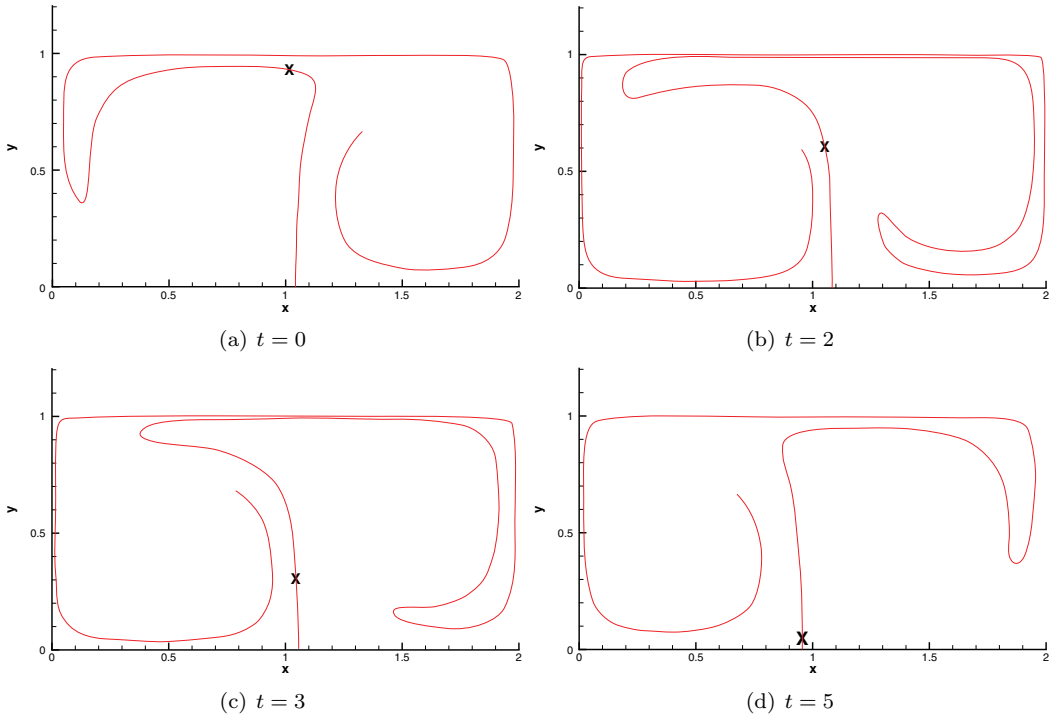

(a) $t = 0$ (b) $t = 2$

(c) $t = 3$ (d) $t = 5$

Figure 2.6: Locations of the LCS and the Lagrangian tracer at four different times. The tracer is denoted by the **X** (Computed with $A = 0.1$, $\omega = 2\pi/10$, $\epsilon = 0.1$ and $T = 15$).

Current Experiment from June 25 through August 25, 1999. Recent observations of surface currents from OSCR using the VHF mode reveal complex flow patterns in this region. More details about the experimental setting and observations can be found in [97, 96]. Data from the OSCR system represents coastal surface currents mapped over a 7 km $\times$ 8.5 km domain at 20-minute intervals with a horizontal resolution of 250 m at 700 grid points. The map for July 22, 1999, 12:00 GMT can be found on panel (a) of Figure 2.8.

2.6.2 Finite-Time Lyapunov Exponents and LCS

To compute the FTLE field using the VHF radar data, a uniform grid of 800 $\times$ 800 particles was used. The FTLE map for July 22, 1999, 12:00 GMT can be found in panel (b) of Figure 2.8. The Florida coastline is located on the left and shaded green. The area shaded blue represents regions of low FTLE and the red represents high FTLE.

Notice that the domain depicted in Figure 2.8 has an open-boundary. The computation of trajectories must be stopped if they exit the domain since velocity data does not extend through this region, and extrapolation would not be meaningful. Such trajectories are disregarded *when* they exit the domain and the FTLE is computed with a smaller integration time, equal to the time at which the trajectory exited.

There is a noticeable ridge of high FTLE in Figure 2.8(b) that encapsulates an LCS. Analysis

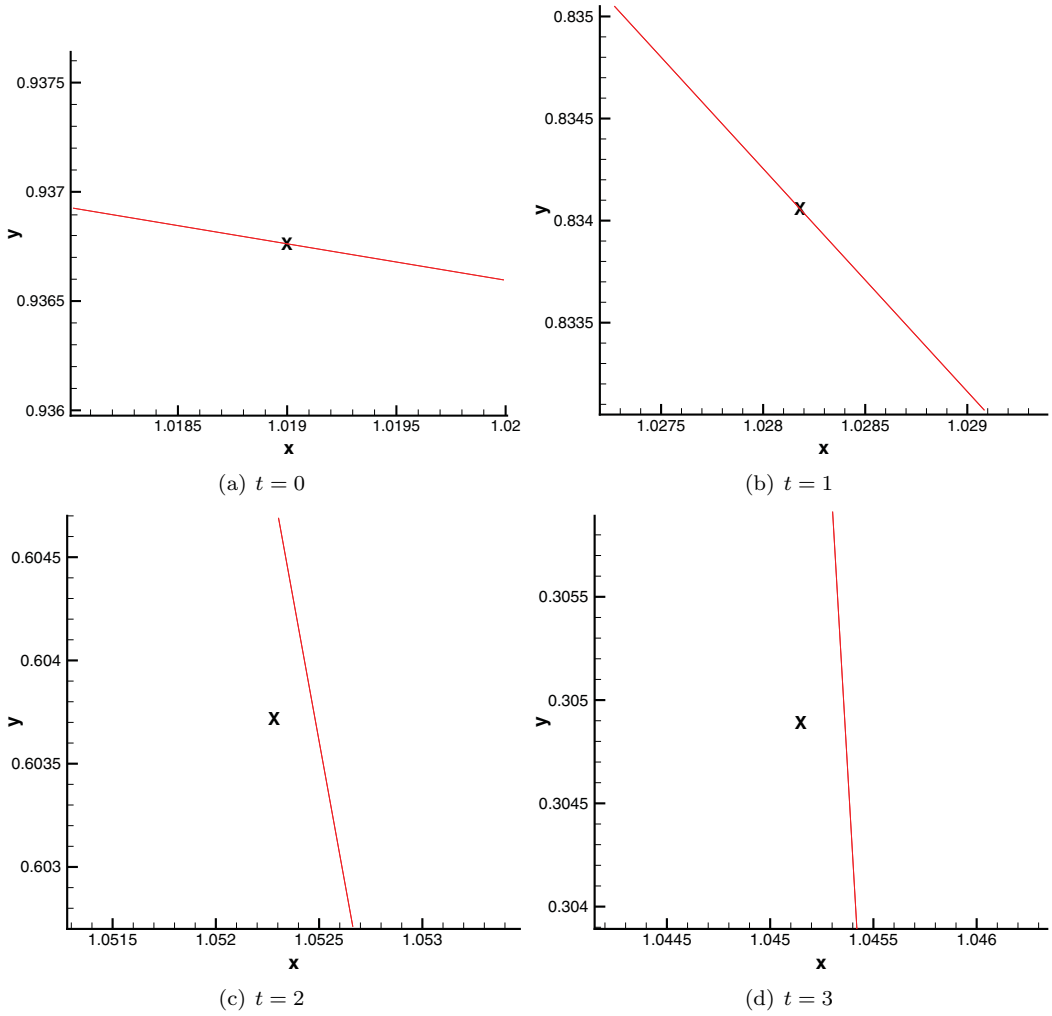

(a) $t = 0$ (b) $t = 1$

(c) $t = 2$ (d) $t = 3$

Figure 2.7: Highly refined plots of the locations of the LCS and the Lagrangian tracer at four different times. (Computed with $A = 0.1$, $\omega = 2\pi/10$, $\epsilon = 0.1$, $T = 30$, and a grid spacing for FTLE computations of 10^{-5}.)

of the motion of fluid parcels [48] reveals that any particle northeast of this structure is flushed out of the domain in only a few hours. In contrast, parcels starting southwest of the structure typically re-circulate several times near the Florida coast before they finally rejoin the current. Interestingly, this unique behavior is not obvious from a simple observation of the velocity footprints, which are typically not very revealing for flows with general time-dependence. However, the Lagrangian footprint of the LCS easily exposes this behavior.

2.6.3 LCS Flux

The objective of this section is to show that for typical coastal flows, such as the one studied here, ridges of the FTLE field are nearly Lagrangian. For this purpose we computed the FTLE field at several instances in time (Figure 2.9). Figure 2.10(a) shows the LCS extracted from the FTLE shown

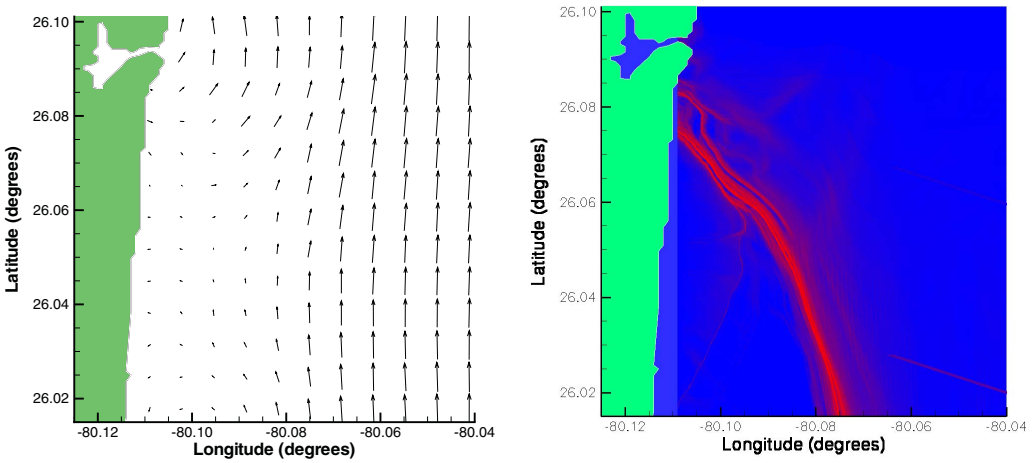

(a) Velocity field

(b) FTLE field

Figure 2.8: Panel (a) shows a vector plot of the velocity field off the Florida coast as observed by the OSCR VHF system on July 22, 1999, 12:00 GMT. Panel (b) shows the FTLE field for July 22, 1999, 12:00 GMT, computed from OSCR data.

in Figure 2.9 at several 30-minute time steps starting with July 22, 1999, 12:00 GMT. Each curve corresponds to the ridge $\mathbf{c}_{t_0+\tau}(s)$ extracted from the field $\sigma^T_{t_0+\tau}(\mathbf{x})$, where $T = 25$ hours is constant, t_0 is set to July 22, 1999, 12:00 GMT and τ increases from zero by increments of 30 minutes. Our goal is to show that $\mathbf{c}_{t_0+\tau}(s)$ is nearly identical to the integration *of the material line* $\mathbf{c}_{t_0}(s)$ from t_0 to $t_0 + \tau$.

Panel (a) of Figure 2.11 shows a close-up of the successive locations of the LCS and the corresponding locations of the integrated material curve. To the naked eye, the LCS behaves as a Lagrangian line. A slight deviation can be noticed after about three hours, but it is not possible to tell from this analysis if that discrepancy is due to numerical error or is inherent.

To give a more definitive and qualitative result, and to verify Theorem 2.4.4, we need to compute the flux, or crossing rate, across the LCS. This is done "directly" by approximating the projected difference in velocity between the LCS and the material line using finite differencing. In other words, the LCS is computed for several times $t = t_0 + k\delta t$. In addition, we integrate the LCS computed at time t_0 from t_0 to t as if it were a line of fluid particles. The difference between the LCS at time t and the integrated line of fluid particles from t_0 to t gives the average flux between t_0 and t, where $t - t_0$ is the averaging time. As the averaging time goes to zero, i.e., $t \to t_0$, we expect the measured average flux to converge toward its instantaneous value $\Phi(t)$. The results of these computations are shown in Figure 2.10(b) and Figure 2.11(b).

Panel (b) of Figure 2.10 shows the distribution of the crossing rate along the LCS computed for July 22, 1999, 12:00 GMT. The bars and red line in Panel (b) of Figure 2.11 represent the computed rate at which particles cross the LCS as a function of the averaging time. One can see that as the

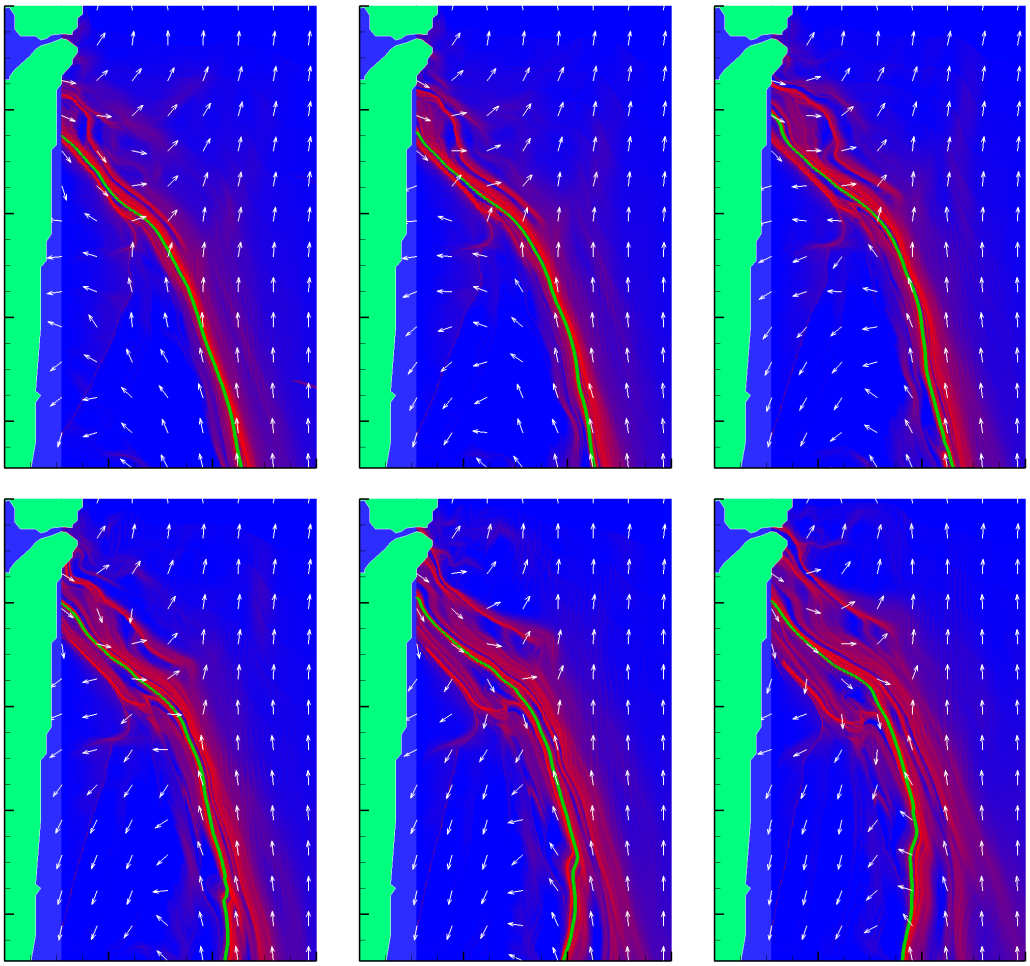

Figure 2.9: From left to right and from top to bottom, FTLE field and LCS on July 22, 12:00 GMT, 12:30 GMT, 13:00 GMT, 13:30 GMT, 14:00 GMT, and 14:30 GMT. Superimposed on each plot is the Eulerian velocity field (using the same length for each vector) at the corresponding time. Figure 2.10(a) shows these six LCS superimposed on a single frame.

averaging time goes to zero, the rate converges to about 0.01 cm s^{-1}. The typical velocity of fluid particles is about 0.05 degrees min^{-1} or 30 cm s^{-1} in the vicinity of the LCS [75, 96, 48]. Therefore, the maximum compound flux along the LCS is less than 0.05% of the average speed of the flow in that region.

In addition to computing the flux directly, we evaluated the first-order term given by equation (2.66). This value is referred to as the "theoretical limit" on Panel (b) of Figure 2.11. Notice that the theoretical limit is very close to the limit of the average flux for $t \to t_0$. This suggests that the integration time T is long enough for the term $\mathcal{O}(1/|T|)$ in equation (2.66) to be negligible.

As an example of how short-term vorticity can break down LCS, we note that during the SFOMC experiment surface current observations revealed Florida Current intrusions over the shelf break, wavelike structures along the inshore edge of the current, and numerous sub-mesoscale vortices [96].

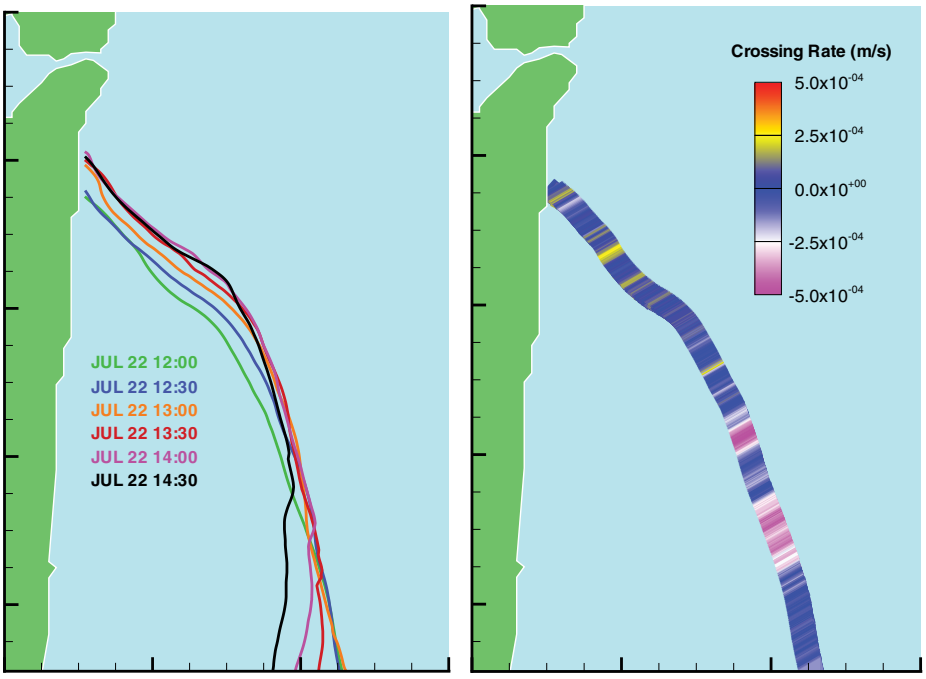

(a) LCS at 30 minute intervals (b) Crossing rate

Figure 2.10: Panel (a) superimposes the locations of the LCS at six different times, spaced every 30 minutes. Panel (b) shows the instantaneous crossing rate along the LCS at July 22, 1999 12:00 GMT.

One example started at 01:20 GMT on June 26, 1999, when a sub-mesoscale vortex was located along the southern part of the VHF-radar domain just inshore of the Florida Current. Surface currents within the vortex ranged from 20–30 cm s^{-1} at a diameter of about 1–1.25 km from the vortex's center. The vortex's northward displacement of about 6 km occurred over a 5–hr period. While there is a continuous presence of distinct, slowly-rotating LCS in the domain, the eddies moving north collide with the structures and eventually break them down by adding local vorticity [48].

2.7 Conclusions

The precise definition of LCS presented in this chapter is based on an idea proposed by Haller [30, 32]. Although FTLE has previously been used to extract LCS in the study of various dynamical systems [76, 77, 109, 110, 48, 38], a refined definition was needed to provide a more rigorous framework for the study of the Lagrangian properties. The definition presented in this chapter allows for the analysis and proof of Lagrangian properties, and supports the computation and numerical extraction of LCS from data sets.

An expression for the flux over an LCS was derived in Theorem 2.4.4, for which it was shown that for well-defined LCS, or those able to rotate with the local Eulerian field, there is a negligible

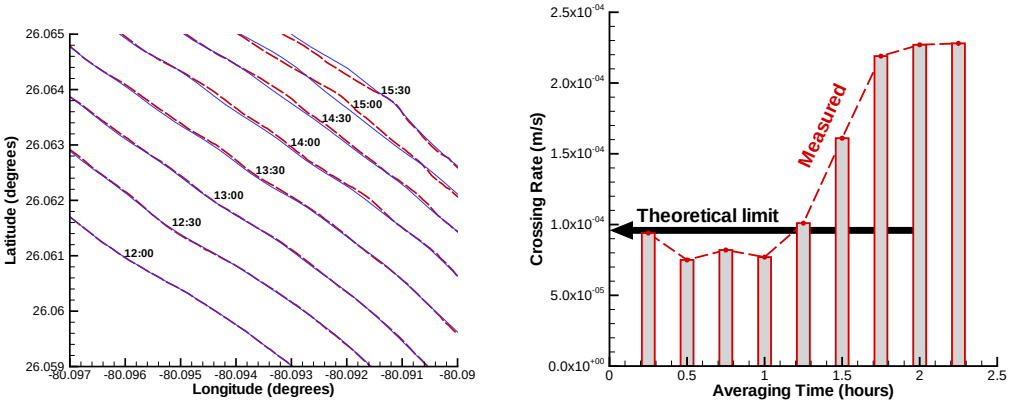

(a) LCS and material line at 30 minute intervals

(b) Crossing rate averaged over time

Figure 2.11: Panel (a) shows a comparison between the location of the LCS, $\mathbf{c}_{t+\tau}(s)$ at different increments of times, τ, (solid blue curves) with the location of the advected material line, which initially corresponds to $\mathbf{c}_t(s)$ (dashed red curves). Panel (b) shows the average crossing rate along the LCS as a function of time; notice that the limiting value for the flux is 10^{-4} m/s.

amount of flux, which is inversely proportional to the integration time of the FTLE.

The theoretical results presented in this chapter were verified for two applications: an analytical double-gyre and observational data of surface currents off the coast of Florida. In both examples, the flux across the LCS was less than 0.05% of the average magnitude of the velocity field near the LCS. These examples re-affirmed that ridges in the FTLE field, i.e., LCS, are indeed Lagrangian.

Acknowledgments

The work presented in this chapter has profited from the motivation and support of the Adaptive Ocean Sampling Network (AOSN) team as well as the Adaptive Sampling and Prediction (ASAP) team. In particular, Chad Coulliette participated in earlier work to compute and observe LCS in oceanographic data.

The high-frequency radar data used was collected by the Rosentiel School of Marine and Atmospheric Science (RSMAS) at the University of Miami. The authors are grateful to Arthur Mariano, Edward Ryan, and Lynn Shay for sharing their results and their experience in using experimentally measured footprints in Lagrangian studies.

Chapter 3

Lagrangian Coherent Structures in n-Dimensional Systems

In collaboration with Francois Lekien and Jerrold E. Marsden

3.1 Introduction

The purpose of this chapter is to extend the results given in the previous chapter from planar systems to n-dimensional dynamical systems. Again, the context of this research is the study of transport and mixing in dynamical systems with aperiodic time dependence.

Most physical fluid systems are arguably 3-D. In special cases, the fluid can be considered 2-D, such as in thin films, or when coordinates can be chosen such that the strength of the vector field in one dimension is negligible when compared to the dynamics in the other two dimensions. However, many physical flows cannot be reduced to surface flows. The results of this chapter demonstrate that computing LCS from FTLE fields is equally applicable to fully 3- and even n-dimensional systems.

Not only are the practical motivations for having a technique that can handle n-dimensional systems compelling, but the theoretical motivation is important as well. Many classic dynamical systems techniques are inherently restricted to planar systems, e.g., the Poincaré-Bendixson Theorem, Dulac's Criterion, results from Index Theory, Chaos theory, etc. Therefore, it is important to show that there is no theoretical limitation to applying these LCS techniques to higher dimensional systems, even if computational concerns quickly impose practical limits.

In the previous chapter, we sought curves of high FTLE to represent LCS that act as separatrices partitioning the flow into dynamically distinct regions. In this chapter we seek hypersurfaces of dimension one less than the dimension of the phase space of the dynamical system. Such co-dimensional 1 hypersurfaces are generalized boundaries to transport. To illustrate the concepts developed, we compute the LCS for a simple analytical model of 3-D Rayleigh-Bénard convection.

3.2 Definitions

We study the dynamical system

$$\dot{\mathbf{x}}(t) = \mathbf{v}(\mathbf{x}(t), t) \ , \tag{3.1}$$

where $\mathbf{x}$ takes values in $\mathcal{D}$, an n-dimensional subset of $\mathbb{R}^n$, and with the following assumptions:

A1. The velocity field is at least C^0 in time and C^3 in space.

A2. The domain $\mathcal{D}$ is compact.

The first assumption is required to allow for the calculus needed to prove the analytic results of this chapter. Although this condition can be ensured by proper interpolation when working with data, it is typically not needed for practical purposes or numerical stability. For example, if $\mathbf{v}$ is specified on a Cartesian mesh, [50] provides C^1 tricubic interpolation, which is typically sufficient. Unstructured data can be interpolated by normal modes for complex boundaries [47]. Additionally, nearly all examples of practical importance must be handled numerically, so there is no loss of generality by assuming that the domain is closed and bounded, and hence compact since $\mathcal{D}$ is embedded in $\mathbb{R}^n$.

The flow map is denoted by $\phi_t^T : \mathbf{x}(t) \mapsto \mathbf{x}(t+T)$, which is simply the solution to equation (3.1) written as a mapping whose input is the initial location of a point at time t and whose output is the position at time $t+T$.

Theorem 3.2.1 *There is a constant $K > 0$ such that*

$$\left\| \frac{\mathrm{d}\phi_t^T(\mathbf{x})}{\mathrm{d}\mathbf{x}} \right\| \leq e^{K|T|} \ , \tag{3.2}$$

for arbitrary T.

Proof. From **A1**, the derivative of $\mathbf{v}$ with respect to space is a continuous function. Over the compact domain, $\mathcal{D} \times [t, t+T]$, the spatial derivative of $\mathbf{v}$ is therefore bounded, hence Lipschitz continuous in $\mathbf{x}$; let K denote the Lipschitz constant. Let $\mathbf{x}(t+T)$ and $\mathbf{x}_\epsilon(t+T)$ denote the solutions to equation (3.1) with initial conditions $\mathbf{x}(t) = \mathbf{x}_0$ and $\mathbf{x}_\epsilon(t) = \mathbf{x}_0 + \mathbf{z}$, respectively, with $\|\mathbf{z}\| = \epsilon$ for some real, positive ϵ, which can be arbitrarily small. The two solutions can be respectively written as

$$\begin{array}{rcl} \mathbf{x}(t+T) & = & \mathbf{x}_0 + \int_t^{t+T} \mathbf{v}(\mathbf{x}(\tau), \tau)\mathrm{d}\tau \ , \\ \mathbf{x}_\epsilon(t+T) & = & \mathbf{x}_0 + \mathbf{z} + \int_t^{t+T} \mathbf{v}(\mathbf{x}_\epsilon(\tau), \tau)\mathrm{d}\tau \ . \end{array} \tag{3.3}$$

Assuming $T > 0$, subtracting the two above equations from each other gives

$$\begin{aligned} \|\mathbf{x}(t+T) - \mathbf{x}_\epsilon(t+T)\| &\leq \|\mathbf{z}\| + \int_t^{t+T} \|\mathbf{v}(\mathbf{x}(\tau),\tau) - \mathbf{v}(\mathbf{x}_\epsilon(\tau),\tau)\| \, \mathrm{d}\tau & (3.4)\\ &\leq \epsilon + K \int_t^{t+T} \|\mathbf{x}(\tau) - \mathbf{x}_\epsilon(\tau)\| \, \mathrm{d}\tau & (3.5)\\ &\leq \epsilon e^{KT} & (3.6)\\ &= \epsilon e^{K|T|} \, , & (3.7) \end{aligned}$$

where the first line follows from the triangle inequality, the second line follows from applying the Lipschitz condition, and the third line follows from applying Gronwall's inequality. If $T < 0$, the above equations should technically be modified to read

$$\begin{aligned} \|\mathbf{x}(t+T) - \mathbf{x}_\epsilon(t+T)\| &\leq \|\mathbf{z}\| + \int_{t-|T|}^{t} \|\mathbf{v}(\mathbf{x}(\tau),\tau) - \mathbf{v}(\mathbf{x}_\epsilon(\tau),\tau)\| \, \mathrm{d}\tau & (3.8)\\ &\leq \epsilon + K \int_{t-|T|}^{t} \|\mathbf{x}(\tau) - \mathbf{x}_\epsilon(\tau)\| \, \mathrm{d}\tau & (3.9)\\ &\leq \epsilon e^{K|T|} \, . & (3.10) \end{aligned}$$

Using the definition of the derivative and equation (3.7), or (3.10), we have

$$\begin{aligned} \left\| \frac{\mathrm{d}\phi_t^T(\mathbf{x})}{\mathrm{d}\mathbf{x}} \right\| &= \lim_{\|\mathbf{z}\| \to 0} \frac{\|\mathbf{x}(t+T) - \mathbf{x}_\epsilon(t+T)\|}{\|\mathbf{z}\|} & (3.11)\\ &= \lim_{\epsilon \to 0} \frac{\|\mathbf{x}(t+T) - \mathbf{x}_\epsilon(t+T)\|}{\epsilon} & (3.12)\\ &\leq e^{K|T|} \, , & (3.13) \end{aligned}$$

which completes the proof. □

We can also provide a lower bound by the following theorem:

Theorem 3.2.2

$$\left\| \frac{\mathrm{d}\phi_t^T(\mathbf{x})}{\mathrm{d}\mathbf{x}} \right\| > 0 \, , \tag{3.14}$$

for arbitrary T.

Proof. Notice that $\phi_{t+T}^{-T}(\phi_t^T(\mathbf{x})) = \mathbf{x}$ for all $\mathbf{x} \in \mathcal{D}$. Differentiating this expression yields

$$\frac{\mathrm{d}\phi_{t+T}^{-T}(\mathbf{y})}{\mathrm{d}\mathbf{y}} \frac{\mathrm{d}\phi_t^T(\mathbf{x})}{\mathrm{d}\mathbf{x}} = \mathbb{I} \, , \tag{3.15}$$

where $\mathbf{y} = \phi_t^T(\mathbf{x})$ and $\mathbb{I}$ denotes the identity map. Suppose that $\|\mathrm{d}\phi_t^T(\mathbf{x})/\mathrm{d}\mathbf{x}\| = 0$. Then there exists an non-zero $\bar{\mathbf{x}}$ such that

$$\frac{\mathrm{d}\phi_t^T(\mathbf{x})}{\mathrm{d}\mathbf{x}} \bar{\mathbf{x}} = 0 \, .$$

Applying equation (3.15) to $\bar{\mathbf{x}}$ gives

$$\begin{aligned} \frac{\mathrm{d}\phi_{t+T}^{-T}(\mathbf{y})}{\mathrm{d}\mathbf{y}} \frac{\mathrm{d}\phi_t^T(\mathbf{x})}{\mathrm{d}\mathbf{x}} \bar{\mathbf{x}} &= \mathbb{I}\, \bar{\mathbf{x}} \\ 0 &= \bar{\mathbf{x}} \end{aligned}$$

providing a contradiction. □

3.2.1 Finite-Time Lyapunov Exponents

The derivative of the flow map, which we refer to as the deformation gradient,

$$\frac{\mathrm{d}\phi_t^T(\mathbf{x})}{\mathrm{d}\mathbf{x}} \tag{3.16}$$

is a linear operator that describes how an infinitesimal change of the initial position $\mathbf{x}$ influences the final position $\phi_t^T(\mathbf{x})$ after an interval of time T. The growth of an infinitesimal perturbation $\boldsymbol{\delta} \neq \mathbf{0}$ between t and $t+T$ is given by

$$0 < \left\| \frac{\mathrm{d}\phi_t^T(\mathbf{x})}{\mathrm{d}\mathbf{x}} \boldsymbol{\delta} \right\|^2 = \left\langle \frac{\mathrm{d}\phi_t^T(\mathbf{x})}{\mathrm{d}\mathbf{x}} \boldsymbol{\delta}, \frac{\mathrm{d}\phi_t^T(\mathbf{x})}{\mathrm{d}\mathbf{x}} \boldsymbol{\delta} \right\rangle = \left\langle \boldsymbol{\delta}, \frac{\mathrm{d}\phi_t^T(\mathbf{x})}{\mathrm{d}\mathbf{x}}^* \frac{\mathrm{d}\phi_t^T(\mathbf{x})}{\mathrm{d}\mathbf{x}} \boldsymbol{\delta} \right\rangle , \tag{3.17}$$

where the symbol $*$ denotes the adjoint (transpose). The strict inequality sign in the above equation is a consequence of Theorem 3.2.2.

equation (3.17) highlights the importance of the finite-time deformation tensor

$$\Delta_t^T(\mathbf{x}) = \frac{\mathrm{d}\phi_t^T(\mathbf{x})}{\mathrm{d}\mathbf{x}}^* \frac{\mathrm{d}\phi_t^T(\mathbf{x})}{\mathrm{d}\mathbf{x}} , \tag{3.18}$$

in the study of attraction and separation in fluids. Notice that equations (3.17) and (3.18) define the deformation tensor as a bilinear form. Throughout, we use a classical abuse of notation and also view $\Delta_t^T(\mathbf{x})$ as a linear operator using the Riesz representation theorem. More specifically, we define $\Delta_t^T(\mathbf{x})\boldsymbol{\delta}$ as the unique vector $\boldsymbol{\epsilon}$ such that

$$\forall \mathbf{y} \in \mathbb{R}^n : \left\langle \mathbf{y},\ \Delta_t^T(\mathbf{x})\boldsymbol{\delta} \right\rangle = \langle \mathbf{y}, \boldsymbol{\epsilon} \rangle \ . \tag{3.19}$$

Notice that $\Delta_t^T(\mathbf{x})$ is a real, symmetric operator by equation (3.18). Moreover, equation (3.17) indicates that $\Delta_t^T(\mathbf{x})$ is also positive definite. As a result, $\Delta_t^T(\mathbf{x})$ has n real, positive eigenvalues and we define the Finite-Time Lyapunov Exponent as

$$\sigma_t^T(\mathbf{x}) \triangleq \frac{1}{|T|} \ln \sqrt{\lambda_{\max}(\Delta_t^T(\mathbf{x}))} , \tag{3.20}$$

where $\lambda_{\max}(\Delta_t^T(\mathbf{x}))$ is the maximum eigenvalue of $\Delta_t^T(\mathbf{x})$. It is easily shown (cf.[93]) that a pertur-

bation $\boldsymbol{\delta}(t)$ to a point $\mathbf{x}(t)$ evolves as

$$\|\boldsymbol{\delta}(t+T)\| \leq e^{\sigma_t^T(\mathbf{x})|T|}\|\boldsymbol{\delta}(t)\| \,, \tag{3.21}$$

where strict equality holds if $\boldsymbol{\delta}(t)$ is chosen in the eigenvector direction of $\lambda_{\max}(\Delta_t^T(\mathbf{x}))$. Note that the integration time T can be positive or negative, corresponding to the *forward-time* and *backward-time* FTLE, respectively. In the next section, we build Lagrangian Coherent Structures as hypersurfaces that "locally maximizes" the FTLE field. The type of LCS depends on the type of FTLE field used; attracting and repelling LCS are obtained by changing the sign of the integration time T in the FTLE.

3.2.2 Lagrangian Coherent Structures

Observations of FTLE fields for time-dependent fluid systems reveals the presence of organized regions of high relative FTLE values [76, 77, 30, 32, 38, 48, 2, 93, 92]. Suppose that the fluid is experiencing qualitatively different dynamics in two quasi-invariant regions of the flow. In each of these regions, we expect a coherent motion of the fluid (such as in an eddy) and the eigenvalues of $\Delta_t^T(\mathbf{x})$ in that region will be close to 1, an indication that the fate of nearby particles is similar inside the sub-region.

At the boundary of two regions of qualitatively different dynamics (e.g., two eddies with different vorticity), perturbations of the initial conditions can cause particles to move in one or the other sub-region. This creates a much higher eigenvalue in the direction normal to the boundary. It are these boundaries, or *separatrices*, that we seek and define as LCS. The definition that we introduce below (the extension to n dimensions of the definition in [93]) captures this aspect by requiring that one eigenvalue of $\Delta_t^T(\mathbf{x})$ be greater than 1 while all the others have modulus less than 1. We exclude cases where, along the boundary, we have other eigenvalues larger than 1. These cases correspond to hyperbolic structures that are not co-dimension 1. As a result, they do not qualify as hypersurfaces dividing regions in the n-dimensional space [30].

Definition 3.2.1 *A **repelling LCS** is a co-dimension 1 manifold $\mathcal{M} \subset \mathcal{D} \subseteq \mathbb{R}^n$ of the forward time FTLE field satisfying the following conditions for each $\mathbf{x} \in \mathcal{M}$:*

LCS1. *$\Delta_t^T(\mathbf{x})$ has $n-1$ eigenvalues with modulus less than 1 and one eigenvalue greater than 1.*

LCS2. *The unit normal vector to the manifold, $\hat{\mathbf{n}}(\mathbf{x})$, is orthogonal to $\nabla\sigma_t^T(\mathbf{x})$.*

LCS3. *For all unit vectors $\hat{\mathbf{u}}$ such that $|\langle\hat{\mathbf{u}}, \hat{\mathbf{n}}\rangle| \neq 1$, $\Sigma(\hat{\mathbf{n}}, \hat{\mathbf{n}})$ satisfies*

$$\Sigma(\hat{\mathbf{u}}, \hat{\mathbf{u}}) > \Sigma(\hat{\mathbf{n}}, \hat{\mathbf{n}}) < 0 \,,$$

where Σ is the second derivative of $\sigma_t^T(\mathbf{x})$ and is thought of as a bilinear form evaluated at the point $\mathbf{x}$.

We require that $\mathcal{M}$ be orientable to guarantee the existence and uniqueness of a continuous normal unit vector on $\mathcal{M}$. In general, $\mathcal{M}$ is orientable if there is a non-vanishing volume form on $\mathcal{M}$. However we will represent $\mathcal{M}$ as the level-set of a C^2 function (cf. Def. 3.3.1 below) and use the gradient of the function to provide a well-defined normal.

Definition 3.2.2 *An **attracting LCS** is a repelling LCS of the backward time, $T < 0$, FTLE field.*

From a mathematical point of view, the smoothness of the FTLE field is a consequence of the smoothness of the eigenvalues of $\Delta_t^T(\mathbf{x})$, but is contingent to the fact that the maximum eigenvalue of $\Delta_t^T(\mathbf{x})$ remains isolated from the other eigenvalues, cf., Lemma 3.2.1 below. Separating the maximum eigenvalue of $\Delta_t^T(\mathbf{x})$ and the remaining eigenvalues by the unit circle is therefore also a convenient way to ensure the degree of smoothness that the results in this chapter require.

Lemma 3.2.1 *The FTLE $\sigma_t^T(\mathbf{x})$ is C^3 in an open neighborhood $\mathcal{G}$ of the LCS.*

Proof. By **A1**, the entries of the matrix $\Delta_t^T(\mathbf{x})$ are C^3. Therefore, the eigenvalues of $\Delta_t^T(\mathbf{x})$ are also C^3. Note that this does not necessarily imply that $\lambda_{\max}$ is C^3 since the maximum value can switch from one eigenvalue to another in a non-smooth manner. However, since the eigenvalues are continuous, we are guaranteed that **LCS1** holds in an open neighborhood $\mathcal{G}$ of the LCS. Inside $\mathcal{G}$, $\lambda_{\max}$ is outside the unit circle and all other eigenvalue are inside the unit circle. Therefore, $\lambda_{\max}$ does not undergo a switch and is thus C^3, making $\sigma_t^T(\mathbf{x})$ a C^3 function of $\mathbf{x}$. □

Corollary 3.2.1 *The normal vector $\hat{\mathbf{n}}$ to the LCS is C^1.*

Proof. From Lemma 3.2.1, Σ varies in a C^1 fashion. Since Σ is C^1 and the smallest eigenvalue of Σ is isolated, by **LCS3**, one can show that the associate eigenvector is C^1, as demonstrated by Dieci and Eirola [22]. However, this eigenvector (when normalized) corresponds to $\hat{\mathbf{n}}$ by **LCS3**. □

3.3 Flux

For convenience, the following corollary from [93] is restated:

Corollary 3.3.1

$$\frac{\partial \nabla \sigma_t^T(\mathbf{x})}{\partial t} = -J^* \nabla \sigma_t^T(\mathbf{x}) - \Sigma \mathbf{v} + \mathcal{O}\left(1/|T|\right), \tag{3.22}$$

where J is the spatial derivative of the velocity field $\mathbf{v}$ and is commonly referred to as the Jacobian matrix.

This corollary will be used later in proving the Lagrangian properties of the LCS; this result is independent of the dimension of the system so its proof [93] carries over to the n-dimensional case considered in this chapter without modification.

3.3.1 Representation

Suppose that we are given an FTLE field, $\sigma_t^T(\mathbf{x})$ for $t \in [t_1, t_2]$ that admits an LCS in the sense of Def. 3.2.1 or 3.2.2. We define a scalar function L of space and time as follows:

Definition 3.3.1 *For every time t, let $L(\mathbf{x}, t)$ be a function of $\mathbf{x} \in \mathcal{D}$ defined by the conditions*

1. $|L(\mathbf{x}, t)| = \|\mathbf{x} - \mathbf{x}_q\|$, *where $\mathbf{x}_q$ is the point on the LCS closest to point $\mathbf{x}$,*
2. $L(\mathbf{x}, t)\ \langle \mathbf{x} - \mathbf{x}_q, \hat{\mathbf{n}}(\mathbf{x}_q) \rangle \geq 0$,

where $\hat{\mathbf{n}}(\mathbf{x}_q)$ is the unit normal vector to the LCS at point $\mathbf{x}_q$. The function $L(\mathbf{x}, t)$ gives the "signed distance" from $\mathbf{x}$ to the nearest point on the LCS. That is, the first line specifies the magnitude of the function as the distance between the points, and the second line determines the sign. In a neighborhood of the LCS, points on one side of the LCS have a positive value of L and a negative value on the other side. By definition of L, the LCS is given by the zero set $L = 0$. This function is never computed in practical applications and is used in this work as a means to derive the properties of the LCS. As shown in the next section, ∇L can be viewed as an extension of the normal vector $\hat{\mathbf{n}}$ away from the LCS.

3.3.2 Properties

Our objective is to analyze the Lagrangian properties of the LCS by analyzing the function L defined above. For this purpose, the first and second derivatives of L are needed. We need to start by showing that L is C^2 near the LCS. Clearly L is continuous everywhere. However, there may exist points in the domain that have multiple possible values for $\mathbf{x}_q$, hence L might not be C^1 everywhere. However we can prove that we can always find an open set that contains the LCS and excludes any of these points. Furthermore, we show that L is also C^2 over this set and therefore its second derivative is well-defined.

Theorem 3.3.1 *Let $\mathcal{B} \subset \mathcal{D}$ be the set of points with non-unique $\mathbf{x}_q$. The LCS and the closure of $\mathcal{B}$ are disjoint.*

Proof. The proof is quite long, but the critical ingredient in this proof is the fact that the curvature of the LCS must remain finite and thus, close enough to the LCS, each point has a unique closest point on the LCS. We will show that $\overline{\mathcal{B}}$ (i.e., the closure of $\mathcal{B}$) must be at a finite distance from the LCS by contradiction; if $\overline{\mathcal{B}} \cap \mathcal{M} \neq \emptyset$, then the curvature of the LCS would become infinite.

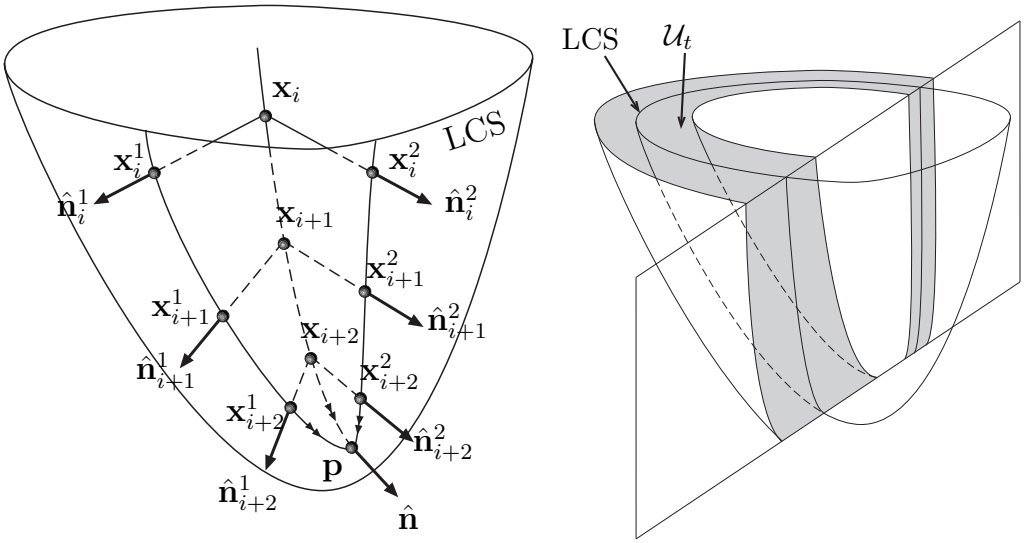

(a) Setting for the proof of Theorem 3.1

(b) An open set $\mathcal{U}_t$ enclosing the LCS, where L is C^2

Figure 3.1: For any LCS, there exists an open cover that excludes points of discontinuity of L.

Consider an arbitrary point $\mathbf{p} \in \overline{\mathcal{B}} \cap \mathcal{M}$. In this case, $\mathbf{p}$ is in the closure of $\mathcal{B}$, so there exists at least one sequence $\mathbf{x}_i \in \mathcal{B}$ such that $\mathbf{x}_i \to \mathbf{p} \in \mathcal{M}$. By definition of $\mathcal{B}$, for each $\mathbf{x}_i$, there exist at least two points $\mathbf{x}_i^1$ and $\mathbf{x}_i^2$ on $\mathcal{M}$ that are equidistant from $\mathbf{x}_i$, and every other point on the LCS is located at the same distance from $\mathbf{x}_i$ as these points or farther.

Notice that

$$\|\mathbf{x}_i - \mathbf{p}\| \xrightarrow[i\to\infty]{} 0 \tag{3.23}$$

and

$$\left\|\mathbf{x}_i^1 - \mathbf{x}_i\right\| = \left\|\mathbf{x}_i^2 - \mathbf{x}_i\right\| \leq \|\mathbf{p} - \mathbf{x}_i\| \ , \tag{3.24}$$

so we must have

$$\begin{cases} \mathbf{x}_i^1 \xrightarrow[i\to\infty]{} \mathbf{p} \ , \\ \mathbf{x}_i^2 \xrightarrow[i\to\infty]{} \mathbf{p} \ , \\ \mathbf{x}_i^1 \neq \mathbf{x}_i^2 \ \text{ for all } i \ . \end{cases} \tag{3.25}$$

Since the LCS is a C^2 manifold, there exists an open set about point $\mathbf{p}$, $\mathcal{O}_\mathbf{p} \subset \mathcal{M}$ where the LCS can be described by a C^2 diffeomorphism, $h : A \subset \mathbb{R}^{n-1} \to \mathcal{O}_\mathbf{p} \subset \mathcal{M}$ (i.e., a local chart of the manifold containing the point $\mathbf{p}$). We will denote by $\mathbf{s} = (s_1, s_2, \cdots, s_{n-1})$ the coordinates in the open set of $\mathbb{R}^{n-1}$.

We will now assume that the points $\mathbf{x}_i$, $\mathbf{x}_i^1$ and $\mathbf{x}_i^2$ are all contained in $\mathcal{O}_\mathbf{p}$. If this is not the case, the sequences can always be cropped by removing a finite number of elements at the beginning of each sequence. That is, since the three sequences converge toward $\mathbf{p}$, cf., equation (3.25), for i

sufficiently large, all the elements are contained in $\mathcal{O}_{\mathbf{p}}$.

The mapping h is a bijection, therefore for any i, there are unique $\mathbf{s}_i^1$ and $\mathbf{s}_i^2$ such that $h(\mathbf{s}_i^1) = \mathbf{x}_i^1$ and $h(\mathbf{s}_i^2) = \mathbf{x}_i^2$. Similarly, we denote by $\mathbf{s}_{\mathbf{p}}$, the unique point of A such that $h(\mathbf{s}_{\mathbf{p}}) = \mathbf{p}$.

Notice that the largest principal curvature at point $\mathbf{p}$ is nothing but the largest singular value of $\frac{\partial h^{-1}\hat{\mathbf{n}}(h(\mathbf{s}))}{\partial \mathbf{s}}\Big|_{\mathbf{s}_{\mathbf{p}}}$. Therefore, Corollary 3.2.1 implies that

$$\left\| \frac{\partial \hat{\mathbf{n}}(h(\mathbf{s}_{\mathbf{p}}))}{\partial \mathbf{s}}\, \delta\mathbf{s} \right\| < \infty \,, \tag{3.26}$$

for any $\delta\mathbf{s}$. The converging sequences of equation (3.25) in $\mathcal{O}_{\mathbf{p}}$ allow us to express the derivative above as the limit of the difference between the normal vectors at points $\mathbf{x}_i^1$ and $\mathbf{x}_i^2$. Let us denote by $\hat{\mathbf{n}}_i^1$ and $\hat{\mathbf{n}}_i^2$ the unit vectors normal to the LCS at, respectively, $\mathbf{x}_i^1$ and $\mathbf{x}_i^2$; cf. Fig. 3.1 for the geometric interpretation of these ideas for $n = 3$. Since equation (3.26) hold for all $\delta\mathbf{s}$, we can choose

$$\delta\mathbf{s} = \lim_{i\to\infty} \frac{\mathbf{s}_i^2 - \mathbf{s}_i^1}{\|\mathbf{s}_i^2 - \mathbf{s}_i^1\|} \,.$$

From equation (3.26), we get

$$\kappa \doteq \lim_{i\to\infty} \frac{\left\|\hat{\mathbf{n}}_i^2 - \hat{\mathbf{n}}_i^1\right\|}{\|\mathbf{s}_i^2 - \mathbf{s}_i^1\|} < \infty \,. \tag{3.27}$$

We will compute the limit in equation (3.27) and show that it goes unbounded, providing the contradiction.

Notice that the points $\mathbf{x}_i^1$ and $\mathbf{x}_i^2$ are the points on the LCS that are the closest to $\mathbf{x}_i$, hence the vectors $\mathbf{x}_i^1 - \mathbf{x}_i$ and $\mathbf{x}_i^2 - \mathbf{x}_i$ must be aligned with, respectively, $\hat{\mathbf{n}}_i^1$ and $\hat{\mathbf{n}}_i^2$. Therefore the difference between the normal vectors can be written

$$\left\|\hat{\mathbf{n}}_i^2 - \hat{\mathbf{n}}_i^1\right\| = \left\| \frac{\mathbf{x}_i^2 - \mathbf{x}_i}{\|\mathbf{x}_i^2 - \mathbf{x}_i\|} - \frac{\mathbf{x}_i^1 - \mathbf{x}_i}{\|\mathbf{x}_i^1 - \mathbf{x}_i\|} \right\| = \frac{\left\|\mathbf{x}_i^2 - \mathbf{x}_i^1\right\|}{\|\mathbf{x}_i^2 - \mathbf{x}_i\|} \,. \tag{3.28}$$

We also have

$$\left\| \frac{\partial h(\mathbf{s})}{\partial \mathbf{s}}\Big|_{\mathbf{s}_{\mathbf{p}}} \delta\mathbf{s} \right\| = \lim_{i\to\infty} \frac{\left\|\mathbf{x}_i^2 - \mathbf{x}_i^1\right\|}{\|\mathbf{s}_i^2 - \mathbf{s}_i^1\|} = D_{\mathbf{p}} > 0 \,, \tag{3.29}$$

because $h(\mathbf{s})$ is a C^1diffeomorphism, hence $\left\|\frac{\partial h(\mathbf{s})}{\partial \mathbf{s}}\right\| \neq 0$ on the LCS and must remain positive in a neighborhood of $\mathbf{s} = \mathbf{s}_{\mathbf{p}}$ by continuity. As a result, there is an i^* such that for all $i > i^*$,

$$\frac{\left\|\mathbf{x}_i^2 - \mathbf{x}_i^1\right\|}{\|\mathbf{s}_i^2 - \mathbf{s}_i^1\|} \geq \frac{D_{\mathbf{p}}}{2} > 0 \,, \tag{3.30}$$

by definition of the limit.

Equations (3.28) and (3.30) give

$$\kappa = \lim_{i\to\infty} \frac{1}{\|\mathbf{x}_i^2 - \mathbf{x}_i\|} \frac{\left\|\mathbf{x}_i^2 - \mathbf{x}_i^1\right\|}{\|\mathbf{s}_i^2 - \mathbf{s}_i^1\|} \geq \frac{D_{\mathbf{p}}}{2} \lim_{i\to\infty} \frac{1}{\|\mathbf{x}_i^2 - \mathbf{x}_i\|} = +\infty \ , \tag{3.31}$$

which contradicts equation (3.27). □

Lemma 3.2.1 states that $\sigma_t^T(\mathbf{x})$ is C^3 on an open cover $\mathcal{G}$ of the LCS. Theorem 3.3.1 shows that $\overline{\mathcal{B}}$, the closure of the set of points with non-unique $\mathbf{x}_q$, does not interesect the LCS. It is therefore natural to combine these two results and define

$$\mathcal{U}_t = \left\{\mathcal{D} \setminus \overline{\mathcal{B}}\right\} \cap \mathcal{G} \ . \tag{3.32}$$

The resulting set $\mathcal{U}_t$ is an open cover of the LCS since both $\mathcal{G}$ and $\mathcal{D} \setminus \overline{\mathcal{B}}$ contain the LCS. Inside $\mathcal{U}_t$, the FTLE field $\sigma_t^T(\mathbf{x})$ is C^3 and each point has a unique $\mathbf{x}_q$. We can therefore prove the smoothness of L inside this open cover.

Theorem 3.3.2 *$L(x,t)$ is C^2 over the open set $\mathcal{U}_t$ containing the LCS.*

Proof. Since

$$L(\mathbf{x},t) = \pm \|\mathbf{x} - \mathbf{x}_q\| \ , \tag{3.33}$$

we have

$$\nabla L = \frac{\pm 1}{\|\mathbf{x} - \mathbf{x}_q\|} \left\langle I - \frac{\mathrm{d}\mathbf{x}_q}{\mathrm{d}\mathbf{x}}, \mathbf{x} - \mathbf{x}_q \right\rangle \ . \tag{3.34}$$

However,

$$\left\langle \frac{\mathrm{d}\mathbf{x}_q}{\mathrm{d}\mathbf{x}}, \mathbf{x} - \mathbf{x}_q \right\rangle = 0 \tag{3.35}$$

in $\mathcal{U}_t$ because the closest point on the LCS does not change with variations in the direction normal to $\mathcal{M}$. As a result,

$$\nabla L = \frac{\mathbf{x} - \mathbf{x}_q}{\pm \|\mathbf{x} - \mathbf{x}_q\|} = \frac{\mathbf{x} - \mathbf{x}_q}{L} = \hat{\mathbf{n}}(\mathbf{x}_q) \ , \tag{3.36}$$

where we have used the fact that $\mathbf{x}_q$ is the point on the LCS closest to $\mathbf{x}$, hence $\hat{\mathbf{n}}(\mathbf{x}_q)$ must be parallel to $\mathbf{x} - \mathbf{x}_q$. Recall that there is a unique $\mathbf{x}_q$ for each $\mathbf{x} \in \mathcal{U}_t$, by virtue of Theorem 3.3.1. By Corollary 3.2.1, the map $\hat{\mathbf{n}}(\mathbf{x}_q)$ that gives the normal vector at a point $\mathbf{x}_q \in$ LCS is C^1 thus $\nabla L(\mathbf{x}) = \hat{\mathbf{n}}(\mathbf{x}_q)$ is C^1, which implies that L is C^2. □

The primary result that we will next derive is an estimate for the flux across an LCS and is mainly is given by Theorem 3.3.4, which gives a similar estimate as derived in [93] for planar systems. Below, $\hat{\mathbf{t}}$ denotes an arbitrary vector in the tangent plane to $\mathcal{M}$, i.e., $\left\langle \hat{\mathbf{t}}, \hat{\mathbf{n}} \right\rangle = 0$. Let $\mathcal{L}$ be the Hessian of L and note the following properties of $\mathcal{L}$ and Σ:

Lemma 3.3.1 *Σ and $\mathcal{L}$ are self-adjoint.*

Proof. This result holds due to the symmetry of mixed partials. From $\Sigma(\mathbf{u},\mathbf{v}) = \Sigma(\mathbf{v},\mathbf{u})$, we deduce immediately that $\langle \mathbf{u}, \Sigma\mathbf{v}\rangle = \langle \mathbf{v}, \Sigma\mathbf{u}\rangle = \langle \Sigma\mathbf{u}, \mathbf{v}\rangle$ because the derivatives are necessarily real numbers. □

Theorem 3.3.3 *For $L = 0$ and $\forall\, \hat{\mathbf{t}}$, we have*

$$\left\langle \hat{\mathbf{t}}, \hat{\mathbf{n}} \right\rangle = 0 \implies \left\langle \hat{\mathbf{t}}, \Sigma\hat{\mathbf{n}} \right\rangle = \left\langle \hat{\mathbf{n}}, \Sigma\hat{\mathbf{t}} \right\rangle = 0 \,.$$

Proof. From Def. 3.2.1, **LCS3** implies that $\nabla L = \hat{\mathbf{n}}$ is an eigenvector of Σ. Hence $\left\langle \hat{\mathbf{t}}, \Sigma\hat{\mathbf{n}} \right\rangle = \lambda_{\min}(\Sigma) \left\langle \hat{\mathbf{t}}, \hat{\mathbf{n}} \right\rangle = 0$, where $\lambda_{\min}(\Sigma)$ is the smallest eigenvalue of Σ. □

Corollary 3.3.2 *For $L = 0$ and an arbitrary vector $\mathbf{v}$, we have $\langle \hat{\mathbf{n}}, \Sigma\mathbf{v}\rangle = \langle \hat{\mathbf{n}}, \Sigma\hat{\mathbf{n}}\rangle \langle \hat{\mathbf{n}}, \mathbf{v}\rangle$.*

Proof. Notice that any vector $\mathbf{v}$ can be written as

$$\mathbf{v} = \hat{\mathbf{t}} + \langle \hat{\mathbf{n}}, \mathbf{v}\rangle \hat{\mathbf{n}} \,, \tag{3.37}$$

for a properly chosen $\hat{\mathbf{t}}$ in the tangent plane to $\mathcal{M}$. Computing $\langle \hat{\mathbf{n}}, \Sigma\mathbf{v}\rangle$ from the expansion in equation (3.37) and applying Theorem 3.3.3 gives the desired result.

□

Lemma 3.3.2 $\mathcal{L}\hat{\mathbf{n}} = 0$ *everywhere in $\mathcal{U}_t$.*

Proof. Everywhere in $\mathcal{U}_t$, L is C^2, so the gradient ∇L exists and is differentiable. In particular, $\|\nabla L\| = 1$, therefore

$$0 = \nabla\left(\|\nabla L\|^2\right) = 2\,\mathcal{L}\nabla L = 2\,\mathcal{L}\hat{\mathbf{n}} \,. \tag{3.38}$$

□

Lemma 3.3.3 *On the LCS, i.e., for $L = 0$,*

$$\langle \hat{\mathbf{n}}, \Sigma\hat{\mathbf{n}}\rangle \frac{\partial L}{\partial t} = \frac{\partial \left\langle \hat{\mathbf{n}}, \nabla\sigma_t^T(\mathbf{x})\right\rangle}{\partial t} \,. \tag{3.39}$$

Proof. Take $\mathbf{x}$ on the LCS at time t, i.e. $L(\mathbf{x}, t) = 0$. Define $\mathbf{y} = \mathbf{x} + \alpha(\delta t)\hat{\mathbf{n}}$ such that $L(\mathbf{y}, t+\delta t) = 0$. In other words, $\mathbf{y}$ is at the intersection of the LCS at time $t + \delta t$ and the line starting at $\mathbf{x}$, orthogonal to the LCS at time t (see Fig. 3.2). Since we require $\mathbf{y} = \mathbf{x}$ for $\delta t = 0$, it follows that $\alpha(\delta t)$ is $\mathcal{O}(\delta t)$. Expanding L to first order in δt gives the following (where all derivatives on the

right-hand side of equations (3.40)–(3.48) are evaluated at $\mathbf{x}$ and t unless otherwise specified):

$$0 = L(\mathbf{y}, t+\delta t) = L(\mathbf{x}, t) + \alpha + \frac{\partial L}{\partial t}\delta t + \mathcal{O}(\delta t^2) \,, \tag{3.40}$$

$$= \alpha + \frac{\partial L}{\partial t}\delta t + \mathcal{O}(\delta t^2) \,. \tag{3.41}$$

Therefore,

$$\alpha = -\frac{\partial L}{\partial t}\delta t + \mathcal{O}(\delta t^2) \,. \tag{3.42}$$

Now expanding ∇L, and plugging in Lemma 3.3.2, gives

$$\nabla L\big|_{\mathbf{y},t+\delta t} = \nabla L + \frac{\partial \nabla L}{\partial t}\delta t + \mathcal{O}(\delta t^2) \,. \tag{3.43}$$

Taylor expanding $\nabla \sigma_t^T(\mathbf{x})\big|_{\mathbf{y},t+\delta t}$ gives

$$\nabla \sigma_t^T(\mathbf{x})\big|_{\mathbf{y},t+\delta t} = \nabla \sigma_t^T(\mathbf{x}) + \alpha \Sigma \hat{\mathbf{n}} + \frac{\partial \nabla \sigma_t^T(\mathbf{x})}{\partial t}\delta t + \mathcal{O}(\delta t^2) \,. \tag{3.44}$$

From Eqs. (3.36) and (3.42) we have

$$\nabla \sigma_t^T(\mathbf{x})\big|_{\mathbf{y},t+\delta t} = \nabla \sigma_t^T(\mathbf{x}) - \frac{\partial L}{\partial t}\Sigma \nabla L \delta t + \frac{\partial \nabla \sigma_t^T(\mathbf{x})}{\partial t}\delta t + \mathcal{O}(\delta t^2) \,. \tag{3.45}$$

Since $\mathbf{y}$ is on the LCS at time $t+\delta t$, we must have

$$0 = \left\langle \nabla L|_{\mathbf{y},t+\delta t} \,,\, \nabla \sigma_t^T(\mathbf{x})\big|_{\mathbf{y},t+\delta t} \right\rangle \tag{3.46}$$

$$= \left\langle \nabla L, \nabla \sigma_t^T(\mathbf{x}) \right\rangle + \delta t \left(-\frac{\partial L}{\partial t} \left\langle \nabla L, \Sigma \nabla L \right\rangle + \frac{\partial \left\langle \nabla L, \nabla \sigma_t^T(\mathbf{x}) \right\rangle}{\partial t} \right) + \mathcal{O}(\delta t^2) \tag{3.47}$$

$$= \delta t \left(- \left\langle \hat{\mathbf{n}}, \Sigma \hat{\mathbf{n}} \right\rangle \frac{\partial L}{\partial t} + \frac{\partial \left\langle \hat{\mathbf{n}}, \nabla \sigma_t^T(\mathbf{x}) \right\rangle}{\partial t} \right) + \mathcal{O}(\delta t^2) \,. \tag{3.48}$$

Hence, we get the desired result, since δt is arbitrary. □

By definition of the function L it is not hard to show [93] that

$$\frac{\mathrm{d}L}{\mathrm{d}t} = \nabla L \cdot \left(\frac{\mathrm{d}\mathbf{x}}{\mathrm{d}t} - \frac{\mathrm{d}\mathbf{x}_q}{\mathrm{d}t} \right) \,. \tag{3.49}$$

On the LCS, i.e., for $L = 0$, the two points $\mathbf{x}$ and $\mathbf{x}_q$ are equal; however, we think of $\mathbf{x}$ as being a *Lagrangian*, or material, point while $\mathbf{x}_q$ is viewed as a point that moves with the LCS. Therefore, the total flux across the LCS is given by

$$\Phi(t) = \int_{\mathrm{LCS}} \frac{\mathrm{d}L}{\mathrm{d}t} \, \mathrm{d}s \,, \tag{3.50}$$

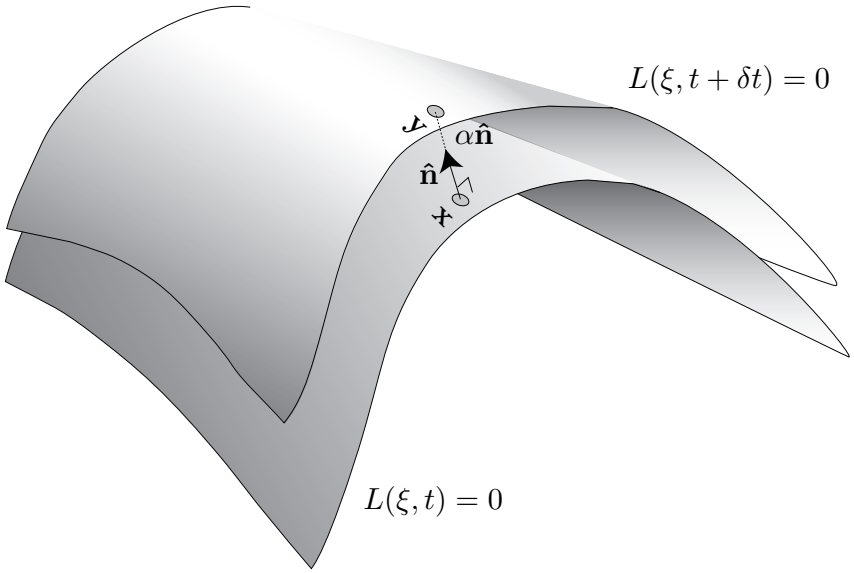

Figure 3.2: Quantities discussed in Lemma 3.3.3.

where the integral is taken over the LCS, i.e., the co-dimension one surface $\mathcal{M}$. The next theorem contains an expression for $\mathrm{d}L/\mathrm{d}t$ based on quantities defining the FTLE and velocity fields.

Theorem 3.3.4 *For $L = 0$, we have*

$$\langle \hat{\mathbf{n}}, \Sigma\hat{\mathbf{n}} \rangle \frac{\mathrm{d}L}{\mathrm{d}t} = \left\langle \nabla\sigma_t^T(\mathbf{x}), \frac{\partial\hat{\mathbf{n}}}{\partial t} - J\hat{\mathbf{n}} \right\rangle + \mathcal{O}\left(1/|T|\right) \ . \tag{3.51}$$

Proof. Lemma 3.3.3 gives

$$\langle \hat{\mathbf{n}}, \Sigma\hat{\mathbf{n}} \rangle \frac{\mathrm{d}L}{\mathrm{d}t} = \frac{\partial \left\langle \hat{\mathbf{n}}, \nabla\sigma_t^T(\mathbf{x}) \right\rangle}{\partial t} + \langle \hat{\mathbf{n}}, \Sigma\hat{\mathbf{n}} \rangle \langle \hat{\mathbf{n}}, \mathbf{v} \rangle \ . \tag{3.52}$$

Applying Corollary 3.3.2 and the chain rule for the derivative gives

$$\langle \hat{\mathbf{n}}, \Sigma\hat{\mathbf{n}} \rangle \frac{\mathrm{d}L}{\mathrm{d}t} = \left\langle \nabla\sigma_t^T(\mathbf{x}), \frac{\partial\hat{\mathbf{n}}}{\partial t} \right\rangle + \left\langle \hat{\mathbf{n}}, \frac{\partial\nabla\sigma_t^T(\mathbf{x})}{\partial t} \right\rangle + \langle \hat{\mathbf{n}}, \Sigma\mathbf{v} \rangle \ . \tag{3.53}$$

Using Corollary 3.3.1 in equation (3.53) gives equation (3.51). □

The above theorem provides an estimate for the instantaneous flux across an LCS. The estimate given in equation (3.51) is nearly identical to the flux estimate provided in [93] for the case of two-dimensional dynamical systems. In particular, we note that the flux is inversely proportional to how well-defined the LCS is, which is measured by the term $\langle \hat{\mathbf{n}}, \Sigma\hat{\mathbf{n}} \rangle$. The term

$$\left\langle \nabla\sigma_t^T(\mathbf{x}), \frac{\partial\hat{\mathbf{n}}}{\partial t} - J\hat{\mathbf{n}} \right\rangle$$

can be thought of as the difference between the local rotation rate of the LCS and the instantaneous rotation due to the Eulerian velocity field measured in the direction of $\nabla\sigma$. The $\mathcal{O}(1/|T|)$ term in equation (3.51) decreases exponentially with the integration time used to compute the FTLE field.

3.4 Example: Three-Dimensional Rayleigh-Bénard Convection Cell

In this section, we illustrate the computation of LCS on a three-dimensional model of time-dependent Rayleigh-Bénard convection derived from the work of Solomon and Gollub [99, 100, 101].

3.4.1 The Model

The model of Solomon and Gollub involves an infinite array of two-dimensional convection cells bounded from above and below by horizontal solid boundaries. It is derived from the stream function

$$\psi = \frac{A}{k} \sin\left[k\left[x - g(t)\right]\right] \sin z \ ,$$

where A is the maximum vertical velocity in the system, k is the wave number, and $g(t)$ represents the lateral motion of the roll pattern. The velocity field is given by

$$\begin{aligned} \dot{x} &= \frac{\partial\psi}{\partial z} &&= \frac{A}{k} \sin k\xi \cos z \ , \\ \dot{z} &= -\frac{\partial\psi}{\partial x} &&= -A \cos k\xi \sin z \ , \end{aligned} \tag{3.54}$$

where $\xi = x - g(t)$.

To extend this model to three-dimensional cylindrical cells, we start by considering the autonomous version of Solomon and Gollub's model (i.e., $g(t) = 0$) applied to the vertical, z, and the radial, r, variables:

$$\begin{aligned} \dot{r} &= \frac{A}{k} r \sin kr \cos z \ , \\ \dot{z} &= -A\,\nu(r) \cos kr \sin z + \mu(r,z) \ , \\ \dot{\theta} &= 0 \ , \end{aligned} \tag{3.55}$$

where r, θ, and z are the cylindrical coordinates. The functions ν and μ are added as a means to recover incompressibility in the three-dimensional space; that is, choosing their value such that the divergence relation,

$$\begin{aligned} \nabla\cdot\left(\dot{r},\dot{z},\dot{\theta}\right) &= \frac{\partial\dot{r}}{\partial r} + \frac{\dot{r}}{r} + \frac{\partial\dot{z}}{\partial z} + \frac{1}{r}\frac{\partial\dot{\theta}}{\partial\theta} \\ &= \frac{2A}{k} \sin kr \cos z + \left[r - \nu(r)\right] A \cos kr \cos z + \frac{\partial\mu}{\partial z}(r,z) \ , \end{aligned}$$

is equal to zero. A simple choice that respects the horizontal boundary conditions is

$$\nu(r) = r \ ,$$

and

$$\mu(r,z) = -\frac{2A}{k} \sin kr \, \sin z \ .$$

The corresponding autonomous model in Cartesian coordinates is

$$\begin{aligned} \dot{x} &= \tfrac{A}{k} \, x \, \sin kr \, \cos z \ , \\ \dot{y} &= \tfrac{A}{k} \, y \, \sin kr \, \cos z \ , \\ \dot{z} &= -A \sin z \left(r \cos kr + \tfrac{2}{k} \sin kr \right) \ , \end{aligned} \tag{3.56}$$

where $r^2 = x^2 + y^2$.

As a consequence of the above choice for $\nu(r)$ and $\mu(r,z)$, we see from equation (3.56) that the vector field is zero when $r = 0$. This condition could represent a case where there is a thin wire placed in the center of the convection cell, which has a no-slip boundary condition. However, this condition will have little consequence on the transport structure of the time-dependent system since this is a non-hyperbolic, co-dimension 2 structure.

To add an explicit time-dependence to the model, we follow the same procedure as in [99]. More specifically, we replace x in the autonomous velocity field by $\xi = x - g(t)$. Such a spatially-homogeneous, time-dependent translation does not affect the divergence. Any autonomous, divergence-free vector field $\dot{\mathbf{x}} = f(\mathbf{x})$ can be transformed into a divergence-free, time-dependent system $\dot{\mathbf{x}} = f(\mathbf{x} - \mathbf{p}(t))$ for any $\mathbf{p}(t)$. For the Rayleigh-Bénard cell, the translation $\mathbf{p}(t)$ is chosen to align with the x-axis. The resulting model is

$$\begin{aligned} \dot{x} &= \tfrac{A}{k} \, \xi \, \sin k\rho \, \cos z \ , \\ \dot{y} &= \tfrac{A}{k} \, y \, \sin k\rho \, \cos z \ , \\ \dot{z} &= -A \sin z \left(\rho \cos k\rho + \tfrac{2}{k} \sin k\rho \right) \ , \end{aligned} \tag{3.57}$$

where $\xi = x - g(t)$ and $\rho^2 = \xi^2 + y^2$.

The model given in equation (3.57) has an interesting property that can be used to improve the efficiency of the numerical simulations. The intersection of the two planes $x = g(t)$ and $y = 0$ defines a line that is parallel to the z-axis and intersects the x-axis at $x = g(t)$. The equation $y = K\xi$, where $K \in \mathbb{R}$, parameterizes all planes that contain this line. Each of these vertical planes containing this line, and following this line with time (since $g(t)$ is time-dependent) remains invariant. To see this,

let $\tilde{\theta}$ denote the angle the plane $y = K\xi$ makes with the x-axis. Thus we have

$$\begin{aligned} \xi &= \rho \cos\tilde{\theta} \,, \\ y &= \rho \sin\tilde{\theta} \,. \end{aligned} \tag{3.58}$$

The vector $\left[\sin\tilde{\theta},\ -\cos\tilde{\theta}\right]$ is orthogonal to the plane $y = K\xi$. Using equation (3.58), we can show

$$\left[\begin{array}{cc} \sin\tilde{\theta} & -\cos\tilde{\theta} \end{array}\right] \left[\begin{array}{c} \dot{\xi} \\ \dot{y} \end{array}\right] = -\rho\dot{\tilde{\theta}} \,. \tag{3.59}$$

However, it is easy to show that $\dot{\tilde{\theta}} = 0$ for all $\rho \neq 0$. Hence the "moving" planes $y = K\xi$ are invariant. To take advantage of the reduction, we can fix $\tilde{\theta} = \tilde{\theta}_0$ for each plane and allow negative values of ρ to avoid the discontinuity of $\tilde{\theta}$ along $\rho = 0$. The dynamics on each plane is given by

$$\begin{aligned} \dot{\rho} &= \tfrac{A}{k}\rho \sin k\rho \, \cos z - g'(t)\cos\tilde{\theta}_0 \,, \\ \dot{z} &= -A \sin z \left(\rho \, \cos k\rho + \tfrac{2}{k}\sin k\rho\right) \,. \end{aligned} \tag{3.60}$$

This reduction can be used to check the output of the numerical algorithms or to improve the computation of the FTLE field by focusing on only one such "moving plane" at a time.

3.4.2 Three-Dimensional LCS

The LCS for the model given in equation (3.57) are shown in Fig. 3.4.2 for parameters $A = 0.24$ and $k = 2$. The blue and red surfaces are, respectively, the repelling and attracting LCS for this system. In the results shown here, the forcing $g(t)$ is a Gaussian noise with unit variance and unit correlation in space and time. Such a one-dimensional displacement can be easily computed by taking the inverse Fourier transform of the Fourier transform of a random sequence fitted to the desired Gaussian spectrum [46].

To avoid the lateral motion of the image, the LCS in Fig. 3.4.2 are shown in the (ξ, y, z) coordinate system, instead of (x, y, z). High resolution snapshots and complete animations can be downloaded at `http://www.mangen.info/papers/lcs3d`.

3.4.3 Dynamics and Transport

Figures 3.4.2 and 3.4.2 reveal that the cell is bounded by the attracting and repelling LCS. The "primary" intersection between the two surfaces can be used to define a moving, permeable boundary in the spirit of [5]. Notice that, in this system, the geometry of the lobes does not present the many difficulties highlighted in [5]. Due to the symmetry of the system, the LCS for periodic $g(t)$ are the union of two-dimensional LCS in a Poincaré section of the periodic system. As a result, the

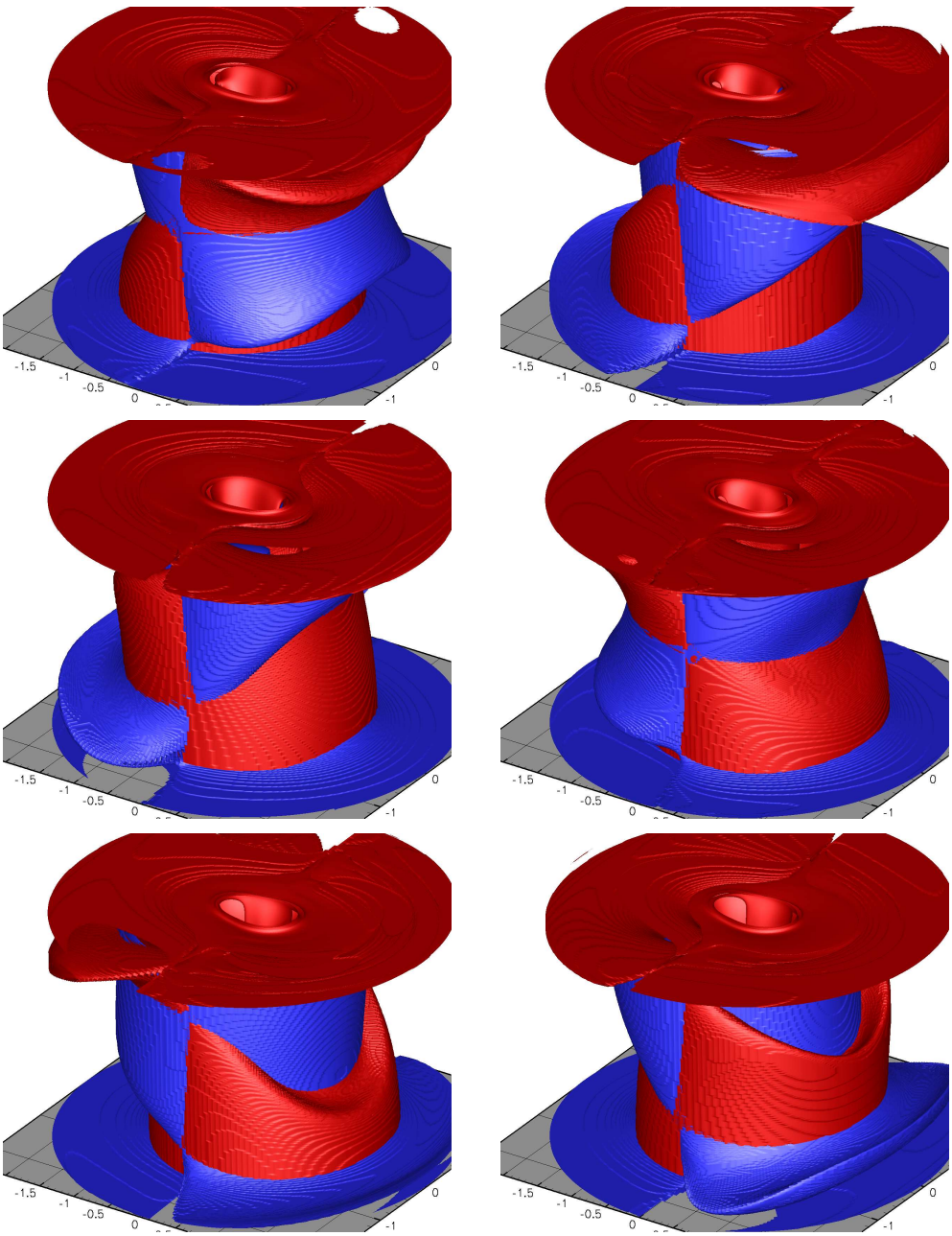

Figure 3.3: Attracting (blue) and repelling (red) LCS for a dynamical model of Rayleigh-Bénard convection in a cylinder. The center cell is bounded by the moving LCS. The non-transverse intersections between the LCS cause the presence of lobes whose dynamics are responsible for transport to and from the center cell.

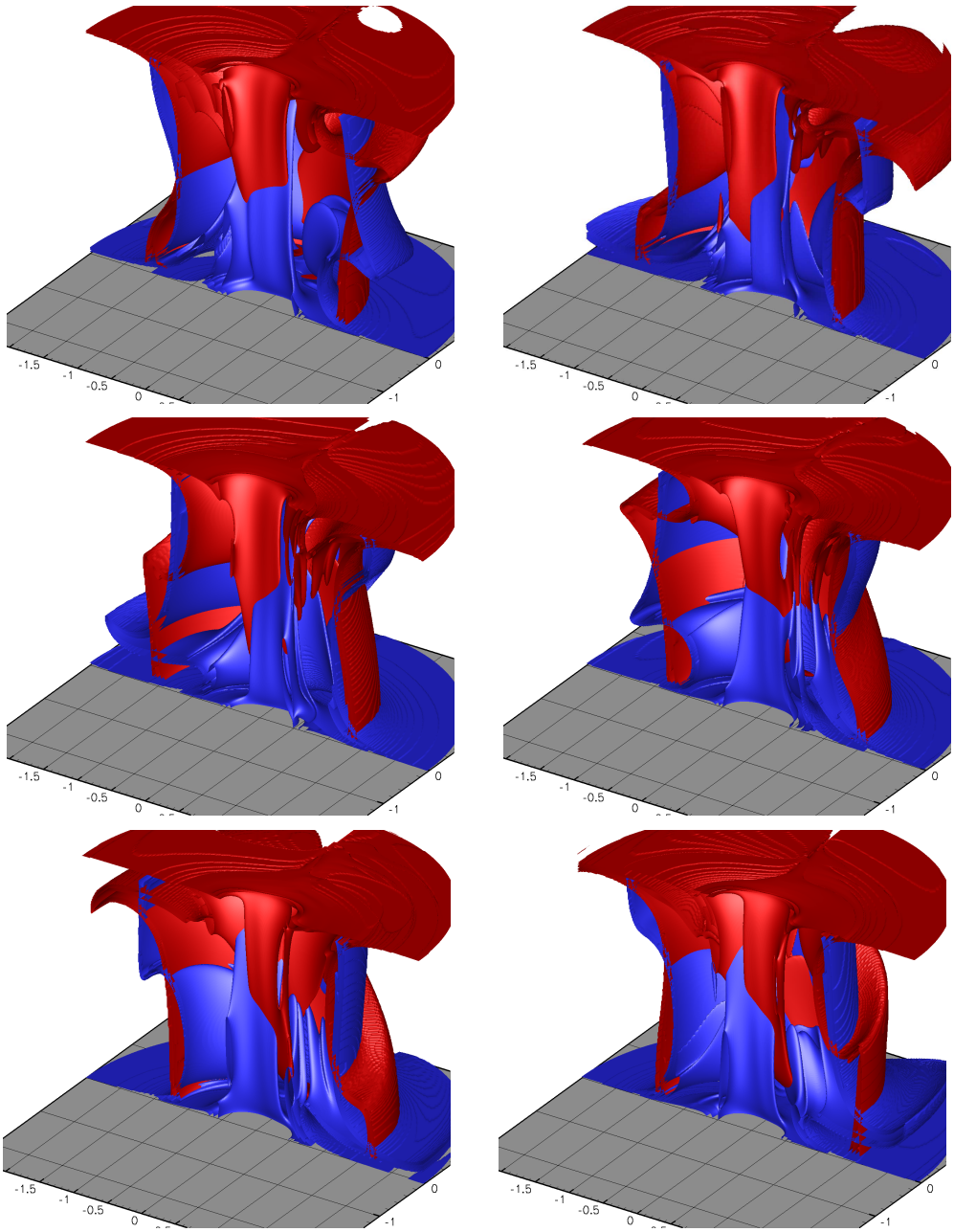

Figure 3.4: Attracting (blue) and repelling (red) LCS for a dynamical model of Rayleigh-Bénard convection in a cylinder. The vertical section reveals the complex entanglement of the lobes inside the center cell. Transport of particles can be derived from the dynamics of the lobes, which are the extensions to higher dimensions versions of heteroclinic tangles.

geometry, properties, and transport can be directly extracted from two-dimensional, time-periodic lobe dynamics theory introduced in [86, 88].

The lobe dynamics framework can be adapted to time-chaotic forcing $g(t)$, such as the one used in this chapter. A detailed description can be found in [14]. In higher dimensions, the construction of the lobes is subject to many difficulties described in [5]. For the specific model studied in this chapter, the invariance of the moving radials guarantees, however, that the three-dimensional system is rigorously equivalent to the superposition of two-dimensional slices. As a result, the primary intersection manifold used to define the sequence of lobes in [5] is smooth and closed. There exist well-defined disjoint lobes on each sides of the LCS and the motion of these lobes is the only mechanism to enter or leave the center cell.

Fig. 3.4.2 shows the inside of the separatrix and reveals highly convoluted lobes. In particular, lobes have secondary intersections, which explains how complex, chaotic dynamics can take place in such a structured system [86]. Since the goal of the definition in this chapter is to find hypersurfaces that locally maximize the Lyapunov exponent, it is evident that the system is sensitive to initial conditions in a neighborhood of the LCS. Although there does not exist any formal theorem to support this assertion, it should be clear from Fig. 3.4.2 that a chaotic Cantor set is expected to be found in the entanglement of the two LCS. Smale and Morse proved the existence of chaos near the hyperbolic manifolds of two-dimensional periodic systems [98, 28]. The extension to time-chaotic systems [6] and higher-dimensional systems [5] is work in progress, but the computation of LCS in various systems already reveals that such chaotic motion is the general behavior in the vicinity of intersecting LCS, regardless of the dimension of the space or the time-dependence of the vector field.

3.5 Conclusions

This chapter extends the ideas and proofs presented in the previous chapter to n-dimensional systems. Here, LCS are defined as co-dimensional 1 maximizing surfaces of the FTLE field, which is made precise in Def. 3.2.1. It is shown that the quasi-invariance of the LCS shown in the previous chapter is independent of the number of dimensions of the system. These results are applied to a dynamical model of Rayleigh-Bénard convection based on the model of Solomon and Gollub.

The ability to compute LCS for systems with dimensions higher than two has important practical appeal. Previous dynamical systems methods have mostly been applied to 2-D applications; even when the method is capable of being extended to higher dimensional systems (see [70] for an exception). However, a vast majority of interesting unsteady fluid systems are inherently 3-D. The method presented in this chapter has no inherent limitation imposed by the dimension of the system. It is important to note though that the computational cost goes exponentially with the dimension of the system based on current computation techniques used to produce the results shown here.

Therefore, to ensure that the method presented in this chapter can be used as a practical tool in the analysis of unsteady systems, with dimensions higher than two, it is important to develop efficient numerical methods. This is currently an active area of research being pursued by the authors. While fluid systems, which have been the main application area for these methods, are inherently 2- or 3-D, visualization of LCS for 3-D systems becomes much more complex as well. However recent advances in 3-D visualization tools can be utilized to help interpret LCS in 3-D systems.

Chapter 4

Computation of FTLE and LCS

This chapter provides an overview of the numerical implementation of FTLE and LCS and some computational concerns. The purpose of this chapter is to allow readers the ability to reproduce the algorithm used to provide the results shown in this thesis.

For many practical applications, especially in the realm of fluid dynamics, the dynamical system is given by a discrete set of data, which is often obtained from CFD simulations or empirical measurements. This chapter assumes that the dynamical system is given by such a finite data set.

4.1 Algorithm Overview

The algorithm starts with the initialization of the FTLE computational grid, $X(t)$. This represents the discrete locations in space, at time t, over which FTLE is computed; in most of the examples shown in this thesis, a Cartesian mesh is used. Note that the domain spanned by these points must be a subset of the velocity field domain. Next, the points in this grid are treated as initial conditions for integrating the velocity data. For most examples shown in this thesis, a fourth-order Runge-Kutta-Fehlberg integration algorithm [81] is used to integrate the points from their initial locations to their final locations after the FTLE integration length T. When working with velocity data sets where the value of the field is only known at discrete locations, interpolation must be used to integrate the FTLE grid. For most examples in this thesis, a third-order interpolator [50] was used.

Once the final positions, $X(t+T)$, are computed, the spatial gradient of the flow map can be evaluated at each point in the **initial** FTLE grid by finite differencing with values at the neighboring grid points. For example, for a planar system, let $(x_{ij}(t), y_{ij}(t))$ denote the position of the (i,j)-th point in the FTLE computational grid at time t. This point then gets advected to $(x_{ij}(t+T), y_{ij}(t+T))$ after T time units. Assuming a cartesian FTLE grid and using central differencing, the spatial

gradient of the flow map at $(x_{ij}(t), y_{ij}(t))$ is given by

$$\left.\frac{d\phi_t^T(\mathbf{x})}{dt}\right|_{(x_{ij}(t),y_{ij}(t))} = \begin{bmatrix} \frac{x_{i+1,j}(t+T)-x_{i-1,j}(t+T)}{x_{i+1,j}(t)-x_{i-1,j}(t)} & \frac{x_{i,j+1}(t+T)-x_{i,j-1}(t+T)}{y_{i,j+1}(t)-y_{i,j-1}(t)} \\ \frac{y_{i+1,j}(t+T)-y_{i-1,j}(t+T)}{x_{i+1,j}(t)-x_{i-1,j}(t)} & \frac{y_{i,j+1}(t+T)-y_{i,j-1}(t+T)}{y_{i,j+1}(t)-y_{i,j-1}(t)} \end{bmatrix} \tag{4.1}$$

Once the gradient of the flow map is computed, the largest eigenvalue of the finite-time, Cauchy-Green deformation tensor is computed and the FTLE at each point is obtained from the definition of the FTLE:

$$\sigma_t^T(\mathbf{x}) \triangleq \frac{1}{|T|} \ln \sqrt{\lambda_{\max}(\Delta)} \, . \tag{4.2}$$

This procedure is then repeated for a range of times t to provide a time-series of FTLE fields.

By finite-differencing neighboring points in the grid, the gradient of the flow map (and hence the FTLE) is being approximated, or smoothed out. However, this smoothing can be desirable in obtaining rough approximations to the locations of LCS. For example, consider a generic hyperbolic point and its stable and unstable manifolds as shown in Figure 4.1. The hyperbolicity of the fixed point causes two points on either side of the stable manifold to diverge after a sufficient amount of time T; therefore we can expect high FTLE values along the stable manifold. But since the value of the FTLE can quickly decrease perpendicular to the manifold, it is possible that the *theoretical* FTLE values at $\mathbf{x}(t)$ and $\mathbf{y}(t)$ can be both quite low if the gradient of the flow map is computed from truly infinitesimal differencing. However, if the derivative of the flow map at point $\mathbf{x}(t)$ is computed by differencing with the trajectory of $\mathbf{y}(t)$ (or vice-versa), then the *computed* value will be large since these points straddle the stable manifold (i.e., LCS). Therefore, if we only know the theoretical FTLE values over a coarse grid, one would not likely see any ridges in the FTLE field since we cannot expect grid points to lie on, or sufficiently close to, the LCS. However, by differencing the computational grid as outlined above, LCS that lie between grid points should still be revealed, even for relatively coarser meshes. As a result, if one is interested in knowing the approximate location of the LCS, then a coarse grid can be used to obtain the approximate location. From there, the FTLE grid can be adaptively refined near the LCS to iteratively improve the location estimate.

To extract the LCS from FTLE fields, the Hessian of the FTLE field and the gradient lines can be computed. In the case of a Cartesian grid, the Hessian is easily computed from finite-differencing. The gradient field can be found by Morse-Smale decomposition. Once the eigenvectors corresponding to the minimum eigenvalue direction of the Hessian are computed, a scalar field can be formed by taking the inner product of these eigenvectors with the gradient field. Then ridges are extracted by looking at the zero-valued level sets. This method has been tested to varying success on simple test cases. However, having an automated capability to extract LCS from FTLE fields is currently an active area of research and is not well-developed.

Current uses for FTLE fields in computing LCS, such as shown in this thesis, are done primarily

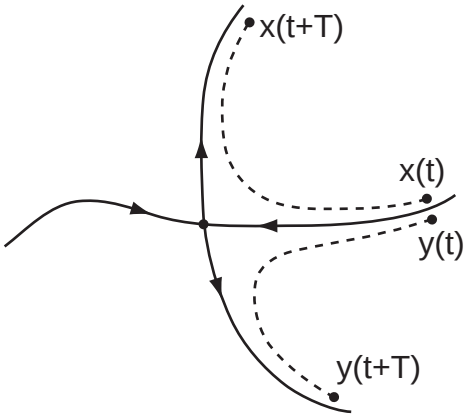

Figure 4.1: Two points on either side of a stable manifold will diverge after a sufficient amount of time.

for visualization purposes to help better understand the underlying flow geometry of unsteady systems. In such cases, it is often sufficient to visualize these structures, which in and of itself can be very revealing since the location of these structures is usually not obvious from viewing the velocity field or even the trajectories. However there is strong motivation to extract these LCS numerically. One reason is to speed computational efficiency. For example, the main cost associate with computing FTLE fields is the integration of the FTLE grid since *each point* must be advected by the flow. Therefore, it is desirable to develop an automated algorithm such that a coarse FTLE grid can be used to obtain approximate locations of LCS and the FTLE grid could then be adaptively refined near LCS locations to produce a interactively better estimate of the LCS location. This is also desirable in the sense that it will produce a final FTLE grid that is better resolved around the LCS, which would facilitate algorithms to extract the unique curve (surface in high dimensions) representing the LCS. This approach becomes even more compelling for higher-dimensional systems since the number of grid points in the FTLE grid increases exponentially with the dimension of the system.

Additionally, the automated extraction of LCS is desirable if the LCS are needed for further computations. Example of such applications might be if the LCS are used for transport computations, or optimization problems where one is trying to "shape" the LCS, or any other application where the LCS is used to drive another computation or system.

4.2 Integration Time

Two points straddling a stable manifold of a hyperbolic point typically separate much faster than other arbitrary particle pairs due to the exponential divergence they experience as they approach the hyperbolic point [40]. Likewise, two points straddling an unstable manifold will similarly have

more pronounced separation than other pairs of points when advected backward in time. This is (heuristically) why ridges of high FTLE correspond to stable/unstable manifolds in autonomous or periodic systems, or more generally repelling/attracting LCS in aperiodic flows. For example, consider the two points, $\mathbf{x}(t)$ and $\mathbf{y}(t)$, straddling a stable manifold as shown in Figure 4.1. After a sufficient amount of time T these two points will have significantly separated due to the divergence of the hyperbolic point. If we assume that these points are neighbors in the FTLE grid then this would cause the FTLE field to have a high value at these locations. Notice that if the two points were located farther up the manifold (i.e., farther away from the hyperbolic point), then a longer integration time would be needed for the points to sufficiently separate. In general, longer integration times allow more of the LCS to be revealed. For example, Figure 4.2 shows the variation in the FTLE field for the double-gyre flow considered in §2.5. Notice that as the integration time is increased, more of the LCS is revealed.

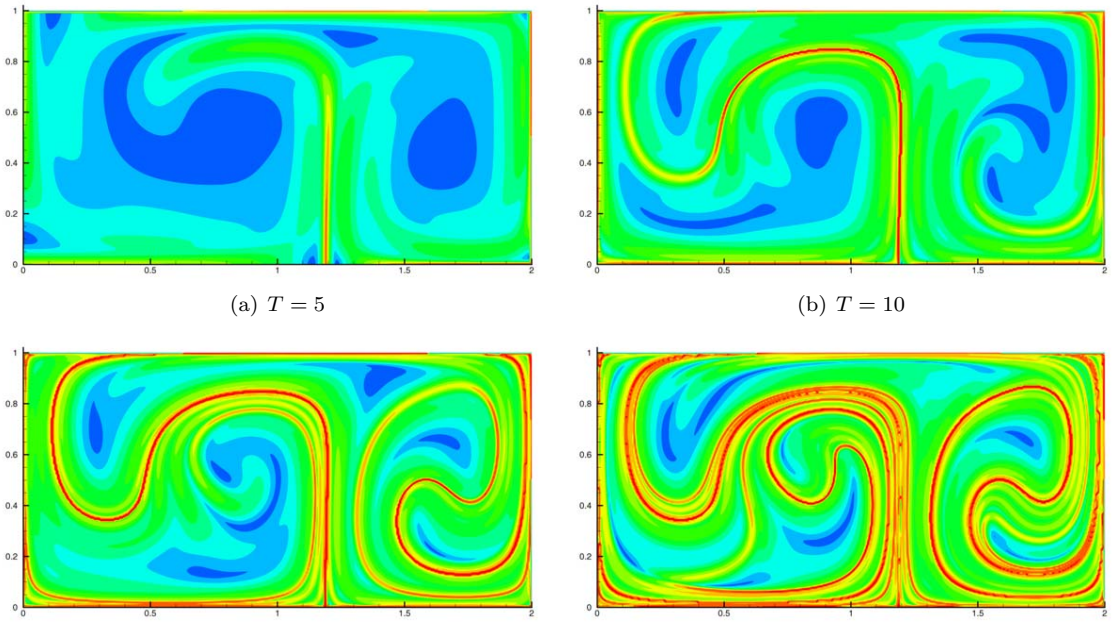

(a) $T = 5$ (b) $T = 10$

(c) $T = 15$ (d) $T = 20$

Figure 4.2: The double-gyre FTLE field at $t = 0$ for $A = 0.1$, $\omega = 2\pi$, and $\epsilon = 0.25$ for increasing integration times T.

However, both practical and theoretical concerns may bound the integration length, T. For example, the double-gyre flow can be thought of as a periodically perturbed Hamiltonian system. For such systems, the stable and unstable manifolds (i.e., LCS) are typically infinite in length, due to the periodicity of the flow [28, 88]. However, for aperiodic flows, the LCS can exist on strictly finite-time intervals, see [49] or Ch. 8 for examples. Therefore, from a theoretical standpoint, the integration length should be limited based on the system dynamics in order to resolve these finite-time structures. Practical concerns also limit the length of the integration time as well, which is

discussed further in the next section.

4.3 Practical Concerns

When the dynamical system is given by a finite data set, the vector field is only defined over a finite domain in extended phase space, i.e., $D \times I$, where D is the spatial domain of the data and I is the time interval over which the vector field is known. Interpolation of this data is needed to integrate the FTLE grid for points that remain in $D \times I$. However, unless D has a closed boundary (in the fluid-mechanics sense), some points will invariably leave the domain D as they are advected. Because it is often difficult (or impossible) to extrapolate the vector field outside of $D \times I$, the points that leave the domain cannot be integrated further. Therefore T is typically bounded by the availability of data. Furthermore, if the time at which a point leaves the domain, $t + T'$, is less than the integration end time, $t + T$, then the FTLE must be computed based on the location of the point at time $t + T'$ and the amended integration time T'. To compute the FTLE at point (i, j) in the FTLE grid, the locations of the neighboring points are needed for finite-differencing, cf. equation (4.1). Therefore, once point (i, j) leaves the domain, not only is the FTLE computation for point (i, j) done prematurely, but the computation must also be done at that time for all neighbors of point (i, j) that use the final location of (i, j) to compute their FTLE value. However, even though the FTLE has been computed for these neighboring points, they are still advected until a) they leave the domain, or b) the integration end time $t + T$ is reached, which is necessary because they may have mutually exclusive neighbors from (i, j) that rely on their final location for the FTLE computation.

Table 4.3 lists pseudocode for an algorithm that could be used as a template for developing a program to compute FTLE based on the above considerations. Depending on user interface flexibility and the choice of supporting functions, the actual code would undoubtedly be substantially longer of course.

If the dynamical system is only known over the finite time interval I, then this inherently restricts the FTLE integration length T to be less than I. However, if a point in the FTLE grid is advected outside of the spatial domain of the data before the integration length is reached, the computation of the FTLE is halted prematurely, as described above. It is often the case that most or all of the FTLE grid will be advected outside of the domain of the data set within a time interval T', such that $|T'| \ll |I|$, in which case, allowing $T > T'$ would not produce any added information. A good example of this, where the domain is quickly "flushed," is when studying flow over an airfoil, cf. §8.3.

Another practical concern that limits the integration time is the fact that because equation (4.2) assumes a linear approximation to the flow map, as the integration time increases, the grid resolution should increase. However, as the resolution of the grid increases, the computation time

```
for each OutputTime {
        set FTLEgrid.Grid array to contain positions of points in FTLE grid
        set FTLEgrid.Old array to FTLEgrid.Grid
        set FTLEgrid.New array to FTLEgrid.Old
        set FTLEgrid.FTLE array to all zeros
        set FTLEgrid.CalcFTLE array to all true
        set FTLEgrid.LeftDomain array to all false

        if any point in FTLEgrid outside velocity domain
                remove point from FTLEgrid

        for IntegrationTime = 0 : DataTimeStep : (FTLEIntegrationLength - DataTimeStep) {
                for each point (i,j,k) in FTLEgrid {
                        set t0 to OutputTime + IntegrationTime
                        set t1 to t0 + DataTimeStep
                        set FTLEgrid.New(i,j,k) to integration of FTLEgrid.Old(i,j,k) from t0 to t1

                        if point FTLEgrid.New(i,j,k) outside velocity domain {
                                set FTLEgrid.LeftDomain(i,j,k) to true
                                if FTLEgrid.CalcFTLE(i,j,k) true {
                                        Compute FTLE based on FTLEgrid.Old and IntegrationTime
                                        Set FTLEgrid.CalcFTLE(i,j,k) = false
                                        Compute FTLE at neighboring points
                                        set FTLEgrid.CalcFTLE false for neighbors
                                }
                        }
                }
                for each point (i,j,k) in FTLEgrid
                        if FTLEgrid.LeftDomain(i, j, k) false
                                set FTLEgrid.Old to FTLEgrid.New
                }
        }
        for each point (i,j,k) in FTLEgrid
                if FTLEgrid.CalcFTLE(i,j,k) true {
                        Compute FTLE based on FTLEgrid.Old and FTLEIntegrationLength
                        Set FTLEgrid.CalcFTLE(i,j,k) = false
                }
}
```

Table 4.1: FTLE algorithm.

correspondingly increases.

4.4 MANGEN

The software package, known as MANGEN for MANifold GENerator, was created at the California Institute of Technology by Francois Lekien and Chad Coulliette and provides a set of tools for analyzing dynamical systems. A nice capability of this software is the ability to easily load velocity field data sets and quickly initiate FTLE calculations. The software is publicly available and can be downloaded from `http://www.lekien.com/~francois/software/mangen/`. Additionally, there is a tutorial page on how to download and run MANGEN at `http://www.cds.caltech.edu/~shawn/LCS-tutorial/mangen.html`.

Chapter 5

Lagrangian Analysis of Fluid Transport in Empirical Vortex Ring Flows

In collaboration with John O. Dabiri and Jerrold E. Marsden

5.1 Introduction

The kinematic flow structure of two empirically measured, unsteady vortex flows is studied in this chapter using Lagrangian Coherent Structures. In particular, entrainment and detrainment of fluid is examined. The first flow considered is that of a propagating vortex ring and the second is that of the flow surrounding a free-swimming *Aurelia aurita* jellyfish. As we explain in more detail below, examples like the jellyfish show that there is a need to extend previous tools, which relied on the use of lobe dynamics that are revealed in Poincaré sections in periodic or near periodic Eulerian velocity fields, to a fully unsteady context. The purpose of this chapter is to carry out this extension by showing that the computation of LCS reveals time-dependent structures in the fully unsteady case, which play the role of heteroclinic lobe structures in the periodic case.

History of Lobe Dynamics Associated to Vortex Rings. The study of vortex rings has a long history and is reviewed in the paper of Shariff and Leonard [95]. Particularly noteworthy in that work, and in [94], is the characterization of entrainment and detrainment though lobe dynamics, which is reviewed below in §5.2.1. Motivated by the work of Leonard, Rom-Kedar, and Wiggins [51], Shariff and coworkers show, using theoretical and numerical analyses, the occurrence of heteroclinic tangles of the stable and unstable manifolds of the front and rear stagnation points in a Poincaré section of a model vortex ring [63]. The Poincaré section was constructed from the periodic motion produced by the vortex model's characteristic frequency, which corresponded to the rotation of its elliptical core. The evolution of the associated manifolds into lobes was shown to govern the

entrainment and detrainment of fluid from the vortex ring. In addition, the computed flow geometry agreed qualitatively with smoke [114] and schlieren [105] visualizations, as well as previous theoretical and numerical observations of spike formation behind vortex rings [62, 79].

Rom-Kedar and coworkers [86, 87] offered a more refined understanding of the role of lobe formation in the entrainment/detrainment processes. The analytic oscillating vortex pair studied in [87] was given by a stream function of the form

$$\Phi(x, y, t) = \Phi_0(x, y) + \epsilon\Phi_1(x, y, t)$$

where $\Phi_0(x, y)$ defines the steady flow of counter-rotating point vortices and $\Phi_1(x, y, t)$ is a time-periodic perturbation scaled by the strain rate amplitude, ϵ. Rom-Kedar, et al., proved the existence of lobe dynamics (and the associated horseshoe map), and also developed estimates of the flux rate into and out of the vortex neighborhood, and performed a detailed study of residence times of particles in, or near, the vortex pair. Krasny and Nitsche [42] went beyond the case of a strictly periodic velocity field and used point-vortex simulations to show that for vortex pairs that exhibit a well-defined fundamental oscillation frequency, this frequency can be used to construct Poincaré sections, which display the generic chaotic features, including the heteroclinic tangle geometry, found in the works of Shariff, et al. and Rom-Kedar, et al. The work of Carnevale and Kloosterziel [11] demonstrated lobe shedding from dye visualizations of vortices produced from rotating tank experiments and attributed these lobes to the same dynamical processes studied by Rom-Kedar, et al. [87], and made qualitative comparisons of the visualizations with their own numerical simulations.

Treating Fully Aperiodic Flows. What separates the current work presented here on vortex ring entrainment and detrainment from these past studies is the ability to compute the explicit geometry of the time-dependent structures that correspond to heteroclinic tangles in the periodic case, from empirical data of aperiodic vortex propagation.

The second flow considered in this chapter is that surrounding a live, free-swimming *Aurelia aurita* jellyfish. Although previous qualitative studies have indicated that these animals form vortex rings during their swimming and feeding behaviors [16, 20], there were no quantitative measurements of the associated flow velocity field available up to now. Using quantitative visualization techniques such as digital particle image velocimetry (DPIV; [1, 113]), it is now possible to obtain detailed measurements of the velocity field of such complex fluid flows.

While there is an obvious (approximate) periodicity associated with the usual motion of the jellyfish itself, there is no clear periodic structure in the Eulerian velocity field of the fluid surrounding the animal. While propagating vortex rings have, arguably, an approximate periodicity in their Eulerian velocity fields due to departures from the steady Hill or Norbury family of vortices (see

§5.2.1 for further discussion), that does not seem to be the case with jellyfish flows. In addition, the flow is not a small perturbation of an analytically known vortex flow, so perturbation methods do not appear to be the right tool for these types of problems. Of course jellyfish and other flows (for example, some cardiovascular flows [37] and microfluidic flows as well [9, 104]) are even more complex as the animal undergoes turning and accelerating maneuvers and we wish to have a tool capable of analyzing such situations as well.

As we have indicated, the theoretical and numerical studies mentioned above have been facilitated by time-periodicity (or aperiodicity with a dominant frequency [42]); empirical vortex ring flows such as those in naturally occurring biological systems will often be fully aperiodic. Another complication is that in such fully aperiodic cases, there are not always obvious equilibrium points (or other invariant structures) on which to "hang" the invariant manifolds. Hence, in these cases it is not obvious whether lobe dynamics—if they occur at all—will manifest themselves in the same manner as in the aforementioned theoretical and numerical studies. A resolution to this question is an important step toward improving our understanding of biological fluid transport, thereby enabling therapies for malfunction (e.g., cardiovascular flows [106]) and the realization of bio-inspired engineering designs (e.g., bio-inspired transportation systems).

Objective. Our objective is to apply methods of quantitative visualization, especially DPIV, to analyze empirical vortex ring flows in a Lagrangian dynamical systems framework. Using the LCS theory, the measured flows are examined to deduce lobe dynamics and their effect on entrainment and detrainment. Both a mechanical piston-cylinder vortex ring generator and live, free-swimming *Aurelia aurita* jellyfish are examined to compare the results of quasi-periodic flows previously examined to more complex biological flows of practical importance.

Although previous empirical studies have combined quantitative imaging and concepts from dynamical systems to analyze Lagrangian fluid transport [102, 110, 2], the goal here is to examine the specific phenomena of lobe formation and fluid transport in empirical vortex ring flows. The coherent vortex ring structures examined here are important both for their ubiquitous occurrence in biological flows and for the fact that, as declared by Saffman [91], the vortex ring "exemplifies the whole range of problems of vortex motion."

Outline. §5.2 reviews the role of lobe dynamics in the entrainment/detrainment of fluid to/from vortex rings and the methods used to extract this geometry from the empirical data. §5.3 describes the experimental methods used to measure the vortex ring flows generated by the mechanical piston-cylinder apparatus and the free-swimming jellyfish. §7.6 presents analysis of the empirical vortex ring flows. In that section, quantitative comparison is made with an Eulerian analysis of isolated vortex rings [17]. The chapter concludes in §5.5 with a discussion of possible extensions of these

results to more complex flows in nature and technology.

5.2 Analytical Methods

5.2.1 Lobe Dynamics

This section reviews, for the reader's convenience, lobe dynamics and its role in entrainment and detrainment in vortex rings; for more information about the fundamental theory, see [94, 87]. Henceforth, the transport of fluid particles is given a kinematic description, which can be summarized by the ordinary differential equation

$$\dot{\mathbf{x}}(t) = \mathbf{v}(\mathbf{x}(t), t) \ ,$$

where $\mathbf{v}(\mathbf{x}, t)$ denotes the Eulerian velocity field of the fluid, $\mathbf{x}(t)$ denotes the trajectory of a fluid particle and t denotes time. For the current studies, $\mathbf{v}(\mathbf{x}(t), t)$ is obtained from DPIV, as described in §5.3.

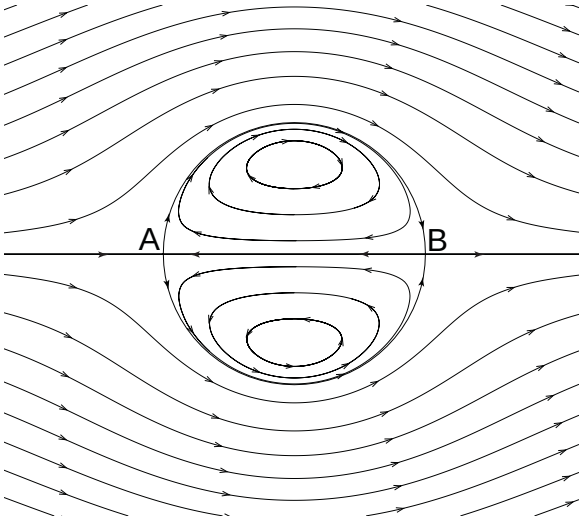

Figure 5.1: Streamlines of Hill's spherical vortex.

Figure 5.1 shows streamlines of Hill's spherical vortex [44]. The velocity field is time-independent so that these streamlines represent fluid trajectories. Point A denotes the (hyperbolic) stagnation point in what we will consider the front of the vortex and point B denotes the (hyperbolic) stagnation point on the rear of the vortex. The stable manifolds of point B are the trajectories which asymptote to point B in forward time and, in this case, coincide with the unstable manifolds of stagnation point A, i.e., the trajectories that asymptote to A as $t \to -\infty$. Such *heteroclinic* trajectories, which connect two stagnation points, are often called *separatrices* because they separate

dynamically distinct regions in the flow. The vortex ring exemplifies this standard paradigm since these trajectories separate the circulating fluid from the irrotational flow that passes around the ring. Therefore, it is reasonable to define the boundary of the vortex ring as the union of these trajectories and the associated stagnation points.

It is well-known that heteroclinic connections in time-independent systems are typically broken by the introduction of time-periodic perturbations [58, 28, 94, 95, 86, 87]. For such systems the velocity field $\mathbf{v}$ is time-dependent, albeit periodic. Typically, time-periodic systems are viewed as time-independent systems by looking at the evolution at fixed intervals of time, equal to the period of $\mathbf{v}$; that is, via a *Poincaré section*. The stagnation points A and B in the unperturbed system typically remain fixed points (perhaps slightly perturbed in position) in the Poincaré section. However the heteroclinic connection will often break and transversely intersect (in fact, in this special case one can prove that the manifolds are infinitely long and an infinite number of transverse intersections occur).

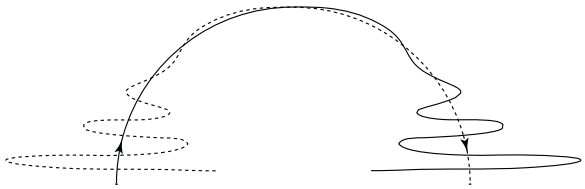

Figure 5.2: Cartoon of the heteroclinic tangle of the upper unstable and stable manifolds of the front and rear stagnation points.

Such behavior is illustrated in Figure 5.2 (see also [94, 95, 86, 87]). The unstable manifold of point A is depicted by the solid line and the stable manifold of point B is depicted by the dashed line. Notice that each manifold loops progressively back and forth as it approaches the other fixed point. To keep the illustration from becoming convoluted, only part of each manifold is shown in Figure 5.2. The intersection of these manifolds creates regions called *lobes*. Each manifold is *invariant* meaning that fluid particles do not cross these curves, or in fluid mechanics terminology, they are *material curves*. Therefore the lobes trap fluid that is confined to remain in the lobe as time evolves. The motion of these lobes can be quite predictable, which can help elucidate the transport and mixing processes.

Vortex ring generation in a real fluid typically results in more oblate structures than Hill's spherical vortex (see [19] for an exception). In general, the shape of the vortex ring will depend on the distribution of vorticity that is delivered by the vortex generator. Although this distribution is usually not linear with radial position as in Hill's spherical vortex and the Norbury vortex family more broadly [66], the flow topology in real vortex rings is similar. Therefore, in empirical flows, we might expect the appearance of patterns similar to those observed in previous theoretical and numerical studies [62, 79, 94, 95, 86, 87, 42], as depicted in Figure 5.3. Again the unstable manifolds

are given by the solid lines while the stable manifolds are depicted by the dashed lines.

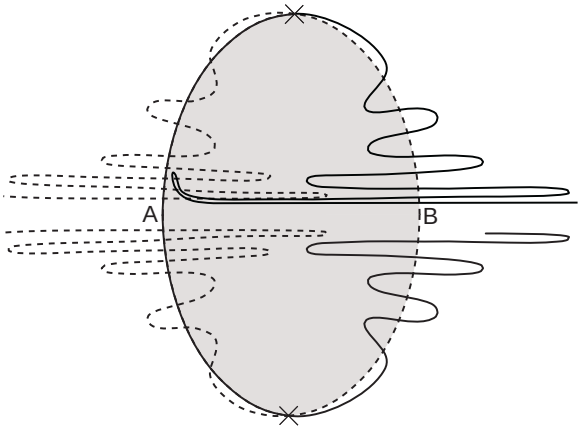

Figure 5.3: Cartoon of heteroclinic intersections for a perturbed elliptical vortex. Interior of the vortex is given by the shaded region.

To understand how fluid is transported into and out of the vortex ring, we must first define the vortex interior. There are natural intersection points of the stable and unstable manifolds that can be used [94, 87]. An X has been placed over these intersection points in Figure 5.3. The interior of the vortex is then given by the intersection of the volumes enclosed by the unstable and stable manifolds, which is shown by the shaded region of Figure 5.3. Since the stable and unstable manifolds given in Figure 5.3 are invariant, particles on one side of a manifold must remain on that side when advected. The fluid in the interior of the shaded region is the recirculating flow. However, since there is entrainment and detrainment we know that some fluid outside the vortex will end up in the interior and *vice versa*; we next review how this occurs.

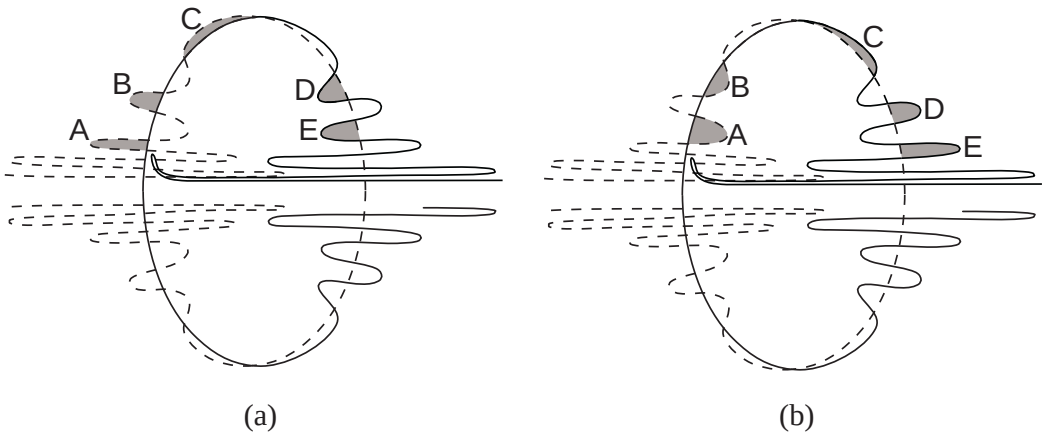

Figure 5.4: Panel (a) illustrates the process of vortex ring fluid entrainment; panel (b) illustrates the process of fluid detrainment from the vortex ring.

Lobe A, in Figure 5.4(a), is nominally outside the vortex (if one likes, the lobe below A can be taken, and so on). As shown by Shariff et al. [94], if we advect this lobe by the flow, it will

continuously deform into a lobe similar to lobe B (or gets mapped to lobe B by the Poincaré map). Further evolution by the flow will continue to deform this lobe into lobes analogous to C, D, and then E. We have thus taken a lobe that is initially located outside the vortex and shown how it is advected, or entrained, inside of the vortex. To summarize, *it is the deformation of these manifolds over time that causes the entrainment, not fluid crossing these manifolds.*

Similarly, Figure 5.4(b) shows how the detrainment of fluid from lobes initially inside the vortex to lobes outside the vortex can occur. Lobe A continually deforms into a lobe analogous to lobe E as time evolves. As time progresses, the lobes become narrower and longer, and for the case of the detrained lobes, they form thin filaments behind the vortex. As mentioned previously, these detrained spikes have been noticed in a variety of previous works [62, 79, 94, 95, 86, 87, 11, 42].

Neither stable nor unstable manifolds can self-intersect. Consistent with this impossibility of self-intersections, the lobes within the vortex will begin to wrap (fold) around the interior of the vortex, as shown by the thin lobe formed from the unstable manifold in Figures 5.3 and 5.4. As these lobes become thinner and longer, they spiral farther into the interior of the vortex. A parcel of particles on either side of the stable manifold will be stretched apart as it approaches the rear, hyperbolic point B, and it will also align with the long loops or filaments formed by the unstable manifold. This stretching and folding of fluid parcels is the distinguishing trait of chaotic mixing [69]. From these figures it should also be apparent that these entrained lobes will eventually intersect lobes that are detrained. Such *secondary intersections* explain how fluid that was once entrained can be later detrained from the vortex, see [87] for further discussion.

Although the existence of the manifolds shown in Figures 5.3 and 5.4 has been proven for near-integrable or quasi-periodic model vortex rings, and given as an explanation for the lobe shedding seen in dye visualizations of experimentally produced flows, analytic techniques have not previously been used to obtain the detailed lobe dynamics structure in empirical vortex ring flows. Such an analysis is important, for example, to be able to quantify transport rates, especially for engineering or biological applications. Relying on techniques for locating hyperbolic manifolds in aperiodic systems, we compute below the exact lobe dynamics structure in the vortex ring flows created by a mechanical vortex generator and free-swimming jellyfish. The next section addresses the experimental methods used to obtain the velocity fields of the mechanically generated vortex rings and the flow about the *Aurelia aurita* jellyfish.

5.3 Experimental Methods

5.3.1 Mechanically Generated Vortex Rings

Vortex rings were generated in the laboratory from the methods described in Dabiri and Gharib [17]. A piston-cylinder apparatus was submerged in a water tank and driven by a constant-head

flow source ($\Delta p = 8.2$ kPa). The device created vortex rings by impulsively ejecting a jet of fluid with length-to-diameter ratio $L/D = 2$ into the surrounding quiescent fluid. All of the fluid ejected during the vortex formation process created a single vortex ring, since the fluid jet length-to-diameter ratio was kept well below $L/D = 4$, the dimensionless time after which vortex ring pinch-off ensues [25]. After the formation process, the vortex ring subsequently propagated downstream under its self-induced velocity.

Flow fields created by the piston-cylinder apparatus were measured by DPIV. A meridian symmetry plane of the axisymmetric flow was illuminated by a pulsed Nd:YAG laser sheet. Glass spheres (13 micron nominal diameter) seeded in the flow reflected incident laser light onto a digital (CCD) camera oriented with its image plane parallel to the laser sheet. Particle image patterns from adjacent camera frames were interrogated by the method of Willert and Gharib [113] to determine the corresponding velocity field. Vorticity fields were subsequently computed based on the measured velocity fields. Velocity and vorticity measurements possess an uncertainty of 1% and 3%, respectively.

The physical dimensions of the vortex generator (i.e., exit diameter $D_e = 2.54$ cm, exit velocity $U_e = 5.5$ cm s^{-1}) lead to a nominal flow Reynolds number of approximately $1,400$. The Reynolds number calculated based on the vortex ring circulation is slightly larger, approaching $2,000$. These parameters as well as dye visualizations of the flow indicate that the vortex rings generated in these experiments primarily exhibit laminar flow behavior [17]. Accordingly, the interpolation of the DPIV data in later analyses does not introduce artifacts in the form of spurious flow features. To be sure, a comparison of measured velocity fields at original spatial resolution (0.19×0.19 mm per pixel) and after enhancement via interpolation does not reveal any discernable differences in integrated flow parameters such as the instantaneous vortex ring circulation, or the location of critical points in the flow such as stagnation points [17].

5.3.2 Free-swimming *Aurelia Aurita* Jellyfish

Jellyfish are unique among most animals in their heavy dependence on fluid transport for both locomotion and feeding. During locomotion, the animals use the surrounding ambient fluid to create vortex rings—one during the contractile power stroke and one during the relaxation recovery stroke [16, 20]. The momentum imparted to the fluid in these vortices results in net thrust generation by the animals during locomotion. Similar vortical flows are also created by the animals to induce transport of prey and nutrients in the surrounding fluid toward the bell margin, where contact is made with the tentacles and oral appendages. This heavy dependence on fluid transport for behaviors that are critical to their survival suggests that useful design and optimization principles for effective transport [43, 18] may be uncovered by studying the physical mechanisms whereby fluid transport is accomplished. The role of vortex ring dynamics is of particular interest in this regard.

Quantitative measurements of the flow created by these animals enables a determination of whether lobe dynamics and vortex ring kinematics observed in previous theoretical and numerical models also exist in a naturally occurring biological flow which is much more unsteady.

Juvenile *Aurelia aurita* medusae (i.e., jellyfish with a characteristic bell-shaped body) were obtained from the Cabrillo Marine Aquarium (San Pedro, CA). The animals were transported on the day of quantitative visualization to a 75-gallon water tank at Caltech designed specifically to house jellyfish for DPIV measurements. A schematic of the facility is provided in Figure 5.5.

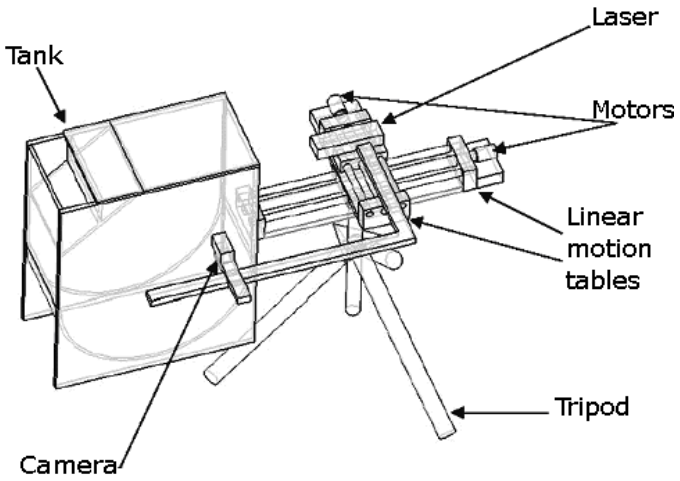

Figure 5.5: Water tank and imaging apparatus for quantitative studies of jellyfish swimming and feeding.

A small background current was maintained in the tank to prohibit the tendency for jellyfish to swim toward walls and flow conditioners, where they are susceptible to damage. Seawater of appropriate salinity ($\approx$ 35 ppm), temperature ($\approx$ 15 C), and filtrate size (less than 20 μm) was circulated by a small magnetic drive pump (Iwaki Co.). The temperature was regulated to $\pm$1 C by an inline electronic chiller (TWA Enterprises, Inc.). Organic waste created by the animals was treated by an inline canister filtration system (Nu-clear Filters). The walls of the tank were constructed from transparent acrylic to facilitate quantitative imaging experiments.

Quantitative imaging was accomplished using DPIV. A laser sheet illuminated a two-dimensional plane of the flow inside the pseudokreisel. Incident light reflected by particles in the flow was captured by a CCD camera oriented so that its image plane was parallel to the laser sheet. Brine shrimp (used as feed) dispersed throughout the water tank provided a modest signal that could in principle be analyzed by DPIV. However, to increase the signal-to-noise ratio, additional 14-micron diameter (nominally) glass beads were seeded in the water tank. These particles increased the scattering of incident laser light, resulting in higher-quality images for interrogation.

Due to the lack of control of jellyfish motion within the tank, the laser system and camera were mounted on a three-axis traverse to facilitate movement of the measurement window in accordance

with the current location of the animal in the tank. This method increased the efficiency of the data collection process, since it was not necessary to wait for the animal to swim through a fixed measurement window. However, it is important to note that the camera and laser were kept in a fixed position during the process of image capture, to ensure that the flow fields were measured with respect to an inertial frame of reference. Velocity fields were computed using the same interrogation techniques implemented for the mechanically generated vortex rings described above.

5.4 Results

5.4.1 Mechanically Generated Vortex Rings

5.4.1.1 LCS Analysis

Figures 5.6(a,b) show color contour plots of the FTLE fields computed from the DPIV data at the arbitrary time $t = 3.4$ s, with integration times of $T = -3.4$ s and $T = 3.4$ s. Time $t = 0$ corresponds to the initialization of vortex formation, i.e., the beginning of fluid ejection from the cylinder. The vortex is completely formed around $t = 1$ s and propagates from right to left as time evolves.

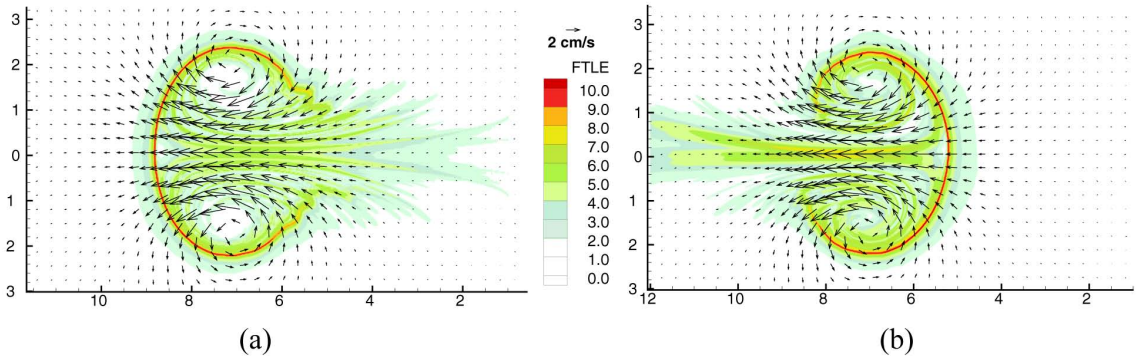

Figure 5.6: Contour plots of the FTLE fields computed from DPIV at time $t = 3.4$ s, with integration times $T = -3.4$ s and $T = 3.4$ s in panels (a) and (b), respectively. Position coordinates are specified in centimeters.

A Cartesian grid was used for the FTLE computations shown in Figure 5.6, with uniform spacing of 0.01 cm. The ridges of high FTLE values in each plot represent LCS. For Figure 5.6(a), the LCS is an attracting LCS (aLCS) since $T < 0$, and for Figure 5.6(b) the LCS is a repelling LCS (rLCS) since $T > 0$. The aLCS is analogous to the manifolds shown by the solid line in Figure 5.3 and the rLCS represents the manifolds shown by the dashed lines in Figure 5.3. The looping behavior of the manifolds shown in Figure 5.3 is revealed in the FTLE fields of Figure 5.6 if a longer integration time is chosen, as we will see (although it is already somewhat noticeable in the plots).

The time, $t = 3.4$ s, at which we chose to show the FTLE field is somewhat arbitrary, and the integration length $|T| = 3.4$ s is also somewhat arbitrary. For example, we could have chosen to show

the FTLE fields at time $t = 3.4$ s using integration times of $T = 2$ and -2 s. If a smaller integration time is used, then not as much of the manifold is revealed, whereas if a longer integration time is used, more of the manifold is revealed. However supposing that the data begins at $t = 0$, if we chose $T < -3.4$ s then we are restricted by the availability of data to show the FTLE field at some time $t > |T|$. Because the FTLE is a measure of the *linearized* growth rate about a trajectory, as $|T|$ becomes larger, the resolution of the FTLE computational grid typically must be increased. The integration length of $|T| = 3.4$ s was chosen because it is long enough to reveal the boundary of the vortex ring, yet short enough to keep the plot (and computation) from becoming overly complicated.

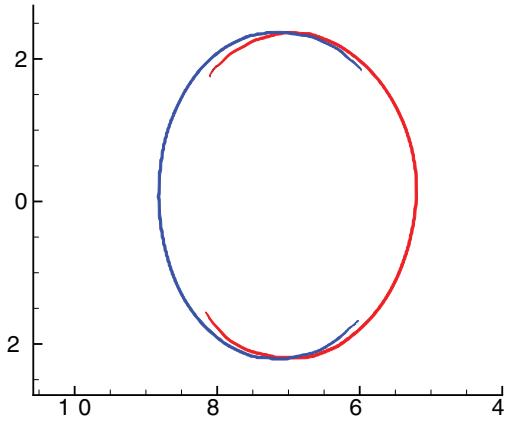

Figure 5.7: Intersection of aLCS (blue curve) and rLCS (red curve) define vortex interior. Shown for $t = 3.4$ s.

Superimposed on the FTLE contour plots of Figure 5.6 is the DPIV velocity field data at $t = 3.4$ s. Notice that it is impossible to define a vortex boundary from inspection of the velocity field. If we plot the two LCS given in Figures 5.6(a,b) together, we obtain the plot given in Figure 5.7. The LCS, up to their intersections, provide a well-defined vortex boundary, as suggested by Shariff et al. [94] and Rom-Kedar et al. [87]. These LCS can be thought of as material lines [93], such that transport is locally tangent to these structures. They separate the circulating fluid, which moves downstream with an average velocity equal to the speed of the vortex from the rest of the fluid. Because the LCS are time-varying, it is the deformation and interaction of these coherent structures which allows fluid to be entrained or detrained, cf. [94, 87].

If the FTLE field shown in Figure 5.6(b) is computed from a longer integration time T, we can obtain the LCS shown in Figure 5.8, where we have zoomed in to the lower left hand corner of the vortex ring. The rLCS loops progressively back and forth. The intersection of this looping with the aLCS creates lobes. These empirical data are sufficient to validate previous theoretical and numerical predictions regarding the transport of fluid into and out of the interior of the vortex ring via the evolution of these lobes. The following analysis accomplishes this.

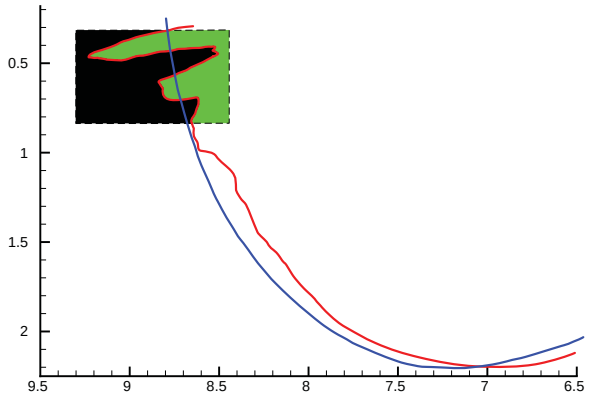

Figure 5.8: Looping of the rLCS. Superimposed is a rectangular parcel of fluid.

Suppose we place a rectangular parcel of fluid particles in the measured flow at time $t = 3.4$ s and locate the parcel as shown by the dashed rectangle in Figure 5.8. The vortex boundary is given by the aLCS (at least up to the intersection point of the two manifolds in the bottom right-hand side of the plot, cf. Figure 5.7). Thus the parcel of fluid intersects the interior and exterior of the vortex. Using the Eulerian velocity field description from DPIV, it would be impossible to determine specifically which particles are entrained, detrained, or remain inside or outside the vortex. However, we can make such a prediction from the LCS derived from the measured vortex ring flow. The particles in the rectangular parcel located "outside" the rLCS at time $t = 3.4$ s are darkly colored, and those located inside the rLCS at that instant are lightly colored. The aforementioned theoretical and numerical results predict that as time evolves, all the lightly colored particles—even those outside the vortex ring at this instant—are entrained into the vortex interior, and all darkly colored particles—even those inside the vortex ring at this instant—will be left in the wake.

Figure 5.9 shows the time evolution of this parcel of fluid particles (as dictated by integrating the measured velocity field from DPIV) with the time evolution of the LCS. The LCS are shown by plotting the FTLE fields as in Figure 5.6 but shading all level sets below some upper threshold white, and coloring the upper level sets for the forward and backward time FTLE fields. Figure 5.9(a) shows the initial location of the parcel, which is composed of 16,110 particles, with 10,250 darkly colored and 5,860 lightly colored. The parcel initially becomes stretched into a thin filament as it is advected around the bottom of the vortex, cf. Figure 5.9(b). As the parcel propagates up the other side of the vortex (which is itself moving relative to the laboratory frame), it forms lobes that are dictated by the looping of the aLCS. The looping of the aLCS is not shown in Figure 5.9, but one can easily see its effect from the "spikes" formed by the parcel as it approaches the rear of the ring. As mentioned previously, the name attracting-LCS implies that a parcel placed about this manifold will align with the manifold over time and analogously a parcel placed over the repelling-LCS is stretched apart as time evolves. As the parcel continues to be advected by the flow, the lightly colored particles are

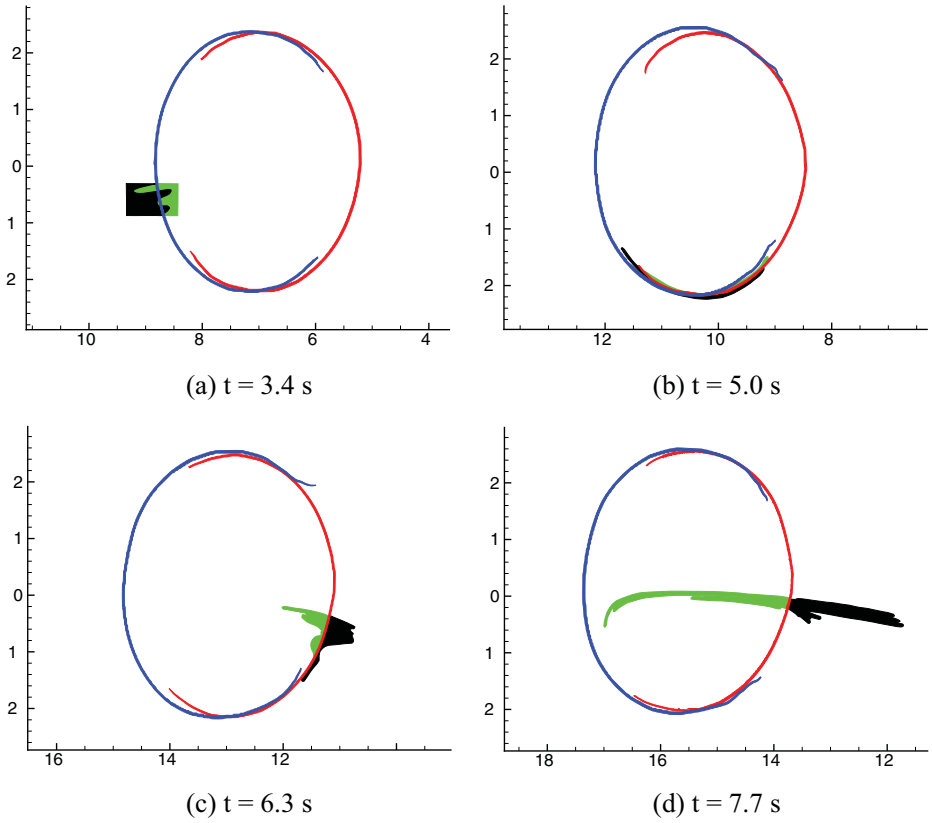

(a) t = 3.4 s (b) t = 5.0 s

(c) t = 6.3 s (d) t = 7.7 s

Figure 5.9: Evolution of lobes in empirical vortex rings.

entrained into the vortex while the darkly colored particles are detrained and left behind the vortex, Figures 5.9(c,d). A movie of the evolution shown by the snapshots of Figure 5.9 can be found at `http://www.cds.caltech.edu/~marsden/research/demos/`.

In Dabiri and Gharib [17] a variety of counter-flow protocols were implemented to alter the vortex ring dynamics. These protocols were comprised of adding a constant counter-flow initiated some time after vortex formation was initialized by the piston-cylinder apparatus. While these flows were more unsteady than the one analyzed above, LCS computed from data of these experiments all revealed lobe dynamics qualitatively similar to the no counter-flow experiment analyzed here, thus demonstrating the robustness of these results.

In the works of Shariff, et al. [94, 95], Rom-Kedar, et al. [87], the heteroclinic tangle geometry was obtained from vortex ring models and was revealed on Poincaré sections by exploiting the periodicity of the flow. In the simulations of the axisymmetric flow studied by Krasny and Nitsche [42], a dominant frequency existed that was used to develop a Poincaré section, but it was clear that the unstable manifold evolved according to lower sub-harmonics, creating a more convoluted picture than the entanglement shown in [94, 95, 87]. However, the heteroclinic geometry for the flow considered here is based on empirical data and shows the *time-dependent geometry* of the entanglement without the need for Poincaré sections. This capability is important when periodicity is lacking, such as in the counter-flow experiments discussed above, or in the case of the swimming jellyfish studied below. Additionally, it is important to note that in aperiodic systems, the "stable and unstable manifolds" (more properly rLCS and aLCS) need not be infinite in length as in the periodic cases. Furthermore, it is not clear that lobe dynamics need exist in aperiodic flows in general. Along these lines, Joseph and Legras [40] studied the Polar Vortex using finite-size Lyapunov exponent fields to reveal LCS that demarcate a boundary of the vortex. Although the Polar Vortex has a monopole structure rather than the dipole configurations studied here (and other flow structures present) it was nevertheless shown that lobe dynamics were present, albeit much more faintly than for the flows considered here.

Although the mechanically generated rings are approximately axisymmetric, non-idealities in the experimental setup, such as reactive forces generated during the experiment or non-quiescent ambient fluid, lead to slight asymmetries in the axial direction. These asymmetries manifest in the slight ordinate asymmetry of the FTLE fields, cf. Figure 5.6. However, it is expected that swirl is negligible for the flow of the mechanically generated vortex rings because swirl would only become noticeable further downstream from the evolution studied here [19]. Therefore it is justifiable to study the evolution of the LCS on two-dimensional sections, however it is most desirable to understand the three-dimensional geometry of these structures. Such a three-dimensional geometry is *intuitively* some slightly deformed surface-of-revolution of the two-dimensional sections shown here, but knowing for example how lobe volume varies radially, or how the intersections of the LCS vary radially is

important for understanding transport rates. The need for such a three-dimensional view becomes more compelling when the flow becomes more radially asymmetric, such as in the case of the jellyfish, cf. §5.4.2.

5.4.1.2 Comparison with Eulerian Analysis

The use of instantaneous streamlines as an accurate representation of flow kinematics is valid strictly for steady flows. However, previous measurements of isolated vortex ring propagation [17] suggest the possibility of applying such methods to approximately describe quasi-steady flow. In that case, the vortex boundary was determined by plotting streamlines of the measured flow in a reference frame propagating with the vortex ring. The cross-sectional area of the vortex ring was determined from an elliptical curve fit to the (instantaneous) front and rear stagnation points of the vortex ring as well as its radial extent. It is useful to compare the fidelity of the present LCS methods with quasi-steady flow kinematics determined from such an Eulerian analysis.

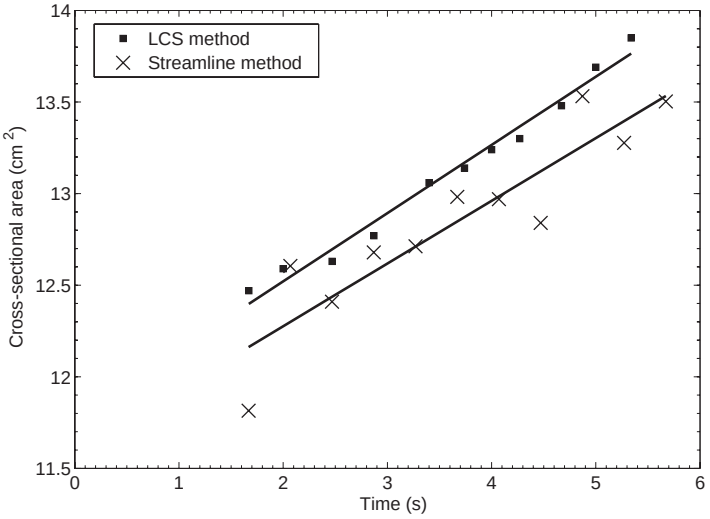

Figure 5.10: Cross-sectional area of vortex interior as a function of time as measured from the streamline method [17] and the LCS method described in § 7.6.

Figure 5.10 plots the temporal trend in vortex ring cross-sectional area measured from the previous Eulerian analysis [17] along with data measured from the LCS method described above. The two trends are in close agreement, indicating the expected result that the Eulerian and Lagrangian analyses converge in the limit of steady flow. However, measurements from the LCS method tend to be less noisy. More importantly, the LCS method provides much more specific information regarding the transport of fluid (e.g., the results of the previous section §5.4.1) and it is not limited by flow unsteadiness as with the Eulerian perspective.

5.4.2 Free-Swimming *Aurelia Aurita* Jellyfish

Figure 5.11 plots measurements of the velocity field and instantaneous streamlines generated by a free-swimming *Aurelia* jellyfish observed from the methods described in §3.2. The vortical wake behind the animal is visible and exhibits a flow geometry consistent with previous dye visualizations [16, 20]. However, this Eulerian perspective provides no quantitative indication of the geometry of fluid transport, e.g., the magnitude or distribution of fluid transport between the animal and its surrounding, or the presence of lobe dynamics.

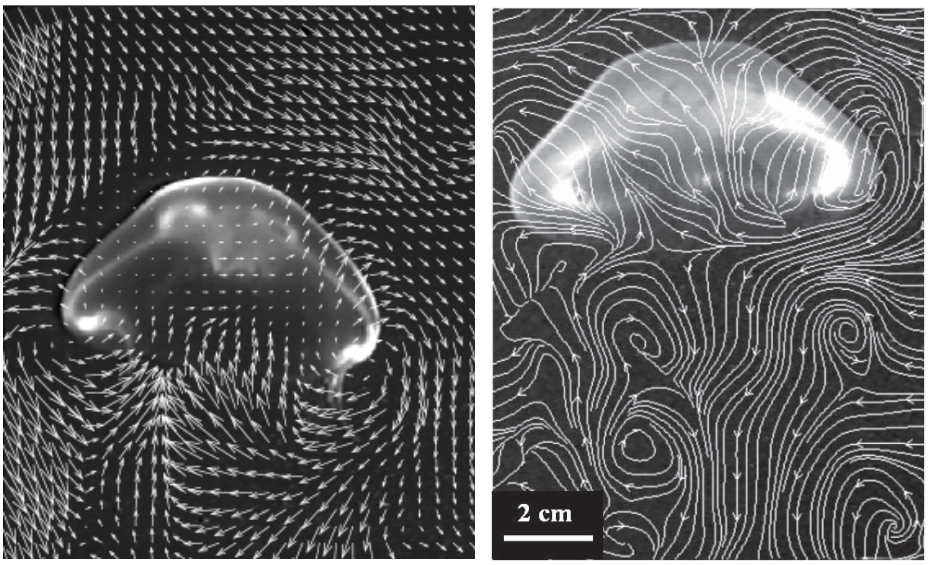

Figure 5.11: Panel (a) shows DPIV measurements of the velocity field surrounding a free-swimming *Aurelia* jellyfish at an arbitrary time in its swimming motion. Panel (b) shows the instantaneous streamlines of the flow in the wake of a jellyfish similar to the one in Panel (a).

FTLE fields were computed from the DPIV data in a manner similar to what was described above in §5.4.1 for the mechanically generated rings. Figure 5.12(a) shows the FTLE field at a given instance in the neighborhood of the jellyfish. A very noticeable LCS exists in the FTLE field. Figure 5.12(b) plots the LCS (at a slightly later time) over the location of the jellyfish. In addition to discovering the existence of a closed region of the flow in contact with the sensory apparatus of the animal (in the sub-umbrellar region), the LCS also reveals the presence of lobe dynamics. An analysis similar to that in Figure 5.9 demonstrates that the lobes formed at the upstream end of the animal dictate which portions of the ambient fluid are sampled by the animal (via passive filter-feeding and prey capture) and which portions pass by the animal without interacting, as shown in Figure 5.13. A movie of the evolution shown by the snapshots of Figure 5.13 can be found at `http://www.cds.caltech.edu/~marsden/research/demos/`. The computations presented here were repeated on a second set of data collected from a similar jellyfish experiment, resulting in

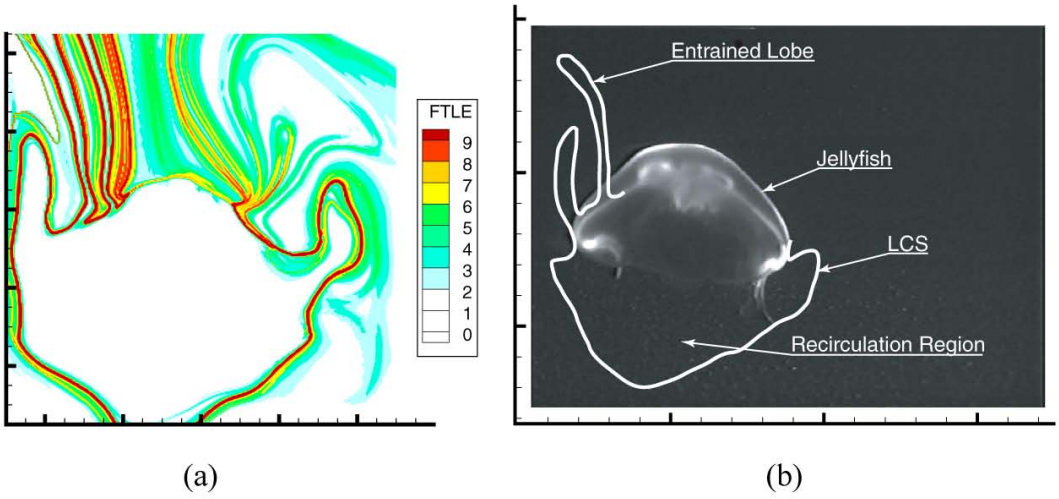

Figure 5.12: Panel (a) shows the FTLE field ($T = 13.3$ s, grid spacing of 0.04 cm) at the same time as the measurement in Figure 5.11(a). The FTLE field reveals an LCS, which is superimposed over the jellyfish at a slightly later time in panel (b). The evolution of the LCS indicates which regions of fluid are entrained and shows a recirculation zone behind the jellyfish.

similar lobe dynamics. It is important to keep in mind that the LCS shown here are cross-sections of two-dimensional surfaces that exist for the fully three-dimensional flow. Progress is currently being made on obtaining the full three-dimensional lobe dynamic geometry.

5.5 Conclusions

This chapter has shown, using DPIV data for the velocity fields of both mechanically generated vortices and the flow around a free-swimming *Aurelia aurita* jellyfish, that heteroclinic and lobe-like structures are present for fully unsteady flows. For the mechanically generated vortex rings, a computational study using Lagrangian Coherent Structures revealed lobe dynamics that were consistent with previous analytic and numeric studies, but were able to do so without the need for a perturbative assumption or periodicity or the use of Poincaré sections. Remarkably, a similar analysis applied to the measured flow about the jellyfish demonstrated qualitatively similar lobe dynamics. The lobes reveal the mechanism for entrainment in the jellyfish flow, which are critical to its feeding.

The results presented in this chapter are noteworthy not only for their important biological implications (which are beyond the scope of the present thesis), but more immediately for their ability to reveal governing fluid transport mechanisms in empirical, unsteady flows. It is reasonable to suggest that other complex flows of interest in nature and technology should be examined within the framework described here to uncover key fluid transport concepts such as lobe dynamics. In particular, flows in the cardiovascular system and microfluidics represent significant opportunities

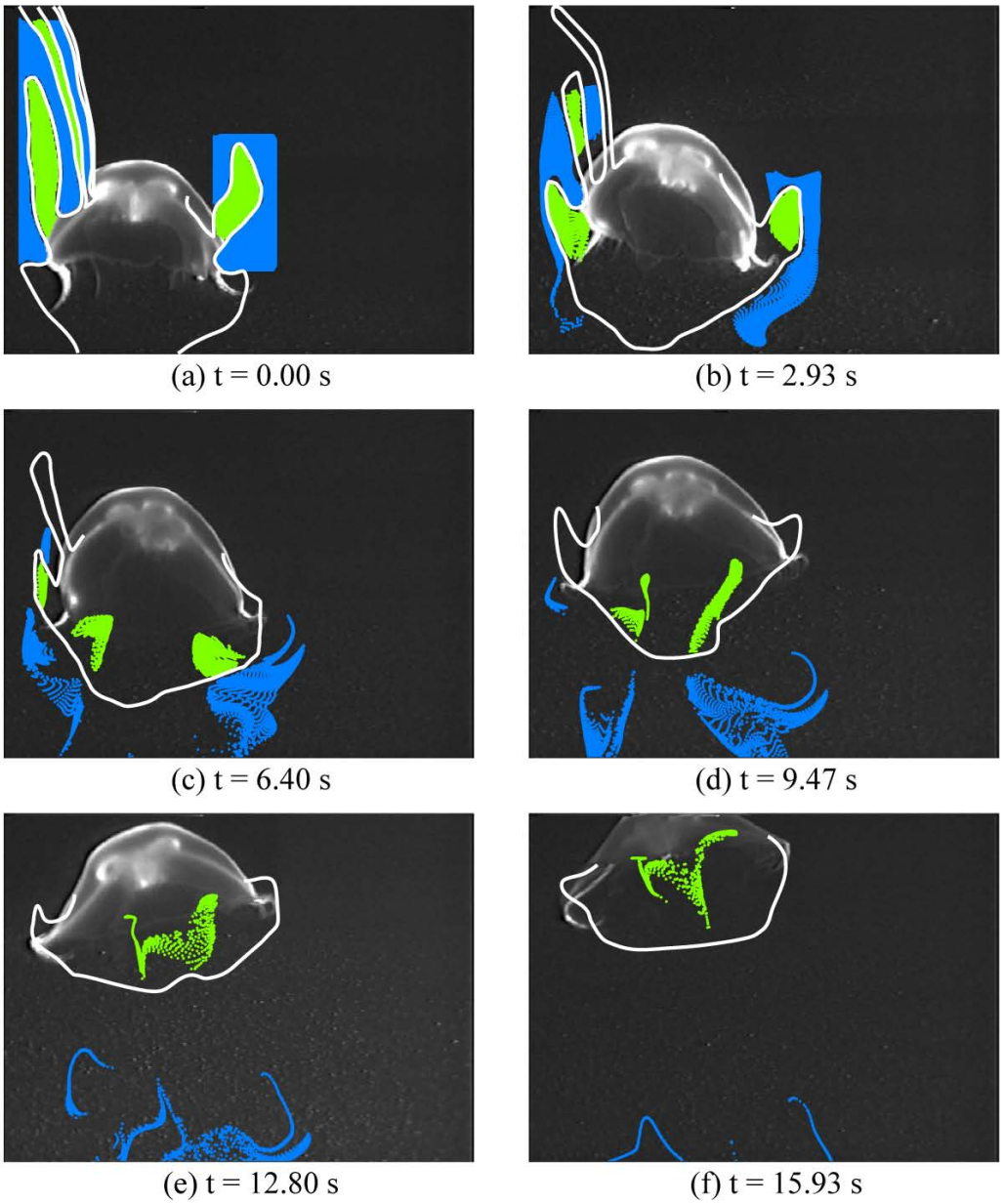

Figure 5.13: Evolution of lobes about jellyfish. The lobes distinguish which fluid is entrained into the sub-umbrellar region.

for such an analysis.

The results of the present chapter demonstrate that, in comparison with a Lagrangian analysis, much of these fluid dynamical features are missed in a traditional Eulerian analyses based on velocity field snapshots or on instantaneous streamlines. Other Lagrangian studies have primarily focused on periodic or nearly periodic model flows for both theoretical and numerical investigations. In addition, the extensions of the experimental methods to obtain velocity data, the LCS theory, and the MANGEN software to handle fully three-dimensional flows is currently underway, which will make the analyses even more interesting.

Although lobe dynamics are ubiquitous for periodically perturbed, two-dimensional, incompressible fluid flows (which are Hamiltonian systems) and for certain 3D flows as well, it is not obvious that similar geometries should occur in naturally occurring aperiodic flows. There has been a need to understand better both the conditions under which such structures arise in vortex flows of practical importance to engineering and biology, and which theoretical and computational tools can be applied or extended to study fluid transport as well as other relevant topics, such as multi-objective optimization, in such systems. This work has provided some important steps towards such interesting goals.

Chapter 6

Optimal Trajectory Generation in Ocean Flows

In collaboration with Tamer Inanc and Jerrold E. Marsden

6.1 Introduction

We propose a method for determining near-optimal trajectories in the ocean for a class of Autonomous Underwater Vehicles (AUVs) known as *gliders*. AUVs are becoming increasingly popular for collecting scientific data in the ocean. For example, they played an important role in the Office of Naval Research-sponsored Autonomous Ocean Sampling Network II project (AOSN–II) [15, 57]. There is a growing body of literature on the use of AUVs for ocean sensing; for examples, see [3, 24, 90]. However, to the best of the authors' knowledge, there has not been much work done on optimization of AUV trajectories in the presence of ocean dynamics, which is the topic of this chapter.

Gliders offer an attractive means for gathering data in the ocean because they are low cost and highly sustainable. They are designed for high efficiency and can operate autonomously, which makes them good candidates for autonomous, large-scale ocean surveys. AOSN-II employed two types of gliders, the SLOCUM and the SPRAY [90].

The trade-off for a glider's remarkable efficiency is a relatively low average speed for the vehicle. Typically, gliders move around 40 cm s^{-1} relative to the ambient water. However, the ambient water can often move at speeds the same order of magnitude as the speed of the glider. For instance, in Monterey Bay, CA, which was the location for the AOSN-II experiment, surface currents average around 20 cm s^{-1}, and are typically stronger outside the bay. Therefore it is advantageous, if not necessary, to make use of ocean currents to help propel the gliders around the ocean for sustainable missions. The idea of exploiting "natural dynamics" for vehicle transport has been used extensively in a number of research areas, such as in space mission design. For example, the natural dynamics

of the 3- and 4-body problem can be used to find efficient orbits for mission trajectories [27].

If the dynamics of the ocean are known a priori, an exhaustive optimization could be performed to numerically find an optimal trajectory each time a glider needed to move from one location to another. However the exact dynamics of the ocean are never known a priori, nor is it often practical to run such extensive computations.

We seek to propose a method for quickly determining near optimal glider trajectories based on approximate ocean current data. It will be shown that *optimal trajectories computed using the Nonlinear Trajectory Generation (NTG) software correspond to Lagrangian Coherent Structures.* These approximate solutions can then be used for either rough path planning or to initialize more detailed optimization computations. For real-time implementation, LCS must be computed from forecasts of ocean currents. However, it is reasonable to assume approximate ocean forecasts can be made [52] and LCS are robust to reasonable errors in the model forecasts [32].

The remainder of the chapter is structured as follows: First we formulate the general optimal control problem. We discuss the utility of B-Splines and the Nonlinear Trajectory Generation software to compute numerical solutions of the optimal control problem. Next we solve the optimal control problem for the case of finding an optimal path between two fixed points in the ocean. We then motivate the use of LCS to help navigate the gliders. Finally we compare our solution to the optimal control problem with a corresponding LCS.

6.2 Optimal Control Problem

Consider a general dynamical (control) system

$$\dot{\mathbf{x}}(t) = f(\mathbf{x}(t), \mathbf{u}(t)) \tag{6.1}$$

where $\mathbf{x}(t)$ is the state of the system and $\mathbf{u}(t)$ is the control input. For optimal control, we would like to choose $\mathbf{u}(t)$ such that some cost function is minimized and constraints are enforced. That is, given a cost function of the form

$$\begin{aligned} J &= \Phi_0(\mathbf{x}(t_0), \mathbf{u}(t_0), t_0) + \int_{t_0}^{t_f} L(\mathbf{x}(t), \mathbf{u}(t), t)dt \\ &\quad + \Phi_f(\mathbf{x}(t_f), \mathbf{u}(t_f), t_f) \end{aligned} \tag{6.2}$$

we would like to choose $\mathbf{u}(t)$ for $t \in [t_0, t_f]$ which minimizes J subject to equation (6.1) and constraints of the form

$$\begin{array}{lccccc} \text{Initial} & lb_0 & \leq & \Psi_0(\mathbf{x}(t_0), \mathbf{u}(t_0), t_0) & \leq & ub_0 \\ \text{Trajectory} & lb_t & \leq & \Psi_t(\mathbf{x}(t), \mathbf{u}(t), t) & \leq & ub_t \\ \text{Final} & lb_f & \leq & \Psi_f(\mathbf{x}(t_f), \mathbf{u}(t_f), t_f) & \leq & ub_f \end{array} . \tag{6.3}$$

The cost function J is composed of an initial condition cost, $\Phi_0(\cdot)$, an integral cost over the trajectory, $L(\cdot)$, and a final condition cost, $\Phi_f(\cdot)$. The constraints are similarly partitioned. *lb* and *ub* represent lower and upper bounds, respectively. Equations (6.2) and (6.3) are standard in optimal control, and are further explained in [10].

In most cases, the dynamics (6.1) and constraints (6.3) are too complicated for the minimization of equation (6.2) to be solved analytically, so numerical algorithms must be used to obtain solutions. To solve optimal control problems numerically, they are often transformed into non-linear programming (NLP) problems. The software package, Nonlinear Trajectory Generation (NTG), is very useful for transforming the optimal control problem given in equation (6.2) to an NLP problem, see [60].

6.2.1 Non-linear Trajectory Generation

If the dynamics, cost, and constraints are evaluated at discrete points in the interval $[t_0, t_n]$, it is possible to translate the optimization problem, defined by equations (6.1), (6.2), and (6.3), into the following NLP problem in C_j:

$$\min_{\vec{C} \in \mathbb{R}^p} F(\vec{C}) \text{ subject to } L \leq G(\vec{C}) \leq U$$

where $\vec{C} = [C_1 \ \cdots \ C_p]^T$. $F(\vec{C})$ is our transformed cost function, and $G(\vec{C})$ is the transformation of the constraints, with L and U being the lower and upper bounds, respectively. The discrete points, C_i, at which cost and constraints are evaluated, are known as *collocation points*.

The NTG software package, developed by Milam et. al. [60], is based on a combination of non-linear control theory, spline theory, and sequential quadratic programming. NTG takes the optimal control problem formulation, characterization of trajectory space, and the set of collocation points, and transforms them into an NLP problem. It is then solved using NPSOL [26], a popular NLP solver, which uses *Sequential Quadratic Programming* (SQP) to obtain the solution.

6.2.2 B-Splines

To facilitate numerical computation, outputs of the optimization, along with the cost function and constraints given in equations (6.2) and (6.3) are expressed in terms of B-Spline functions, see [21] for a detailed treatment of splines, and [64, 7, 61] for their use in optimal control problems.

B-Spline curves are constructed by joining *Bézier* curves with a prescribed level of continuity. The points at which the curves are joined are called *breakpoints*. The non-decreasing list of real numbers containing the breakpoints is the *knot vector*, $K = \{t_0, t_1, \cdots, t_n\}$, and n is the number of intervals. The number of times a breakpoint occurs in a knot vector is called the multiplicity, m_i. The smoothness, s_i, of a breakpoint provides the level of continuity; a breakpoint is $(s_i - 1)$ times continuously differentiable. The order, r_i, of each piecewise polynomial is $r_i = s_i + m_i$ for interior breakpoints. We will assume that the smoothness, s_i, and the multiplicity, m_i, are the same for all breakpoints.

A trajectory $\mathbf{x}(t)$ with prescribed smoothness s and order r can be written as

$$x(t) = \sum_{j=1}^{p} B_{j,r}(t) C_j \; ; \; t_0 \leq t \leq t_n \tag{6.4}$$

where p is defined by $p = n(r - s) + s$, which is the number of free parameters C_j (coefficients of the B-Spline functions) that can be used to customize the trajectory. The functions $B_{j,r}(t)$ are B-Spline basis functions defined by

$$B_{j,1}(t) = \begin{cases} 1 & \text{if} \quad t_j \leq t < t_{j+1} \\ 0 & \text{otherwise} \end{cases} \tag{6.5}$$

and $B_{j,1} = 0$ if $t_j = t_{j+1}$. Higher order terms can be found using the *Cox-de Boor* recursion formula for $r > 1$, see [21].

6.2.3 Using Temporal Constraints with NTG

While the NTG formulation allows any spatial constraint to be easily coded into the constraint set, including temporal constraints requires more care. The easiest way to solve this is to introduce time as a state variable in the optimization.

First define the new scaled time variable τ shown in equation (6.6), where t represents the true time, or old time, and T is the new state variable representing the unknown final time that will be optimized. In the setup of the optimization problem detailed in Sec. 6.3, scaled time τ rather than true time t is used:

$$\tau = \frac{t}{T} \tag{6.6}$$

After introducing the new state variable T, the cost and constraint functions given in equa-

tion (6.2) and (6.3) become

$$\begin{aligned} J(\mathbf{x},\mathbf{u},T) &= \Phi_0(\mathbf{x}(0),\mathbf{u}(0),T) + \Phi_f(\mathbf{x}(1),\mathbf{u}(1),T) \\ &\quad + \int_0^1 L(\mathbf{x}(\tau),\mathbf{u}(\tau),T)d\tau \end{aligned} \tag{6.7}$$

$$\begin{array}{rcccl} lb_0 & \leq & \Psi_0(\mathbf{x}(0),\mathbf{u}(0),T) & \leq & ub_0 \\ lb_f & \leq & \Psi_f(\mathbf{x}(1),\mathbf{u}(1),T) & \leq & ub_f \\ lb_t & \leq & \Psi_t(\mathbf{x}(\tau),\mathbf{u}(\tau),T) & \leq & ub_t \end{array} \quad . \tag{6.8}$$

Any additional temporal constraints may be expressed as a set of inequalities given by

$$lb_T \leq \Psi_T(T) \leq ub_T \qquad N_T \text{ temporal constraints.}$$

6.3 Optimal Control Example

Now that we have reviewed the formulation of the optimal control problem, let us consider a particular example. Consider the problem of finding an optimal glider trajectory between two fixed points in the ocean. Denote the starting point $\mathbf{x}_0$ and the end point $\mathbf{x}_f$. In particular, we will consider two points in Monterey Bay, CA, whose longitude/latitude coordinates are given by

$$\begin{aligned} \mathbf{x}(t_0) &= (-122.178(\text{deg}), 36.8557(\text{deg})) \\ \mathbf{x}(t_f) &= (-122.242(\text{deg}), 36.6535(\text{deg})) \ . \end{aligned} \tag{6.9}$$

For the purposes of determining the glider trajectory, a 2-D kinematic model will be used:

$$\begin{aligned} \dot{x} &= V\cos\theta + u \\ \dot{y} &= V\sin\theta + v \end{aligned} \tag{6.10}$$

where V is the speed of the vehicle, θ is direction of motion, and u and v are the components of the ocean currents in the x- and y-direction,[1] respectively. These equations represent the equations of motion given in (6.1), with V and θ being the control inputs. The pair $(u(x,y,t), v(x,y,t))$ is referred to as the (time-dependent) velocity field.[2]

The velocity field data was obtained from High Frequency Radar stations that measure surface currents in Monterey Bay, CA [74]. The data was processed by Open–Boundary Modal Analysis [47] to smooth the data and fill in missing data points.

In the NTG framework, the user needs to specify the following:

[1] Coordinates are chosen such that the x-axis is in the direction of increasing longitude and the y-axis in the direction of increasing latitude.

[2] For this analysis, we only consider two-dimensional flow, even though the ocean is three-dimensional. However, for most purposes, the z-component of the ocean is negligible.

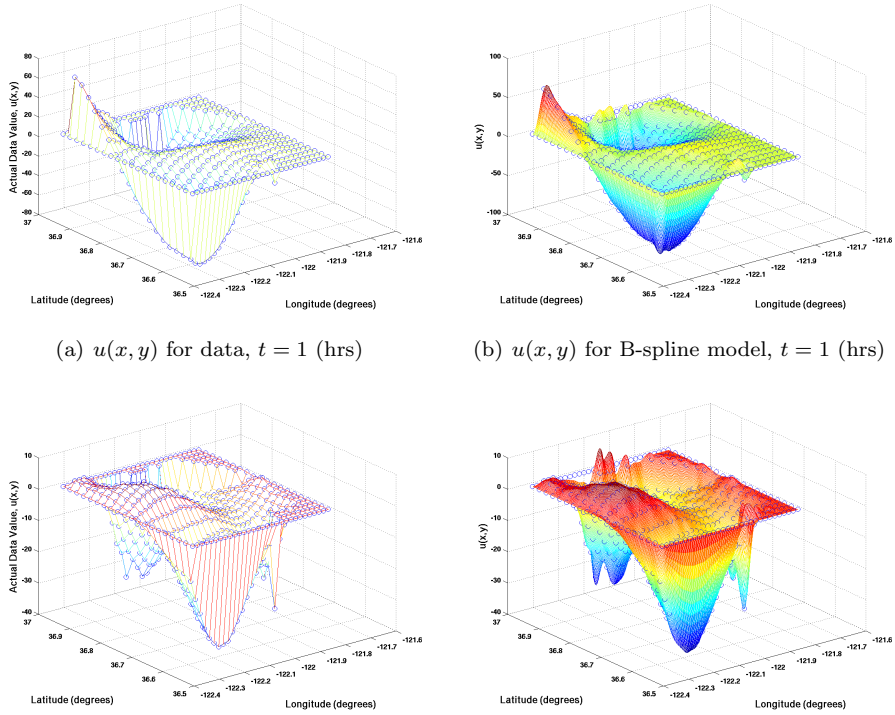

(a) $u(x, y)$ for data, $t = 1$ (hrs)

(b) $u(x, y)$ for B-spline model, $t = 1$ (hrs)

(c) $u(x, y)$ for data, $t = 4$ (hrs)

(d) $u(x, y)$ for B-spline model, $t = 4$ (hrs)

Figure 6.1: The Ocean Current Data and B-Spline Models

- Choice of outputs and their derivatives
- The cost and the constraints in terms of these outputs and their derivatives
- The regularity of the variables, placement of the knot points, order and regularity of the B-Splines, and collocation points for each output

Thus, NTG needs the derivatives of the velocity field with respect to the outputs. Numerically computing these derivatives directly from the velocity data sets can easily create convergence problems so it is best to use the tensor product B-Spline functions, allowing straightforward computation of derivatives.

The general B-Spline parameterizations for this example are given as:

$$\begin{aligned} u(x,y) &= \sum_{i=1}^{m}\sum_{j=1}^{n} B_{i,k_{ux}}(x)B_{j,k_{uy}}(y)a_{ij} \\ v(x,y) &= \sum_{i=1}^{p}\sum_{j=1}^{r} B_{i,k_{vx}}(x)B_{j,k_{vy}}(y)b_{ij} \end{aligned} \tag{6.11}$$

where a_{ij} and b_{ij} represent coefficients of the B-Spline functions for $u(x, y)$ and $v(x, y)$, respectively. $B_{i,k}$ and $B_{j,k}$ represent B-Spline basis functions for the x- and y-direction, respectively. The order of the polynomials used were $k_{ux} = k_{uy} = k_{vx} = k_{vy} = 4$ and the number of the coefficients were $m = p = 32$ and $n = r = 22$. Figure 6.1 shows u(x,y) from ocean current data and the B-Spline

representations at times $t = 1$ and $t = 4$ hours.

The cost function for this problem is a weighted sum of a temporal cost and an energy cost as follows:

$$\begin{aligned} J &= W_t T \\ &\quad + \int_0^1 W_u \left(\left(\frac{\dot{x}}{T} - u \right)^2 + \left(\frac{\dot{y}}{T} - v \right)^2 \right) T d\tau \end{aligned} \tag{6.12}$$

where $\dot{x} = dx/dt$. Note that the T terms in the integral are due to introducing time as a state variable in the NTG formulation. Integral bounds range from 0 to 1 from the re-scaling transformation. W_t and W_u represent the weighting on the total mission time and energy expenditure, respectively. Constraint functions are given as:

- (Linear) Initial Constraints:

$$-122.1780 - \epsilon(\text{deg}) \leq x(0) \leq -122.1780 + \epsilon(\text{deg})$$

$$36.8557 - \epsilon(\text{deg}) \leq y(0) \leq 36.8557 + \epsilon(\text{deg})$$

$$0 \leq T \leq 48 \text{ hours}$$

- (Linear) Final Constraints:

$$-122.2420 - \epsilon(\text{deg}) \leq x(T) \leq -122.2420 + \epsilon(\text{deg})$$

$$36.6535 - \epsilon(\text{deg}) \leq y(T) \leq 36.6535 + \epsilon(\text{deg})$$

- (Nonlinear) Trajectory Constraint:

$$1 \leq W_v \frac{1}{T^2} \left(\left(\frac{dx}{d\tau} \right)^2 + \left(\frac{dy}{d\tau} \right)^2 \right) \leq 1600$$

where ϵ is a small positive number and W_v represents the weighting on the velocity of the glider.

The linear initial constraints serve to define the start position of the glider and initialize the time. Linear final constraints restrict the final destination point of the glider. The non-linear trajectory constraint limits the velocity of the glider to a maximum relative velocity of 40 (cm/s).

To understand how W_t and W_u affect optimal solutions, consider the differences between trajectories from heavily weighting energy as opposed to time. Figure 6.2(a) compares trajectories that range from $W_t >> W_u$, in the solid line, to $W_t << W_u$ in the dotted line. As expected, the trajectories are more direct when time is weighted more than energy. We see that weighting energy

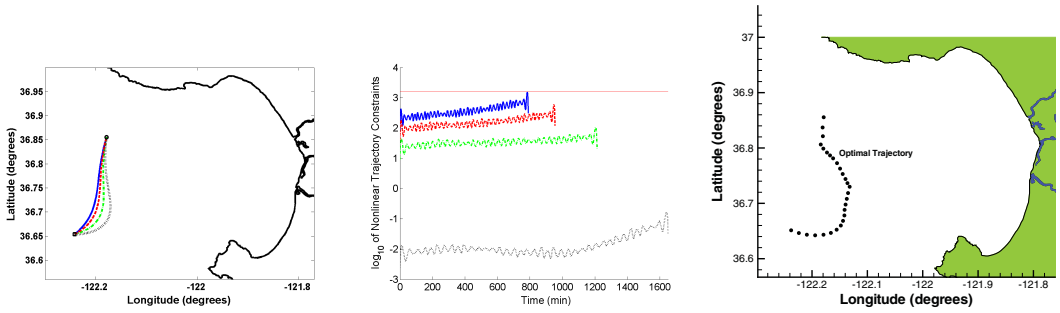

(a) (b) (c)

Figure 6.2: Panel (a) shows four trajectories with varying emphasis on W_t and W_u, the solid line is for $W_t >> W_u$ and the dotted line for $W_t << W_u$. Panel (b) shows the trajectory constraints of the four trajectories shown in panel (a). Panel (c) shows the receding-horizon optimal trajectory.

causes the trajectories to deviate from a straight line, which indicates the effect of ocean currents.

One can see an even more striking distinction between these trajectories by comparing the plots of their non-linear constraint functions shown in Figure 6.2(b). The constraint values are plotted on a log-scale and that the square-root of the non-linear constraint gives the relative speed of each glider. Upon close inspection, one will notice that the minimum-time glider shown by the solid blue line moves on average about three times faster (relative to the water), and over a shorter path, than the glider represented by the green dashed-dotted line. But remarkably, the total trajectory times between these two only vary by about 30%. Therefore, one can decidedly conclude the utility of the currents in the energy-optimal solutions. This motivates the need for a systematic way to utilize the ocean currents for navigating the gliders. This is accomplished by the help of Lagrangian Coherent Structures in the ocean.

6.3.1 Receding-Horizon Optimal Trajectory

The parameterizations given by equation (6.11) do not incorporate the time dependence of the currents. To build in the time dependence of the velocity data into NTG, we assume the velocity fields are constant over hourly intervals. For example, at time $t = 0$ an optimal trajectory from $\mathbf{x}(t_0)$ to $\mathbf{x}(t_f)$ is computed assuming the velocity field given at $t = 0$ does not change in time. Denote this trajectory $\hat{\mathbf{x}}_1(s)$. Then another next trajectory, $\hat{\mathbf{x}}_2(s)$, is computed by letting the initial point be $\hat{\mathbf{x}}_1(1 \text{ hour})$ and keeping the same endpoint $\mathbf{x}(t_f)$ while assuming the velocity field given at $t = 1$ hour is constant in time. Continuing, we let the optimal trajectory, $\mathbf{x}_{\text{opt}}(s)$, be the concatenation:

$$\mathbf{x}_{\text{opt}}(s) = \begin{cases} \hat{\mathbf{x}}_1(s) & \text{for } 0 \le s < 1 \\ \hat{\mathbf{x}}_2(s) & \text{for } 1 \le s < 2 \\ \vdots & \\ \hat{\mathbf{x}}_n(s) & \text{for } T-1 \le s \le T \end{cases}$$

where $\hat{\mathbf{x}}_n(T)$ satisfies the terminals constraints. We think of this as a receding-horizon approach, where we update the best estimate of the currents each hour, which is reasonable since the currents do not change significantly in one hour. Figure 6.2(c) shows the complete optimal trajectory for this example, where W_u is slightly larger than W_t.

6.4 Comparison of Results

LCS can be thought of as material lines, which act as separatrices. The intuition behind this for two-dimensional, incompressible flow is that since there is high stretching about the LCS, then we must have a situation where particles on either side of the LCS are being advected into dynamically different regions of the flow, and to preserve continuity, particles on the LCS are advected along the structure. Since LCS delineate the average motion of the flow, it is reasonable to assume that they might make efficient pathways. As shown below, it turns out that this is indeed the case.

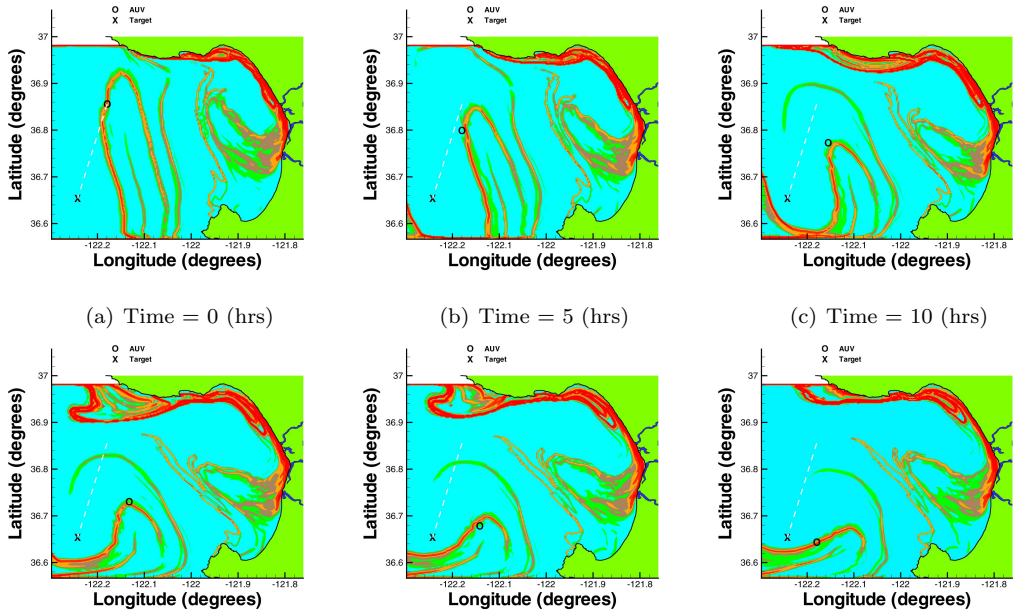

(a) Time = 0 (hrs) (b) Time = 5 (hrs) (c) Time = 10 (hrs)

(d) Time = 15 (hrs) (e) Time = 20 (hrs) (f) Time = 25 (hrs)

Figure 6.3: This figure shows the correspondence with the optimal trajectory shown in Figure 6.2(c) and an LCS. Note that the "O" in the figures near the LCS represents the location of the AUV while the "X" represents the final target location. The movie version of these figures can be found at www.cds.caltech.edu/∼shawn/animations/ACC05.html.

Now we are in a position to test the hypothesis that LCS in the ocean reveal efficient or near-optimal routes for glider transport. In Sec. 6.3 we had chosen boundary conditions (i.e., $\mathbf{x}(t_0)$ and $\mathbf{x}(t_f)$) near an LCS in Monterey Bay. In Figure 6.3 we have superimposed instances of the trajectory given in Figure. 6.2(c) with the corresponding FTLE field at that time. The figure should be thought of as snapshots of a movie that show the progression of the LCS and the progression

of the glider path together.[3] One can see that there is indeed a good correspondence between the optimal trajectory and the LCS.

This suggests something quite interesting: *One can construct approximations to optimal paths by knowing the evolution of the LCS.* It should be noted that although the initial location of the glider given in our example was near an LCS, this fortuity does not seem so contrived when one considers that LCS often correspond to geophysical fronts, such as temperature, which the gliders are meant to study [45]. Additionally, these LCS often represent separatrices, dividing regions of qualitatively distinct behavior. Therefore, gliders navigating along such dividing lines can easily switch to one or the other region with minimal control.

6.5 Conclusions and Future Work

This chapter shows that LCS provide a good correspondence with optimal trajectories for autonomous underwater gliders in the ocean. The ability to navigate gliders efficiently is very important for sustainability and keeping maintenance and operational costs low. Therefore, analyzing the evolution of LCS can be quite important in planning paths for glider trajectories. While showing the existence of this correspondence is interesting, work is being done to develop systematic ways to exploit this relation in controlling gliders in the ocean in actual experiments, such as AOSN.

Some questions that will be studied in the near future are: Can computations of optimal trajectories be sped up by using information of LCS to initialize the optimization code? How does the trade-off between optimizing energy and optimizing time affect the utility of LCS for "optimal" path planning? Also, we assumed a receding-horizon approach to integrating the currents into the optimal control, however this integration should be incorporated continuously by extending the B-spline parameterizations in time (as well as space).

[3] This movie can be found at
www.cds.caltech.edu/∼shawn/animations/ACC05.html

Chapter 7

Transport Barriers in the Ocean: Computation and Verification

In collaboration with Francois Lekien, Jeffrey D. Paduan, Jerrold E. Marsden, and Francisco Chavez

7.1 Introduction

Recent technological advances in ocean sensing have provided an abundance of data on the flow structure of the ocean. Analysis of this data often reveals many well-known *coherent structures* related to transport, such as major currents, vortex structures, upwellings, downwellings, squirts, etc. Often these coherent patterns are quite obvious from visual inspection of the data, but sometimes they are more elusive.

Recent advances in high frequency radar technology have allowed vast improvements in the measurement of surface currents. For instance it is now possible to obtain high resolution space-time measurements of the surface velocity fields in coastal regions, see [74, 96, 4, 89].

Measurements of the ocean's velocity field, $\mathbf{v}$, composes a data set that defines this field at discrete points in space and time. If we restrict our analysis to two-dimensional motion, e.g., motion of the surface of the ocean, then we write $\mathbf{v} = (u(x, y, t), v(x, y, t))$, where x and y denote the spatial coordinates in the domain of interest, t denotes time, and u and v are the components of the velocity field in the x- and y-directions, respectively. The equations of motion of a fluid particle are then given by

$$\begin{aligned} \dot{x} &= u(x, y, t) \\ \dot{y} &= v(x, y, t) \, . \end{aligned} \tag{7.1}$$

Equation (7.1) can be integrated to answer a number of interesting questions. For instance one can determine the motion of passive tracers—particles that move with the fluid, i.e., they do not actively propel themselves or have non-negligible inertia. Therefore, one can answer the question,

if a tracer is placed in the flow at a given location and time, where will it end up after some later time?

More generally, one might hope to understand if there is some underlying skeletal structure that orchestrates particles to have various fates? Since trajectories are inherently chaotic and change dramatically when the system suffers even the tiniest perturbation, direct interpretation of particle trajectories can be difficult. Therefore, looking for robust coherent patterns that dictate transport, such as separatrices that divide dynamically distinct regions, is often more enlightening, as we will show.

There have been recent developments to studying aperiodic[1] systems, which might only be defined over a finite time-interval. These techniques are based on the knowledge that transport and mixing are strongly influenced by *hyperbolicity* —the presence of both stretching and shrinking in some regions of the fluid [69].

Hyperbolic structures in the flow are characterized by how particles behave in their vicinity. There are direction(s) of significant stretching along which fluid moves away from the structure and direction(s) of attraction where particles approach the structure. In the analysis of steady systems, e.g., those derivable from a stream function, or periodic systems, hyperbolic stagnation points play a critical role. Such stagnation points have stable, and unstable, manifolds that are composed of all trajectories that asymptote to the stagnation point in forward, and backward, time, respectively. These manifolds form hyperbolic structures that typically partition finite regions of qualitatively different dynamics. For time-periodic systems, these manifolds will often interweave to provide a mechanism that stretches and folds parcels of fluid particles, which is the basis of chaotic transport [28]. For aperiodic systems, analogous stretching and elongation of fluid parcels is frequently observed, even though stagnation points may no longer be present in the time dependent field. Furthermore there are analogous "invariant manifolds" that dictate the global flow geometry, which we refer to as Lagrangian Coherent Structures (LCS).

The most common methods for computing LCS in aperiodic systems involve either locating finite-time hyperbolic trajectories and growing their their associated *finite-time invariant manifolds*, which correspond to LCS, or detecting these structures based on some local measure of hyperbolicity. Locating finite-time hyperbolic trajectories [34, 29, 54] often assumes that the time-variation of the system is benign, and leads to conditions that are difficult to verify in practical applications. Detecting LCS from local measures of hyperbolicity seems to show strong promise, especially in turbulent flows, and includes such measures as hyperbolic time, finite-size Lyapunov exponents (FSLE), finite-strain, and finite-time Lyapunov exponents (FTLE). The hyperbolic-time approach [35, 30] measures the amount of time a trajectory *continuously* repels nearby trajectories. For fully turbu-

[1] By *aperiodic systems*, we mean a system with an arbitrary time dependence, i.e., not periodic and not quasi-periodic.

lent flows, the small scale variation in particle dynamics makes this measure troublesome however. For such flows, more statistical based measures seem to be most relevant. The FSLE is a measure of how quickly initially close particles reach a specified separation. Although this measure shows promise in locating LCS [41, 40], it is somewhat cumbersome since choosing the separation criterion is highly dependent on the application. The finite-strain measure [39] and the FTLE [30, 93] and can be thought of as ways to measure the relative dispersion about a given trajectory over a finite-time interval. However, the FTLE offers a more robust measure as it nicely accounts for the *exponential separation* of fluid particles, which is key for revealing the most important hyperbolic structures.

Since it is derived from fluid trajectories, FTLE is thought of as a Lagrangian quantity, as opposed to an Eulerian quantity that is derived from the velocity field. This is an important distinction, as instantaneous fields can often be misleading when studying the kinematics of time-varying flows. For example, in such flows streamlines and actual trajectories rapidly diverge. The theoretical development of defining LCS from FTLE fields can be found in [93] where it is shown that LCS act as transport barriers, which bound regions of qualitatively different dynamics.

HF radar captures features down to a grid spacing of approximately 500 meters. Between grid points, the data is interpolated, which smooths out subgrid-scale turbulence. In addition to the smoothing, the observed data always contain some deviation or error from the true velocity field. As shown below, the techniques presented in this chapter tend to mitigate these errors. The LCS remain valid separatrices when the data is subject to large experimental errors.

7.2 Coastal Radar Measurements

The surface current mapping data used in this study was derived from a network of four CODAR-type high frequency (HF) radar systems deployed around the shores of Monterey Bay (see Figure 7.1 for locations). The systems operate on frequencies between 12 MHz and 25 MHz producing estimates of the radial current speeds approaching or receding from the radar sites. During this study, radial current data were combined on an hourly basis to estimate vector currents in the region of overlap, which extended 40–50 km offshore (e.g., Figure 7.1). The range resolution of the individual systems was 3 km and vector current estimates were produced, where possible, on a Cartesian grid every 2.5 km by fitting radial observations within a radius of 3 km from the location of the grid point. The effective depth of currents measured using any HF radar system is a weighted function of the particle motions exhibited by the Bragg-resonant surface wave constituent [72]. In the case of the Monterey Bay HF radar network, the Bragg-resonant wavelengths were between 3 m and 6 m, which implies effective measurement depths between 25 cm and 50cm using the rule-of-thumb estimate of 8% of the wavelength [103].

7.3 Lagrangian Coherent Structures

Finite-time Lyapunov exponent fields provide time-varying maps of relative particle dispersion. The FTLE is derived from particle trajectories and is therefore not an instantaneous separation rate, which is often misleading when the flow has unsteady behavior. High FTLE values indicate that there is high local stretching of fluid particle trajectories in at least one direction. In two-dimensional (surface) flows, there are typically well-defined curves of high FTLE. If one is to plot the graph of an FTLE field over the given two-dimensional domain, then these curves of high FTLE would appear as *ridges* within the graph. We define these *ridges* of high FTLE as LCS [93].

To compute the FTLE, the right-hand side of Eq. (7.1) is integrated to provide the *flow map*, $\phi_t^T : \mathbf{x}(t) \mapsto \mathbf{x}(t+T)$, which maps fluid particles from their initial location at time t to their location after some interval of time T. The symmetric matrix

$$S = \frac{\mathrm{d}\phi_t^T(\mathbf{x})}{\mathrm{d}\mathbf{x}}^* \frac{\mathrm{d}\phi_t^T(\mathbf{x})}{\mathrm{d}\mathbf{x}} \tag{7.2}$$

is a *finite-time* version of the (right) Cauchy-Green deformation tensor. Letting $\lambda_{\max}(S)$ denote the largest eigenvalue of S,

$$\sigma_t^T(\mathbf{x}) = \frac{1}{|T|} \ln \sqrt{\lambda_{\max}(S)} \tag{7.3}$$

represents the *finite-time Lyapunov exponent* at the point $\mathbf{x}$ at time t with a finite integration time T and measures the maximum stretching about the trajectory of $\mathbf{x}$ when advected by the flow.

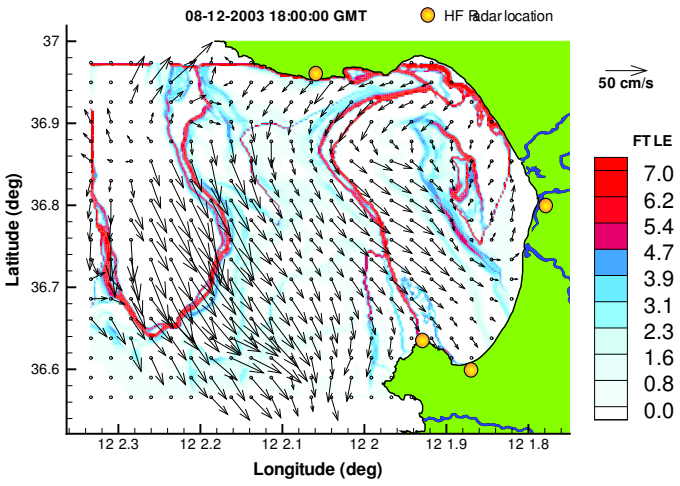

Figure 7.1: FTLE field computed for Monterey Bay, CA using HF radar velocity field data. Curves of high values of FTLE represent the time-varying LCS which act as transport barriers between flow regions. Superimposed of the FTLE field is a snapshot of the HF radar velocity field.

Figure 7.1 shows the FTLE field on August 12, 2003, 18:00 GMT computed from integrating the HF radar velocity data. A snapshot of this HF radar velocity data at August 12, 2003 18:00 GMT

is superimposed on the FTLE field in Fig. 7.1. The FTLE field was computed from the following steps: First, a 2-dimensional Cartesian grid was chosen to represent the FTLE field. The span of this grid coincides with the span of the velocity data, however the spatial resolution of the FTLE grid is ten times the resolution of the velocity data. Points in the FTLE grid are treated as fluid particles and advected by numerically integrating the HF radar velocity data from time t = August 12, 18:00 GMT to August 16, 18:00 GMT, hence the integration length is $T = 96$ hrs. This integration length satisfies the following requirements: (i) it is sufficiently large so the points of the FTLE mesh travel at least a couple of grid spacings. This is necessary to capture nonlinear effects. (ii) it is sufficiently small, so most particles of the FTLE mesh stay inside the area. The deformation tensor was then computed over the grid using finite-differencing. The FTLE was then obtained over the grid from straightforward evaluation of Eq. (7.3). The time variation of the FTLE field can then be computed by following the previous steps, but varying the evaluation time, t.

The ridges in the FTLE field, which are apparent in Fig. 7.1, represent LCS. As shown in [93], these structures are transport barriers. While any material line can be considered a transport barrier, these structures are unique in that they act as separatrices that divide dynamically distinct regions. For example consider the LCS that extends across the mouth of the Bay in Fig. 7.1. This LCS divides the flow that re-circulates within the Bay from the flow that moves down the California coast. To see this, consider Fig. 7.2. Panel (a) shows the LCS, extracted from the FTLE field on August 13, 2003, 07:00 GMT, which extends across the mouth of the Bay. Also shown is an arbitrary grid of fluid particles, for which particles that are placed to the right of the LCS are denoted by the empty circle, while particles placed to the left of the LCS are shaded. Panels (b)–(d) shows the time-evolution of these particles along with the time evolution of the LCS. The shaded particles are shown to move down the California coast and exit the domain, while the unshaded particles remain inside the LCS and recirculate within the Bay. Note that the time-evolution of the particle grid is computed independently of the LCS.

Knowing the location of the LCS, one can quickly understand the time-dependent global flow structure, and thus understand the geometry of many interesting transport driven processes. For example, LCS have been used in pollution release studies [48], optimal trajectory generation of gliders in the ocean [38], and locating scalar fronts, such as temperature and salinity [45]. LCS additionally often reveal many interesting phenomena such as large-scale eddies, squirts, upwellings, etc. The exact geometry of such flow features is often vague from quantities directly derived from Eulerian velocity fields, since such fields only represent snapshots of the unsteady flow. While the LCS provide significant information and utility, a main purpose of this chapter is the validation of LCS computed from HF radar data against the actual flow structure for the true ocean.

LCS can be thought of as a method for *visualizing* the global flow geometry of time-dependent systems. However, when working with measured data, there is the issue of whether the data used

to compute the LCS is representative of the actual flow. For example, if the HF radar data is erroneous, then it is likely the LCS will also be flawed. Additionally, small errors in the velocity field measurement typically result in large integrated errors on particle trajectories. However, LCS depict hyperbolic regions in the flow. Hyperbolic structures are usually robust to typical noise found in the ocean. Indeed, Haller showed that the LCS are not much influenced by oscillating perturbations of large amplitudes [32]. Haller's findings suggest that it is non-oscillating noise, applied during a long interval of time, that can affect the existence and shape of the LCS. In Monterey Bay, the typical lengthscale and timescale of the processes are 20 km and 2 days [90]. Therefore, it is expected that differences between the true field and experimentally measured data oscillates on a scale smaller than 2 days. Compared to the integration time $T = 4$ days, this perturbation falls into the category of fast oscillating noise that has very little effect on the LCS [32]. Thus even if trajectories obtained from integrating HF radar fields show noticeable deviations from actual tracer paths, we still expect the computed LCS to be very close to true transport barriers or separatrices present in the flow. In §7.6 data collected from drifter experiments is used to validate the LCS that are computed from HF radar data.

7.4 Drifters

The drifting buoy position data was obtained from deployments of a set of GPS-tracked surface drifters. The instruments included a cylindrical surface float approximately 1 m across that supported a holey sock-style drogue element approximately 8 m long centered around 5.5 m depth [73]. Estimates of the drift characteristics of this particular buoy suggest a drag area ratio around 20 and slip or error currents in the range 1–3 cm/sec for winds under 10 m/sec [65].

7.5 Upwelling and Relaxation

The results in this chapter span data collected during the month of August 2003. During this period, the Monterey Bay region experienced distinct upwelling and relaxation phases. Upwelling is characterized by a southward flowing filament of cold, salty water that rises from just north of the Bay and spreads southward. The prominent cause of the upwelling is strong northwesterly winds [83]. The winds were consistently upwelling-favorable from around August 6 to August 18. During August 18–22, the winds briefly calmed and reversed to a more southwesterly direction resulting in a *relaxation* state in the Bay. This causes the upwelling to disappear and results in an onshore flow in the southern portion of the Bay, which generally allows warmer water to spread into the Bay from the south. The winds switched back to upwelling-favorable toward the end of August. Stick plots of the winds are during this time-frame in Figure 7.3 at the two moorings located in the

Bay, M1 and M2.

During the upwelling stage, there is typically an LCS that extends across the mouth of the Bay, see Figure 7.1, 7.2, 7.4 or 7.5. As mentioned in §7.3, this LCS is a separatrix that divides the fluid that recirculates inside the domain from the fluid that moves down the California coast. Thus, upwelling appears to be responsible for producing recirculation of the surface fluid inside the Bay. This observation is also consistent with LCS computations on HF radar observations from an upwelling period during August 2000, which produced an analogous LCS across the mouth of the Bay. Therefore, we can consider this LCS as a *Lagrangian* footprint that the Bay is experiencing upwelling.

Around August 18, the upwelling-favorable winds calmed and reversed direction. This created relaxation-favorable conditions. During the transition to relaxation, the LCS extending from Point Piños moved southward and pushed further from the coast, for example see Figure 7.6. This allowed water in the northern region to initially be pushed further off-shore. Subsequently, the LCS moved further up the coast, causing an influx of water in the lower portion of the Bay during the days of Aug 20–23. This geometry is consistent with the dynamics typically associated with relaxation.

Toward the end of August, the winds switched back to upwelling-favorable. After a brief transient period of a couple days, a well-defined LCS extending off Point Piños develops, which is analogous to the LCS observed during the August 6–18 upwelling stage, which reaffirms the idea that this LCS is a footprint of upwelling in the Bay.

7.6 Comparison

Figures 7.4–7.7 show the time evolution of LCS superimposed with measured positions of drifting buoy paths at the corresponding times. The LCS shown in these figures were extracted from FTLE fields, similar to Figure 7.1. While there may be other LCS present in the domains shown, the ones shown are those located closest in proximity to the initial location of the drifters, as these are the most relevant. That is, drifter paths far away from an LCS do not reveal much about the flow structure near the LCS. Also shown in these figures are the predicted locations of the drifters as given by integrating their positions according to the HF radar velocity measurements of the surface currents.

Figure 7.4 shows the trajectory of one of the GPS-tracked drifting buoys, described in §7.4, with the location of the LCS extending from Point Piños. The drifter starts to the left of the LCS and moves down the California coast, staying out of the Bay, as expected based on its initial location with respect to the LCS. Additionally, there is a drifter that begins inside the LCS on August 15, 8:00 GMT, as shown in Figure 7.5. This drifter remains inside the Bay as it is advected in by the flow, which is consistent with our expectation that it should remain to the right of the LCS. Unfortunately,

the drifting buoy shown in Figure 7.5 was recovered on August 17, 6:00 GMT, preventing a longer time history to be used for the comparison.

The upward influx of water into the Bay during relaxation greatly changes the flow geometry of the surface currents, which is apparent by inspection of the FTLE fields during this time frame. For example, the LCS across the mouth of the Bay is no longer present, which indicates this southern influx of water into the interior of the Bay. During the relaxation phase, a drifter was launched at the location shown in Figure 7.6(a), which was to the left of the LCS shown in that figure. As time evolves, the drifter's position is consistent with that predicted from the LCS.

Around August 26, 2003, 09:00 GMT two drifters were released in proximity to an LCS and straddled the LCS as shown in Figure 7.7. This geometry is interesting because it can be used to get an estimate of the error between the "true" location of the LCS, and the computed location based on noisy HF radar observations. Since the two drifters are shown to diverge, with the inner drifter re-circulating and the outer drifter moving down the coast, this demonstrates that the true location of the LCS is transversed by the segment connecting the two drifters. Thus the error in the location of the LCS must be less than the distance between the computed location of the LCS and the drifter furthest from the LCS. In this case that distance is *at most* 4.5 km. However, notice that the error in the location between the drifting buoy and the location predicted by integrating the HR radar data reaches almost 14 km in just over a day. Therefore this shows the robustness of the LCS. That is, errors in the velocity data cause large deviations in the computed paths of drifters, but relatively small deviations in the location of the LCS even though it is based on trajectory information. This is due to the fact that the LCS represent the most hyperbolic trajectories in the flow, which are well-known from traditional dynamical systems theory to be robust to perturbations.

7.7 Optimal drifter release

One interesting application of LCS is to assist with tasks such as the optimal deployment of drifters. Drifters are very common to costal observatory systems and are not just used to provide Lagrangian measures of the currents, but are used as mobile arrays that can measure quantities such as temperature, salinity, fluorescence, nitrate, and scattering. As the name implies, drifters are completely subjugated to the rule of the ocean. Thus, planning effective release and recovery strategies a priori can be difficult. The authors are currently developing techniques to utilize LCS to help predict and plan release strategies to optimize drifter coverage and minimize the recovery effort.

Consider the LCS shown in Figure 7.8(a), which was obtained from computing the FTLE field on July 23, 2003, 18:00 GMT from HF radar data. We will show that a significant improvement in the utility of drifters can be achieved by accounting for the location of the LCS. To demonstrate this, two groups of drifters are placed in the Bay as shown in Figure 7.8(b). The darker-shaded

group is located on one side of the LCS and the lighter-shaded group is located on the other side. As before, this LCS can be thought of as the material line that separates the fluid that re-circulates within the Bay from the fluid that passes down the California coast or out to the open Pacific. Thus we might expect that the lightly-shaded group will remain in the Bay longer, thus providing more measurements in this area and reducing the need for frequent recovery. Figure 7.9 shows that this is indeed the case. The darker-shaded group remains relatively close together, and exits the domain of interest within about 5.5 days (thus necessitating recovery). Members in the lighter-shaded group remain in the Bay up to 16 days, nearly 3 times longer. It should be noted that when a drifter comes sufficiently close to the coastline, it is removed, i.e., considered recovered.

It would be difficult to predict a priori which drifters would remain in the bay without knowledge of the LCS. On might guess that those located further in the Bay might remain there longer, but Figure 7.9 shows that this is not necessarily the case. Of course, given velocity data for the ocean, one could compute the path of a drifter by integrating the velocity data, but this only gives information about that particular initial condition. The problem with integrating an array of initial conditions is that the resulting information is difficult to directly interpret. However, by knowing the location of the LCS, we can quickly infer where to drop drifters such that they have the desired dynamics.

Some practical concerns are worth mentioning. First, notice that even though the LCS is a moving boundary, we only have to know the location of the LCS at the release time. Thus there is no need to continually compute the LCS. Although we require future information about the surface currents to compute the LCS at the release time, this does not present an insurmountable obstacle. The integration time, T, used to compute the LCS shown in Figure 7.8(b) was three days (cf., Eq. (7.3)). However, ocean models are currently capable of making reliable predictions of the ocean dynamics within this time window. Since the location of LCS is robust to uncertainty in the velocity field, we can expect to compute a reliable estimate of the LCS location from moderately uncertain estimates. Alternatively, the movement of LCS are typically much slower than fluid particle dynamics, since on average the flow is tangential to these structures. Therefore it is reasonable to assume that time-lagged locations of LCS computed from observational data could be used in certain circumstances for real-time applications.

Although the integration time used to compute the LCS shown in Figure 7.8(b) was three days, this, remarkably, allowed us to keep the drifters inside the bay for up to 16 days. This can be attributed to the robustness of the LCS. Although it is difficult to prove that the drifters will remain in the bay that much longer than the integration time of the LCS, we can expect the LCS to persist much longer than the integration time length. Thus, if we were to take the naive approach of integrating trajectories based on ocean model predictions, we would require a much longer prediction time, which is unrealistic. Furthermore, individual trajectories exhibit a "butterfly effect", where they are highly sensitive to errors in the velocity data, whereas the locations of LCS are robust to

such errors.

7.8 Discussion

The velocity and pressure fields constitute a fundamental representation of a fluid. Since fluid governing equations such as Navier-Stokes' and Euler's equations are derived in this coordinate system, much experience has built-up in inferring the fate of particle trajectories from the observation of velocity fields. This is also a convenient representation because many common flow descriptors can be derived from it, such as vorticity, strain-rates.

Velocity is, however, not an observable quantity. Footprints and measurements of the velocity cannot be measured directly, but rather derived from Lagrangian observations. For example, the numerical derivative of a drifter path approximates the velocity along that path. The Doppler shift in the spectrum of traveling waves is used to recombine currents along a radial of a HF radar sample.

Since most applications in Engineering and Science are concerned with the position of particles or vehicles, and not their instantaneous rates of change, it is natural to focus the analysis on Lagrangian motion. For steady or quasi-steady flows, inspection of the velocity fields can provide a good qualitative description of the transport since particle trajectories are (at least approximately) streamlines of the velocity field. Real fluid flows are, however, highly unsteady, or turbulent and it becomes difficult to discern the flow structure by inspection of the velocity field, that is, the fate of individual particle. Of course, the velocity data can be integrated to provide individual particle trajectories, but these trajectories are usually very chaotic and are typically not very revealing of the overall flow geometry. However, more structured, frame-independent techniques have been developed to reveal the underlying skeletal structure that dictates the complicated stirring and mixing patterns observed in unsteady and turbulent systems.

For this chapter, velocity fields were obtain from HF radar measurements of the surface currents in and around Monterey Bay, CA. These velocity fields were numerically integrated to provide FTLE fields, and hence LCS. The purpose of this chapter was to validate the existence of these structures by comparing them with measured positions of drifter paths. It was shown that even if integrated drifter trajectories significantly deviate from measured drifter trajectories, the LCS computed from the integrated data are robust indicators of transport barriers in the actual flow.

The drifters used to help validate the fidelity of the LCS contained a drogue element at approximate depth of 5 m. HF radar observations measure current footprints at the ocean surface, which can have variations from the dynamics a few meters below, depending on the given flow conditions. This discrepancy can introduce error, in addition to inherent measurements errors, when comparing the drifter track with those predicted by HF radar measurement [71]. This is likely a significant contributor to the error seen by the difference in integrated drifter trajectories and the measured

trajectories shown in Figures 7.4–7.7. However, even though there is large deviations in these trajectories, both sets were relatively consistent with the LCS. This reaffirms the belief that LCS are robust to errors in the Eulerian velocity field, as demonstrated by Haller [32]. Work is currently underway to obtain trajectories of surface drifters which follow more closely the surface ocean dynamics, and use the data to compare with the LCS computed from HF radar. Such a comparison would help factor out the inherent discrepancies in dynamics caused by the vertical variation of the flow and help focus on the robustness of LCS to measurement errors in the velocity data.

During the AOSN experiment, there was a strong upwelling favorable period from August 6 up to August 18. Also during this period, there consistently was a well-defined LCS that extended across the mouth of the Bay, attached to Point Piños. This observation is also consistent with a similar comparison of the upwelling period during the first AOSN in August 2000 that produced an analogous LCS across the mouth of the Bay. Therefore, we can consider this LCS as a footprint that the Bay is experiencing upwelling. Around August 18, the upwelling-favorable winds reversed direction creating relaxation-favorable conditions. During this transition to relaxation the LCS extending off Point Piños moved further down shore and off coast allowing. This allowed an influx of water in the lower portion of the Bay during the days of Aug 20-22. This geometry is consistent with the dynamics typically associated with relaxation.

The formulation of computing LCS from FTLE fields is independent of the dimension of the system. Current work is underway to study LCS, not just at the surface, but for the full three-dimensional flow. This could test whether there is a well-defined two-dimensional LCS (surface embedded in the full three-dimensional ocean) that can be associated with the upwelling plume, which results from the upwelling-favorable wind forcing. If so, such a geometry could greatly aid in the visualization and subsequent interpretation of this upwelling phenomenon.

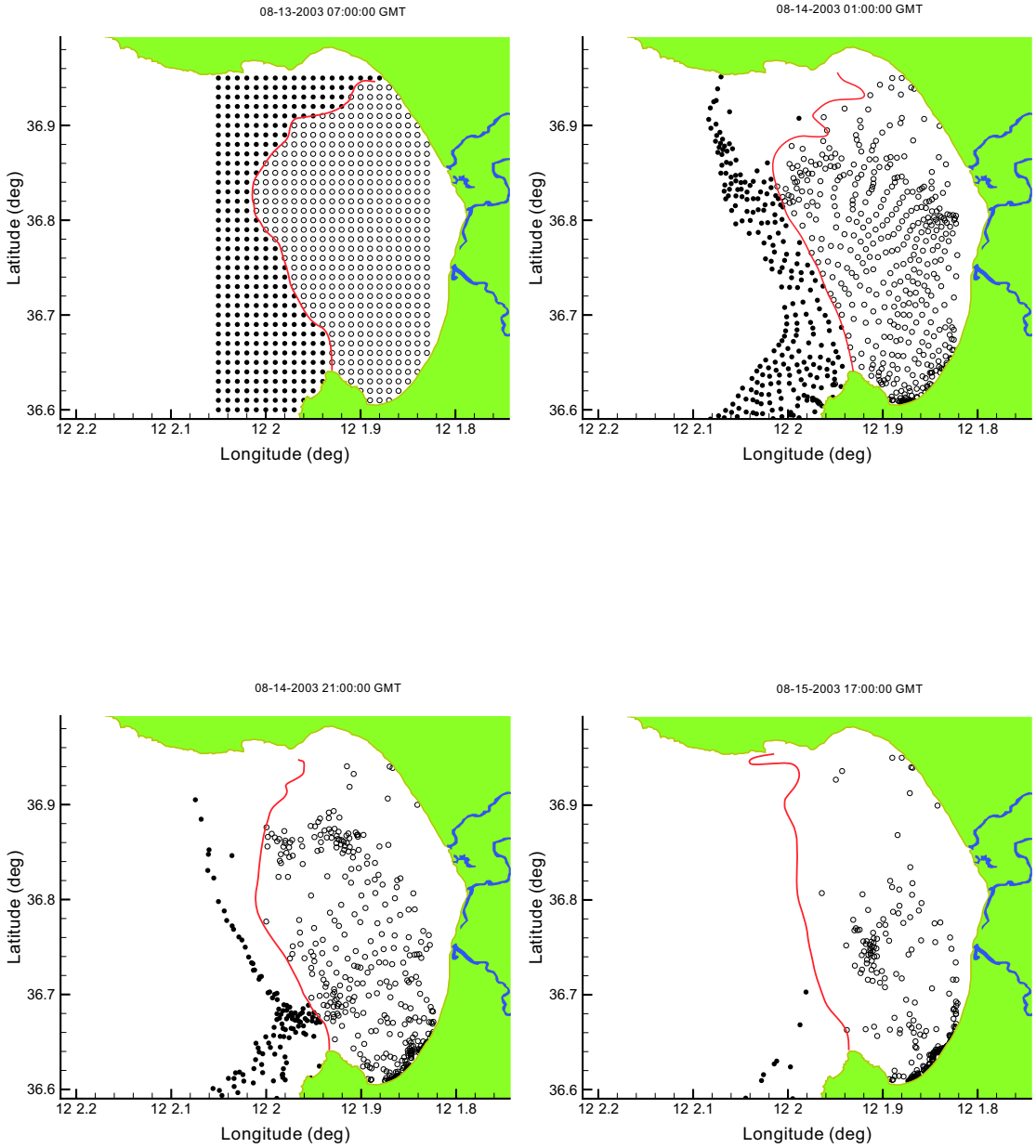

Figure 7.2: The LCS above that extends across the mouth of Monterey Bay is a moving separatrix. It divides fluid that recirculates in the Bay from fluid that moves down the California coast. Therefore, particles initially on the right of the LCS stay on the right, and particles on the left stay on the left.

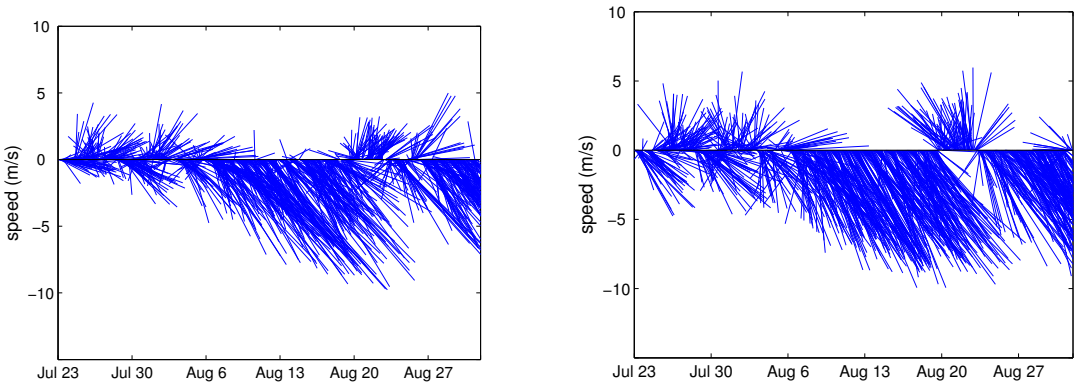

(a) M1 winds

(b) M2 Winds

Figure 7.3: Direction from which wind blows from August 23, 2003 to September 1, 2003, measured at moorings M1 (36.75 N, -122.03 W) and M2 (36.70 N, -122.39 W). North is the upward direction.

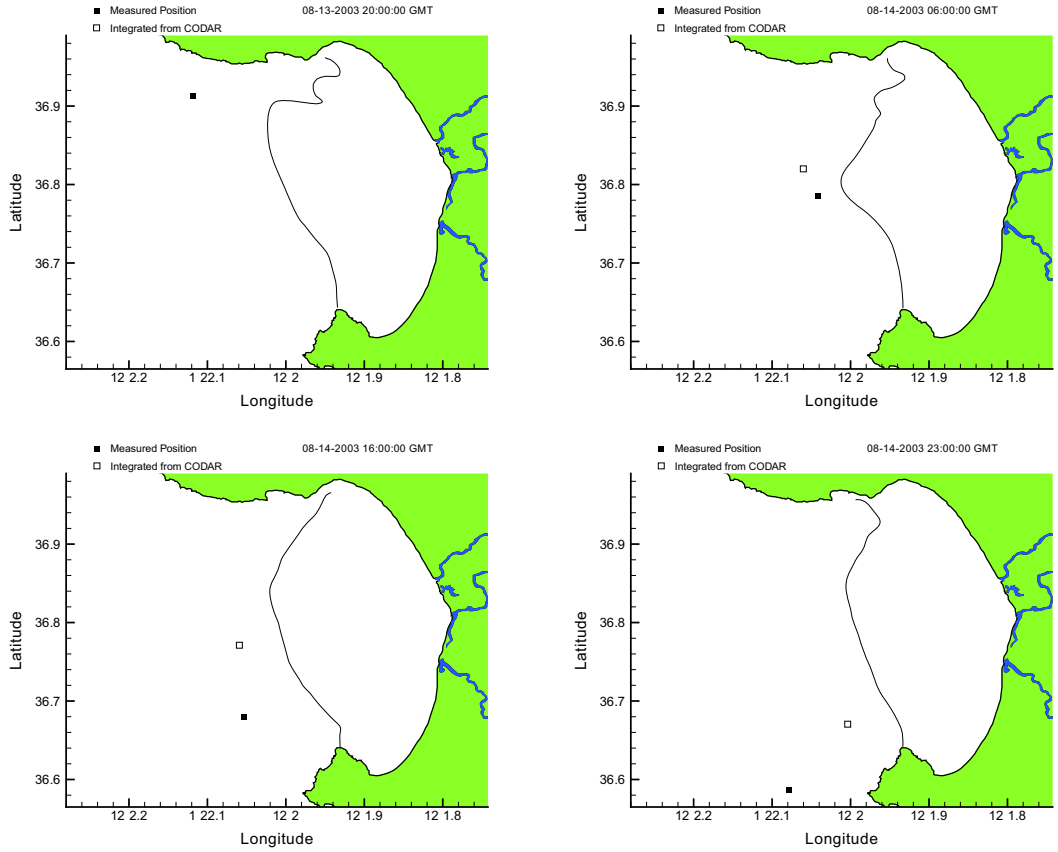

Figure 7.4: Time series locations of drifter A.

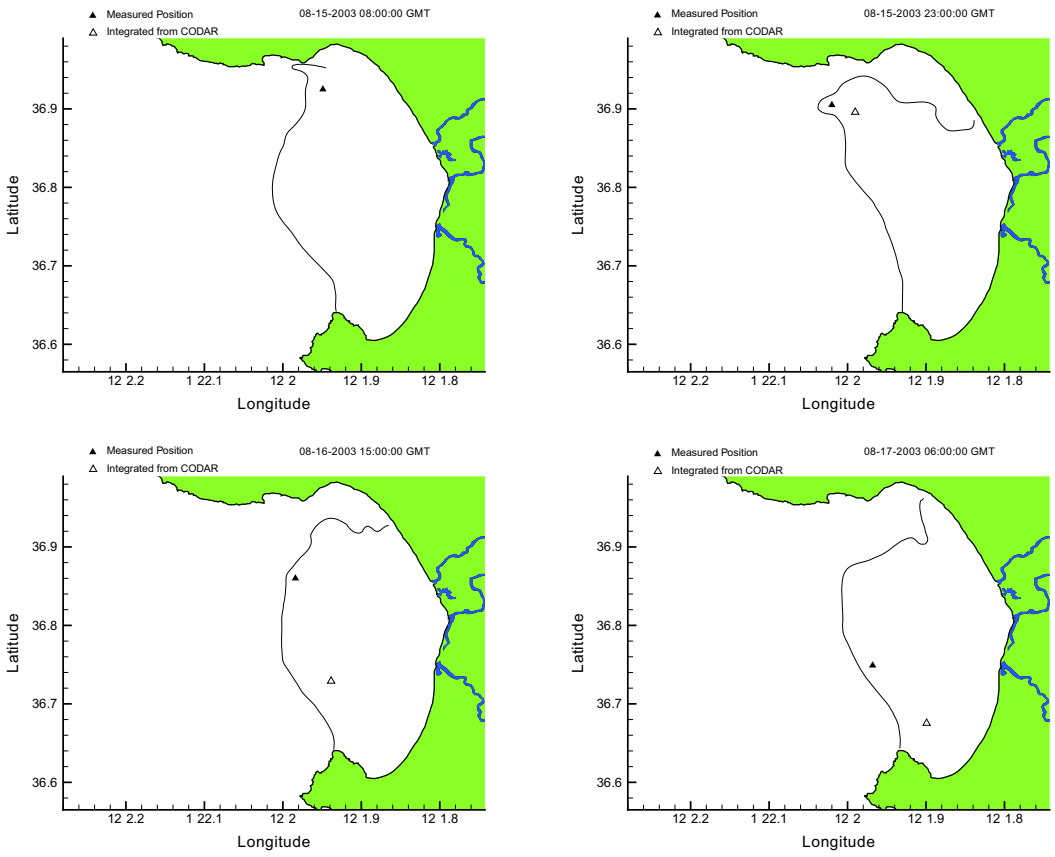

Figure 7.5: Time series locations of drifter B.

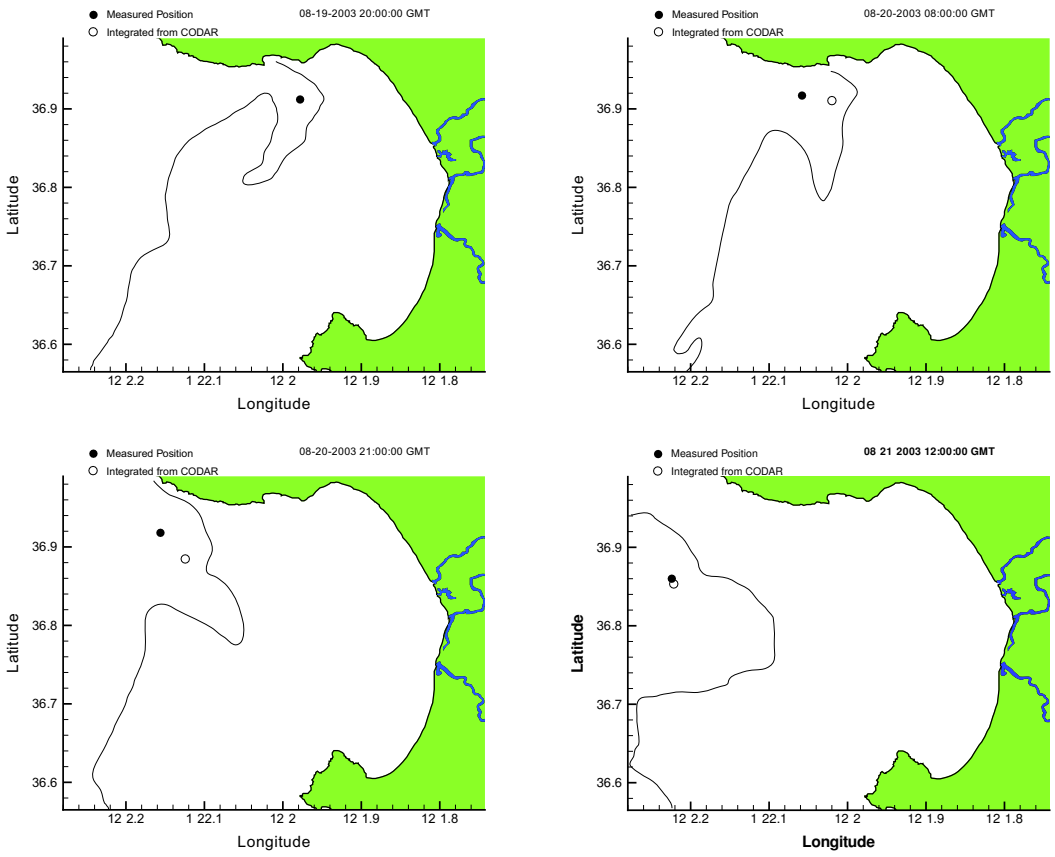

Figure 7.6: Time series locations of drifter D.

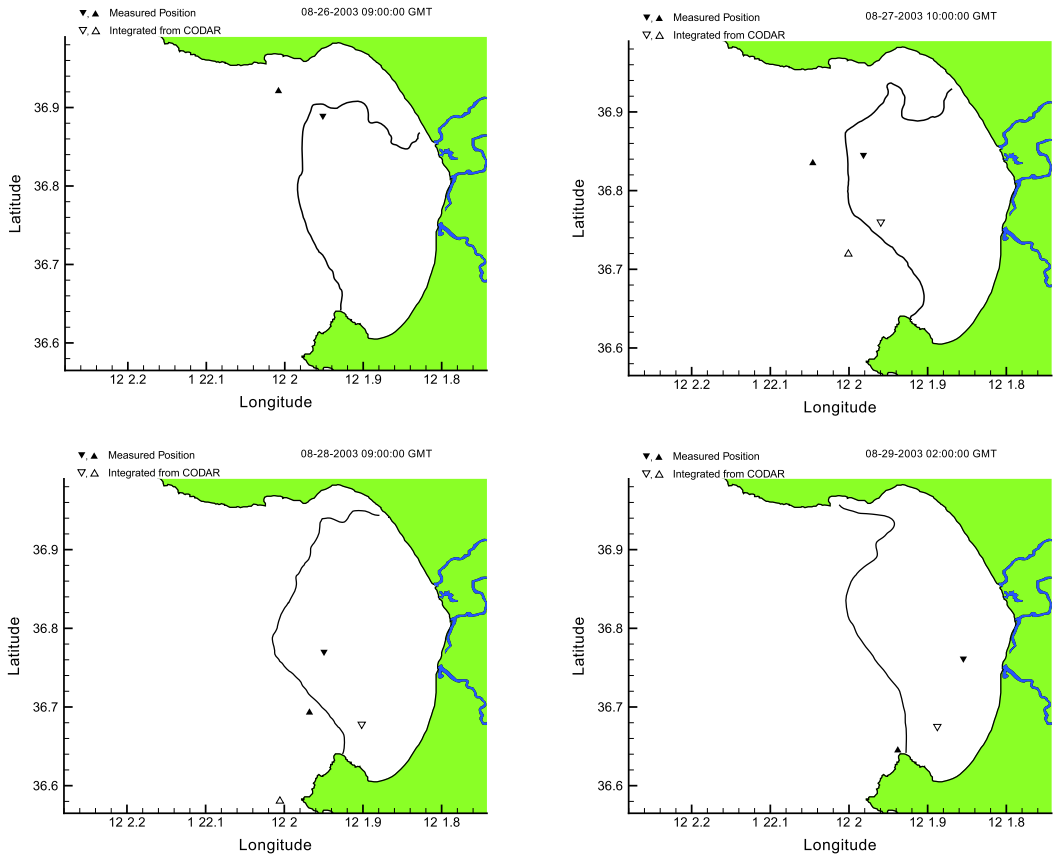

Figure 7.7: Time series locations of drifters B and D.

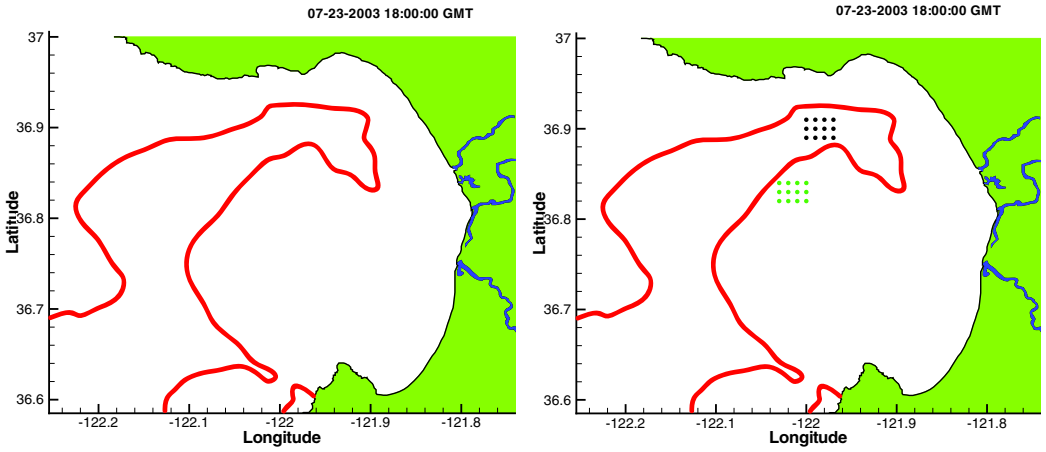

(a) LCS

(b) LCS and drifters

Figure 7.8: Panel (a) shows the location of an LCS on 07-23-2003, 18:00 GMT. Panel (b) shows the locations of two arrays of drifters on either side of the LCS.

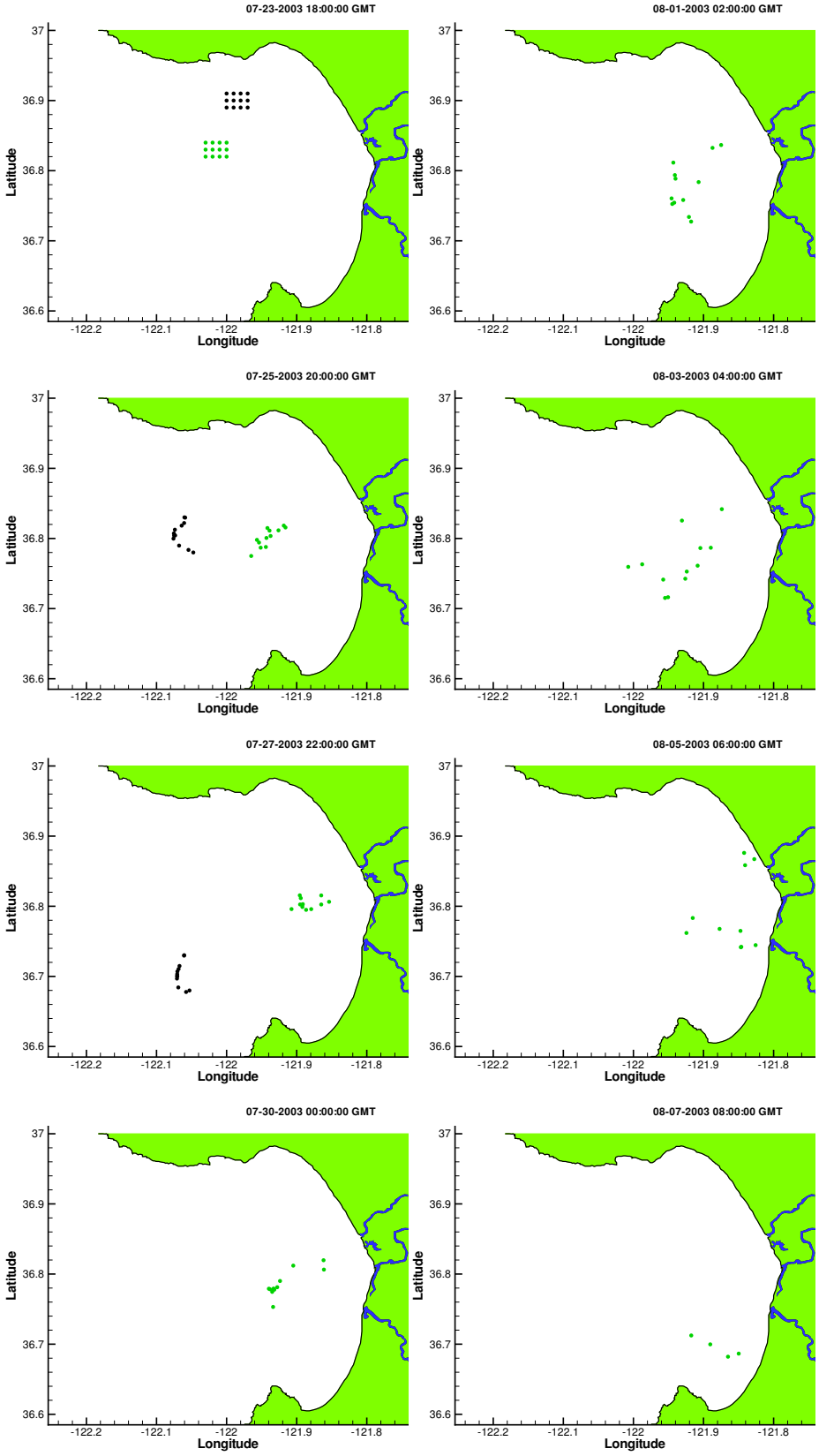

Figure 7.9: Time series location of the two groups of drifters release on either side of the LCS shown in Figure 7.8.

Chapter 8

Other Applications of LCS to Unsteady Systems

8.1 Turbulent Vortex Rings

In collaboration with Tim Colonius

This section demonstrates the application of LCS to turbulent flow. The data studied comes from a turbulent vortex ring generated by Direct Numerical Simulations (DNS) of the fully compressible, three-dimensional Navier-Stokes equations with stochastic disturbances added. The vortex ring is generated by applying a non-conservative body force to the equations of motion. Time $t = 0$ corresponds to the initiation of this force to the quiescent flow. For a complete description of the computational technique, see Ran and Colonius [84]. For the purpose of this study, the flow was averaged over several runs to factor out the radial noise in the velocity field, creating axisymmetric flow.

Figure 8.1 shows the evolution of the forward time FTLE field computed with an integration length of $T = 50$ for time ranging from $t = 0$ to $t = 71.52$ s. As time evolves a large primary vortex is formed and a smaller secondary vortex is shed from the primary structure around $t = 20$ s. The two ridges of high FTLE are repelling LCS. These LCS bound the particles that are either initially inside, or will be entrained into, the primary or secondary vortices.

Figure 8.2 is of the FTLE field computed with $T = -50$ s. Since $T < 0$, the LCS are attracting LCS. As the name implies, blobs of fluid particles will tend to align with these LCS as time evolves. As with the laminar vortex ring studied in §5.4.1, the intersection of the repelling and attracting LCS create a well-defined boundary for the turbulent vortex ring, separating re-circulating fluid from the fluid that passes around the ring. Additionally, the intersection of these structures dictate exactly which fluid is entrained or detrained from the interior of the vortex.

From inspection of the forward time field we can notice a few interesting things. First, it appears that the vortex is well-formed after about 10 s. During this formation however, there is a secondary

vortex structure that forms and circulates in the core of the primary structure. Associated with this secondary structure are filaments formed from its LCS that intertwine with the LCS of the primary vortex. The secondary vortex appears to shed around $t = 20$ s, which causes the rear of the vortex to protrude. After about $t = 26$ s the primary vortex forms stable well-defined ring. Then at approximately $t = 50$ s the primary vortex begins to quickly dissipate and loose its coherence. This is evident by the rLCS shortening in length and collapsing toward the rear (hyperbolic point). The rLCS eventually disappears, which indicates that there is no longer re-circulation occurring in the rear of the vortex.

An analogous story is revealed by inspection of the aLCS. After about $t = 26$ s the aLCS forms a well-defined, stable ring. After approximately $t = 50$ s the aLCS begins to form large lobes in the rear of the ring, which grow with time. These lobes represent the presence of heavy detrainment occurring from the vortex core. As more fluid is sucked out by these large lobes, the vortex quickly decreases in size.

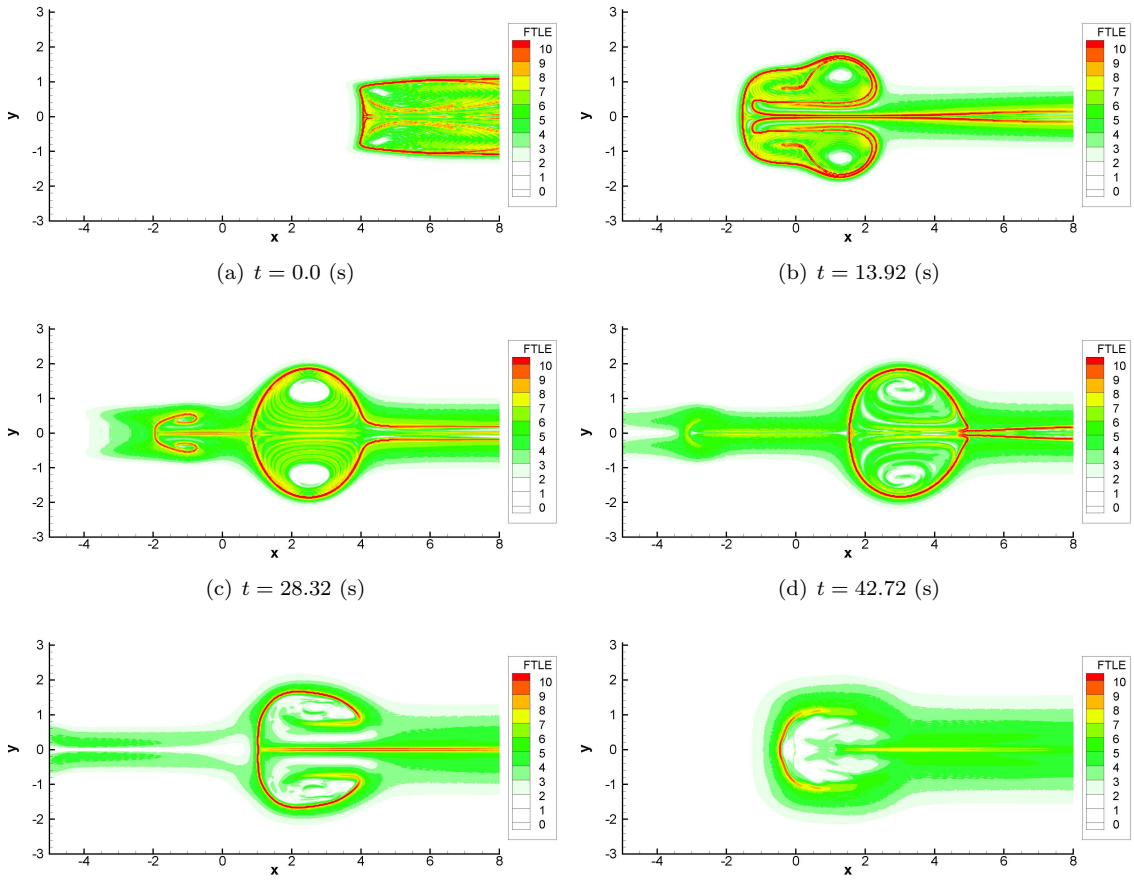

(a) $t = 0.0$ (s) (b) $t = 13.92$ (s)

(c) $t = 28.32$ (s) (d) $t = 42.72$ (s)

(e) $t = 57.12$ (s) (f) $t = 71.52$ (s)

Figure 8.1: Time variation of forward time FTLE fields for turbulent vortex ring. For the complete movie see http://www.cds.caltech.edu/∼marsden/research/demos/.

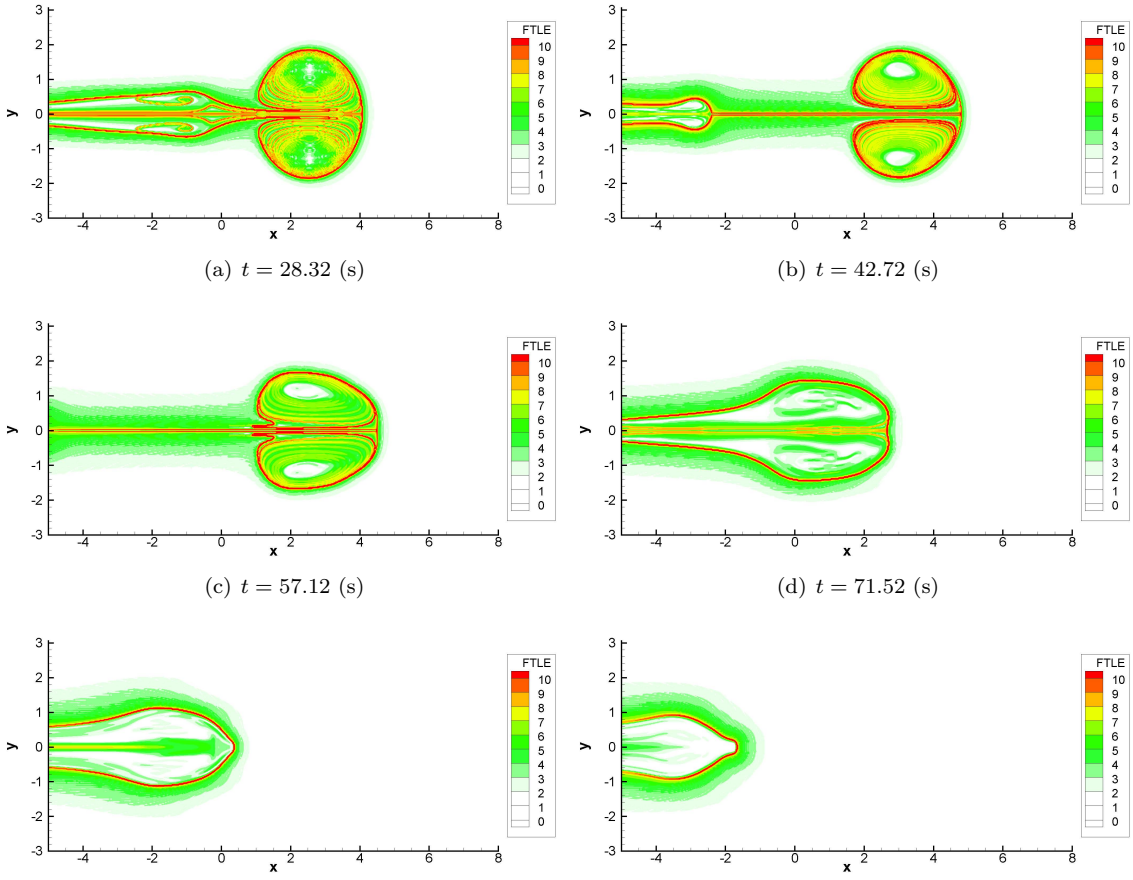

(a) $t = 28.32$ (s)

(b) $t = 42.72$ (s)

(c) $t = 57.12$ (s)

(d) $t = 71.52$ (s)

(e) $t = 85.92$ (s)

(f) $t = 95.04$ (s)

Figure 8.2: Time variation of backward time FTLE fields for turbulent vortex ring. For the complete movie see http://www.cds.caltech.edu/∼marsden/research/demos/.

To give better intuition about how the LCS shown in the previous movies dictate the flow geometry, we superimpose their time evolution with a parcel of fluid particles. The aLCS and rLCS are plotted by fitting curves to the $\sigma = 9$ level sets of both the forward (red) and backward (blue) time FTLE fields. For the purpose of visualization, this contour level does a sufficiently good job of showing the LCS without the need for an elaborate ridge extraction method. A rectangular grid of particles is seeded at the initial time $t = 24$ s. To aid the visualization, particles initially located inside the rLCS are colored black and those outside are colored green. Figure 8.3 demonstrates how the black particles are entrained and recirculate, and the green particles pass around the ring.

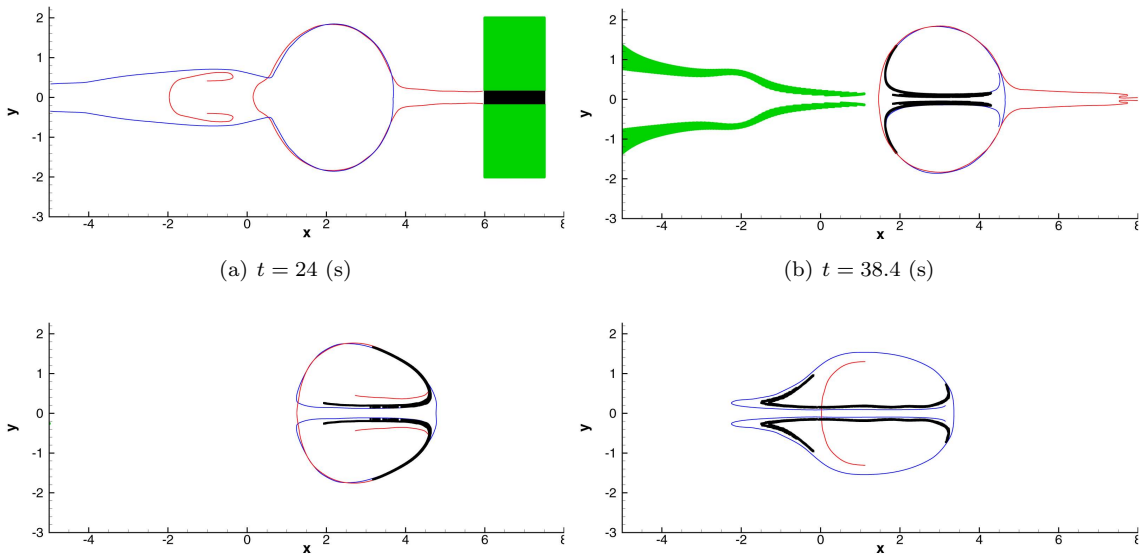

(a) $t = 24$ (s) (b) $t = 38.4$ (s)

(c) $t = 52.8$(s) (d) $t = 67.2$ (s)

Figure 8.3: Turbulent vortex ring LCS and drifter evolution.

The LCS are the true vortex boundaries because they separate the fluid that re-circulates from that which moves downstream. However, let us compare the LCS with streamline plots. Figure 8.4 makes this comparison at two separate time instances. On top, streamlines and the forward time FTLE field, i.e., the rLCS, are shown at time $t = 24$ s (the aLCS could also be shown, but the rLCS is sufficient to point out some faults of the streamline plot). The streamline plot actually does a decent job at capturing the *size* of the vortex *at this time*, the main reason being that the flow temporarily reaches a somewhat steady state. However, the main fault of the streamline method is in the delineation of the flow around the vortex. For example, from inspection of the rLCS, we see that fluid originating upstream, near the x-axis, is entrained inside the vortex (cf. Figure 8.3), which is contradictory to the geometry in Figure 8.4(a) in which the streamlines originating near the x-axis move around the exterior of the ring making it impossible to notice this heavy entrainment. Additionally streamlines on the left of the (main) vortex pass through an rLCS, therefore contradicting the true behavior of the flow in this region. As the vortex begins to dissipate, the

streamline description begins to show larger digression from the LCS description. This can be seen by comparing streamlines at $t = 71.52$ s to the aLCS at that time. From inspection of the aLCS, fluid appears to be quickly detraining from the vortex (i.e., the vortex is no longer tight core, but begins to dissipate out), but this is hard to see from the streamline plot. Additionally the extent of the vortex is significantly smaller in the streamline plot at time $t = 71.52$ s than the LCS description.

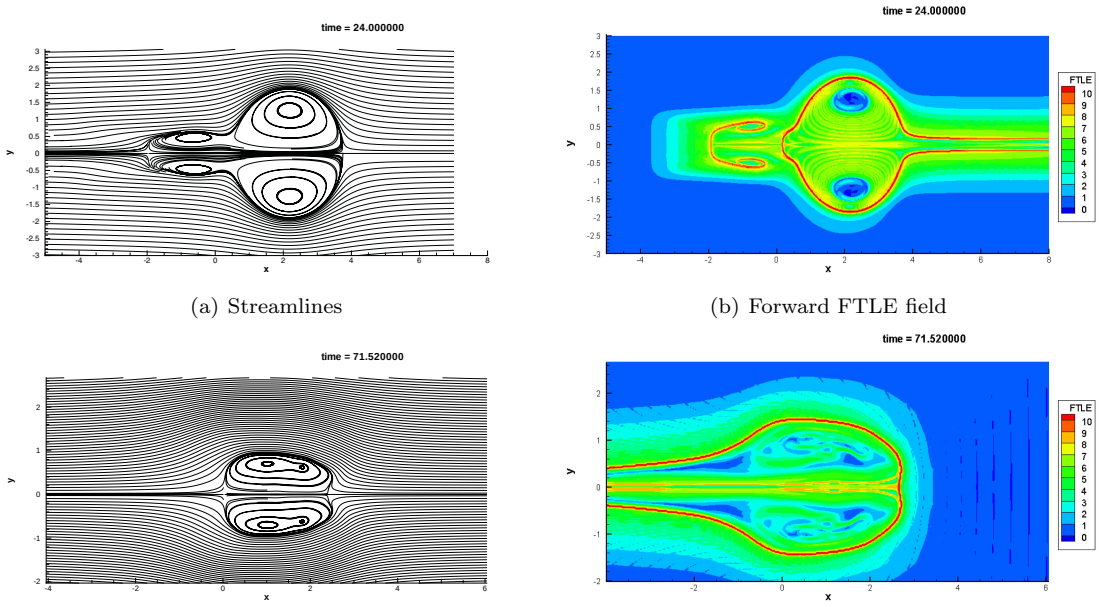

(a) Streamlines

(b) Forward FTLE field

(c) Streamlines

(d) Backward FTLE field

Figure 8.4: Comparison of LCS with streamlines for the turbulent vortex ring.

8.2 Vortex Formation

In collaboration with John Dabiri and Kakani Katija

In this section we come back to the study of isolated vortex rings produced by a piston-cylinder apparatus. The studies of Dabiri and Gharib [17] and Shadden, et al. [92] focused on the time-dependent entrainment/detrainemnt processes. However, the extent of those studies only examined the vortex dynamics after the vortex was well-defined, i.e., after approximately 2.4 s. This section focuses on understanding the exact flow geometry associated with the formation of the vortex ring, i.e., during the 0 to 2.4 s time frame.

Vortex rings were generated in the laboratory similar to the methods described in detail by Dabiri and Gharib [17]. Experiments were conducted in a 60 cm H $\times$ 40 cm W $\times$ 110 cm L water tank using a constant-head tank ($p = 8.2$ kPa) with a computer-controlled flow monitoring valve. Vortex rings were generated by allowing the flow from the constant-head tank to drive a piston that pushed fluid out of a sharp-edged cylinder (inner diameter of 2.54 cm) mounted horizontally into the

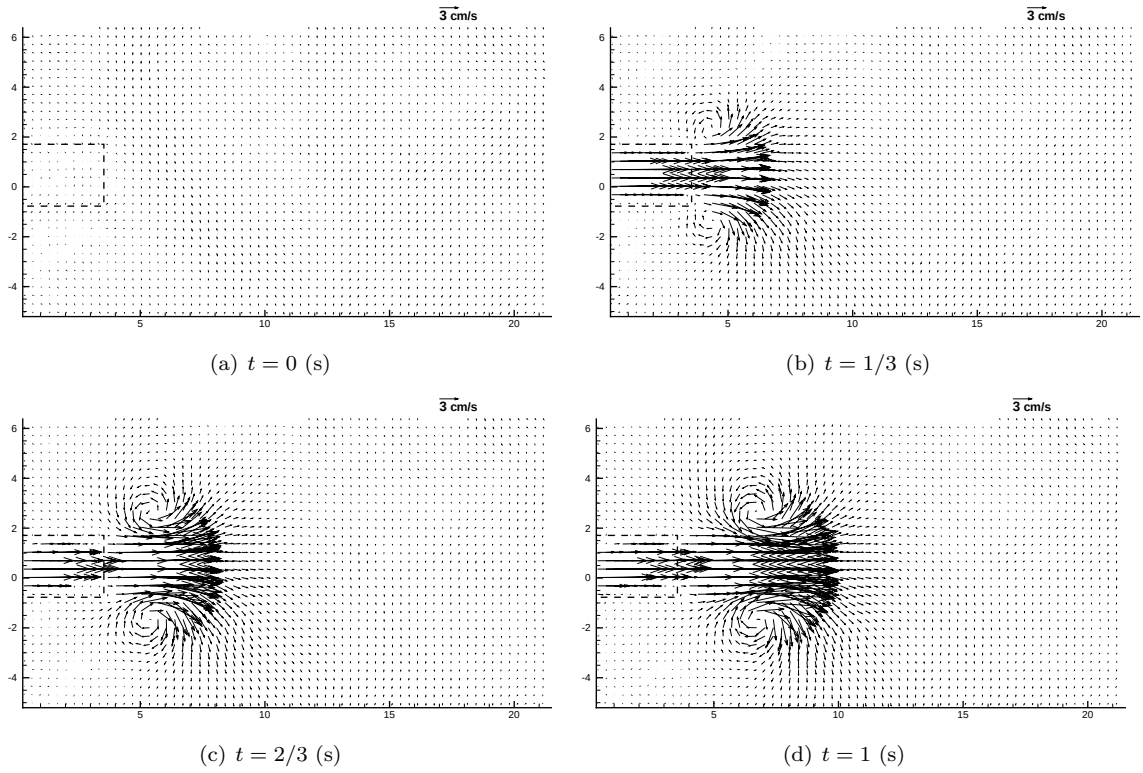

(a) $t = 0$ (s) (b) $t = 1/3$ (s)

(c) $t = 2/3$ (s) (d) $t = 1$ (s)

Figure 8.5: DPIV velocity field for vortex formation experiment. Position coordinates specified in centimeters.

surrounding fluid. The fluid was ejected at a length-to-diameter ratio (L/D) of 2, well below L/D of 4 where a trailing jet behind the leading vortex forms [25]. The setup created vortex rings by impulsively ejecting a jet of fluid at a constant velocity of 5.5 cm/s. The computer control provided precise timing and synchronization of vortex ring generation with a time resolution of 0.01 s. A CCD camera was positioned normal to the measurement plane and recorded image sequences of vortex ring generation at a rate of 30 frames per second. Image data were transferred in real time to a frame grabber linked to a PC. The spatial resolution of the images was 47.64 pixels/cm. Velocity fields for the starting jet flow were obtained quantitatively using digital particle image velocimetry (DPIV). The water tank was seeded with 13 μ glass spheres and was illuminated by two pulsed Nd:YAG lasers (New Wave Research) whose beams were collimated by a cylindrical lens before entering the test section. Images were later paired according to the method described by Willert and Gharib [113]. In the experiment, each pair of images represented a separation of 18 ms between laser pulses. The cylinder was made of clear acrylic to allow for DPIV inside the cylinder core. Figure 8.5 shows representative velocity fields produced by this method.

Figure 8.6 shows the forward time FTLE field during the vortex formation computed from the DPIV velocity measurements. The approximate cylinder location is denoted by the dashed line. FTLE values lower than 50% of the maximum are transparent. Time, $t = 0$ corresponds to the

instant before fluid is pumped out of the cylinder; therefore even though the FTLE field has a very elaborate geometry at $t = 0$, the fluid is quiescent. Contrasting the stark difference from the Lagrangian picture (FTLE field) and the Eulerian picture (velocity field) motivates the advantages of this Lagrangian approach when the flow is unsteady. Since the flow is quiescent at $t = 0$, the LCS that is shown at this time should be interpreted as the boundary of the fluid that becomes entrained into the vortex. That is, all particles "inside" the rLCS will recirculate, at least once, in the vortex core when advected by the flow, and all particles "outside" the rLCS will not recirculate.

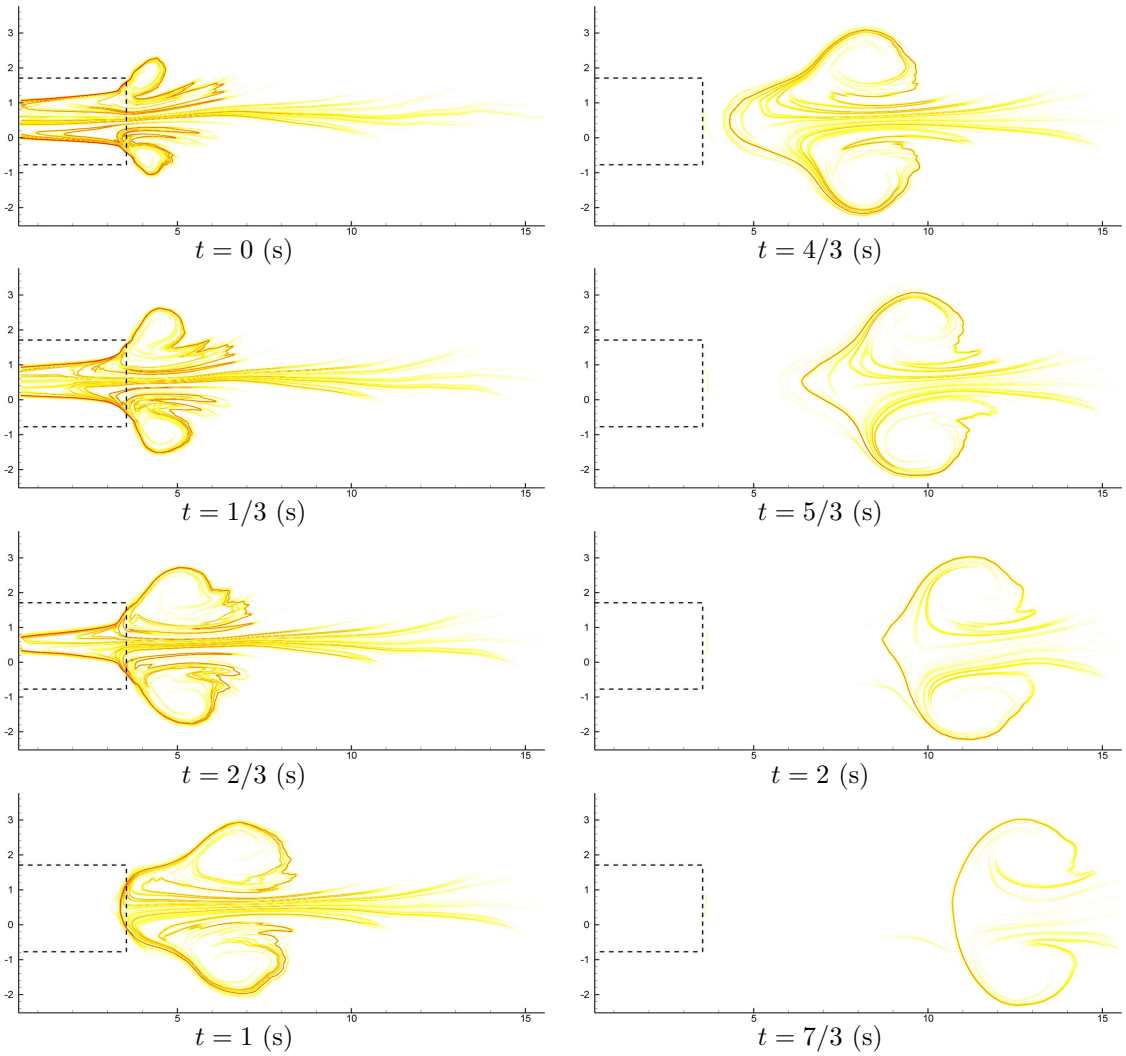

Figure 8.6: Evolution of forward time FTLE field for vortex formation. Position coordinates are specified in centimeters. The computations were done with $T = 4$ s and a grid spacing of 0.01 cm

From Figure 8.6 we can notice that the rLCS provides a well-defined rear boundary for the vortex, even at $t = 0$. In particular, the rLCS forms a long nose, or pocket, in the rear of the vortex that appears to extend well into the cylinder, slightly farther than the domain over which measurements were made. As time evolves, this pocket of fluid is entrained into the interior of the vortex, causing

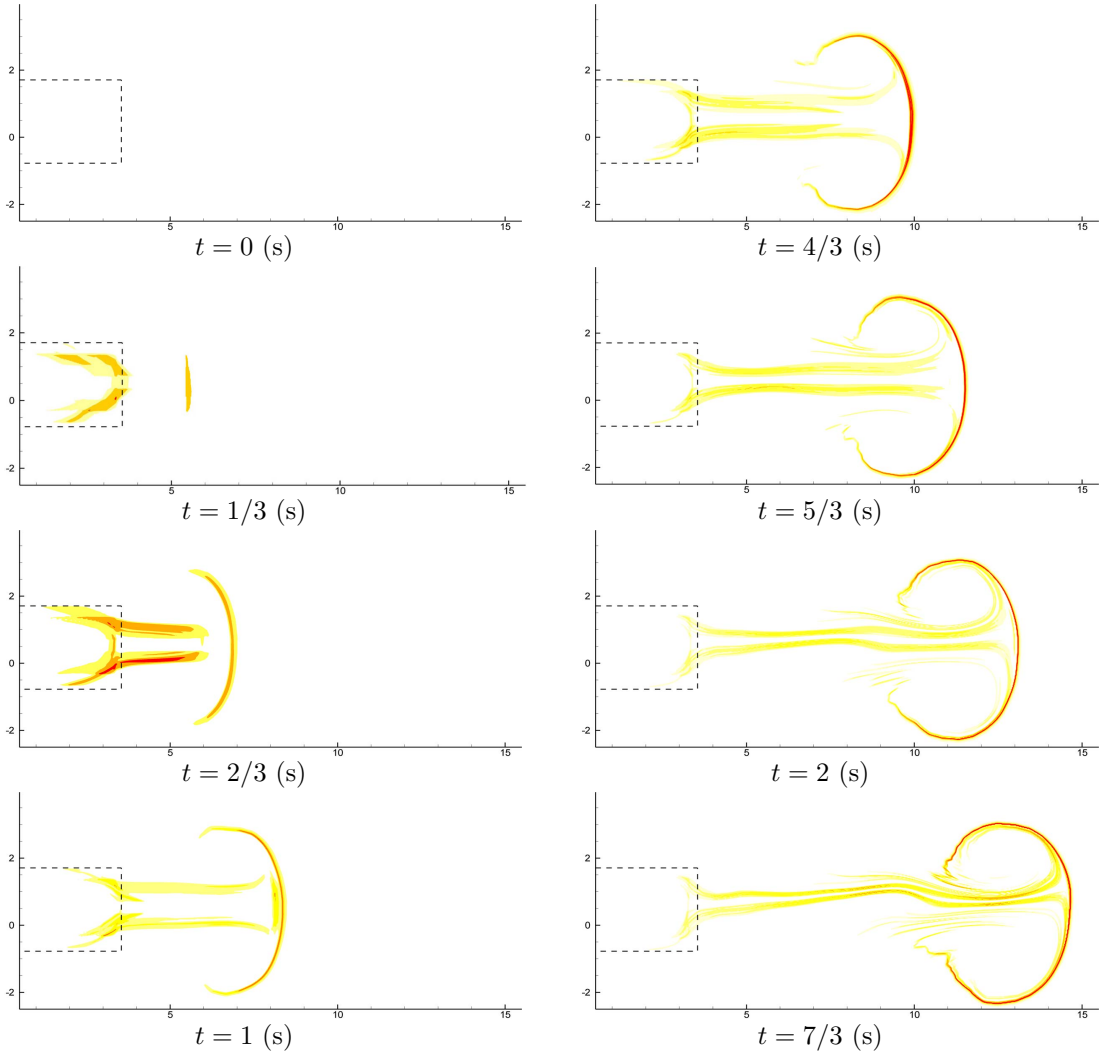

Figure 8.7: Evolution of backward time FTLE field for vortex formation. Position coordinates are specified in centimeters.

the rear boundary to morph into the familiar elliptical ring structure commonly observed. It is also clear from the dramatic looping of the rLCS that fluid is being both entrained and detrained via the lobe-dynamics shown in Shadden, et al. [92].

Figure 8.7 shows the backward time FTLE field at several instances during the vortex formation. Again, the approximate location of the cylinder is denoted by the dashed line, and FTLE values below 50% of the maximum value are transparent. No velocity data is available before $t = 0$, and alternatively the flow is quiescent for $t \leq 0$. Therefore, the FTLE field at $t = 0$ is everywhere zero (top left). Furthermore, the integration length T used to compute the FTLE fields is limited by $t = 0$. For example, the integration time used to compute the FTLE field at time $t = 1/3$ s was $T = -1/3$ s, and at $t = 2/3$ s was $T = -2/3$ s, and so on.

This example nicely demonstrates some important paradigms of LCS for unsteady systems and

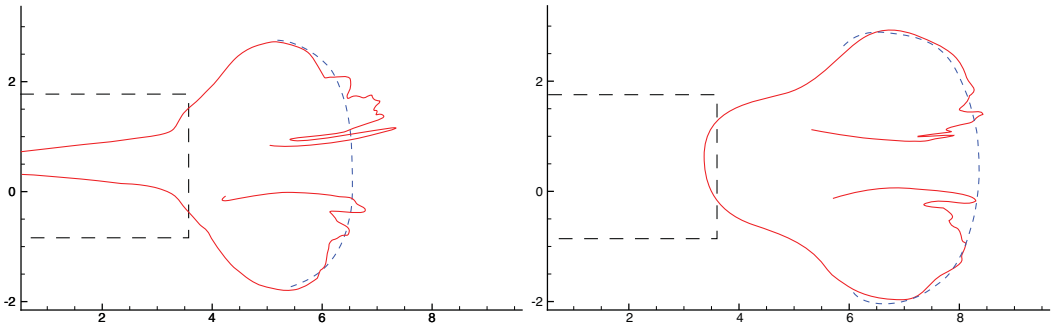

(a) $t = 2/3$ (s) (b) $t = 1$ (s)

Figure 8.8: Locations of aLCS and rLCS at two instances during the vortex formation

how they differ from traditional stable and unstable manifolds of hyperbolic points in steady or periodic systems. Since the flow is quiescent for $t \leq 0$, no aLCS can exist for any time $t \leq 0$ since the backward time FTLE field would be everywhere zero, thus not allowing any ridge. However, as Figure 8.7 clearly demonstrates, an aLCS exists for times greater than zero. We see this LCS *grow* as time increases. Note that the growth of this LCS is due to the finite time nature of this structure, and not due to the fact that a finite integration time is used to compute the structure. This clearly demonstrates the fact that some LCS, especially for highly time dependent systems, can exist strictly on finite time intervals. Additionally, to compute the backward time FTLE field at time $t > 0$, it would not be advantageous to let $T < -t$ since doing so would only scale the FTLE field, but would not yield any additional information about the location of LCS.

To help demonstrate the extent of the lobe dynamics during the formation process, the rLCS and aLCS are plotted together at two instances during the vortex formation in Figure 8.8. Time $t = 2/3$ s is approximately the time at which it is possible to use both LCS to provide a well-defined vortex boundary. Although there appears to be significant entrainment due to lobe dynamics, a far greater volume of fluid gets entrained by the induction of the rear pocket. Additionally, even though the vortex is, overall, growing in volume, detrainment is continually occurring during the formation process, although to a less extent than the entrainment, as evidenced by the respective lobe sizes, and the overall area enclosed by the LCS as time progresses.

8.3 Separation over an Airfoil

In collaboration with Jeff Eldredge

In this example we show the utility of computing LCS from FTLE fields to obtain the unsteady separation profile of flow over an airfoil. Haller [33] recently derived criteria for the existence of separation profiles in unsteady flows. In this section, we show that the existence of such a Lagrangian profile is indicated by an attracting LCS in the FTLE field. The geometry of the airfoil used here is

known as GLAS-II and has been used in the area of active flow control where an oscillatory blowing valve is placed on the surface of the airfoil to provide regulated pressure oscillations by means of blowing and suction. This enables control of the separation and reattachment points over the airfoil, and hence control of aerodynamic properties such as lift and drag.

The velocity data used to compute FTLE was obtained by a viscous vortex method [13, 23] and provided by Jeff Eldredge. Figure 8.9 shows the FTLE field for two different times. There is a noticeable LCS attached to the rear of the airfoil.

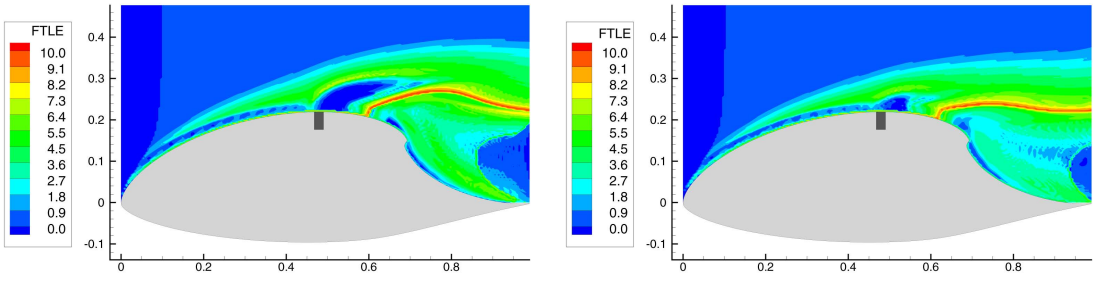

(a) $t = 0.0$ (b) $t = 3.2$

Figure 8.9: Time evolution of FTLE field on the airfoil. An LCS following the separation profile is clearly visible. For the complete movie see.

In Figure 8.10 we have plotted the evolution of the FTLE field together with a grid of fluid particles. In these plots, however, the FTLE is plotted by a color contour plot in which high values of FTLE are shaded red and low values are white. This allows us to highlight the ridge of high FTLE (i.e., the LCS) and keep the rest of the plot transparent. This LCS reveals the separation profile that separates the free-stream flow over the airfoil from the separation bubble or dead-water zone.

An unsteady separation profile can be thought of as a material line that attracts and ejects particles near the separation point [33]. Therefore, the separation profile behaves like an unstable manifold. As previously mentioned, for time-independent systems stable manifolds produce ridges in the FTLE field when computed using a positive integration time, $T > 0$, and unstable manifolds are revealed from backward integration, $T < 0$. Therefore, the FTLE fields shown in Figure 8.10 were computed from *integrating backward in time*. To obtain the FTLE field at time t, a grid of particles is advected from time t to time $t - |T|$ (or equivalently $t + T$ where $T < 0$). Once FTLE has been computed in this manner for a series of times t, the forward time evolution of the LCS can then be presented by sequentially showing these fields as t increases.

To demonstrate the Lagrangian behavior of the LCS, a uniform grid of fluid particles is placed in the flow at time $t = 0$. Particles initially located above the LCS are colored green, while particles initially located below the LCS are colored black. Note that the trajectories of these particles were *not* used to compute FTLE, since these particles are being advected *forward* in time. The location

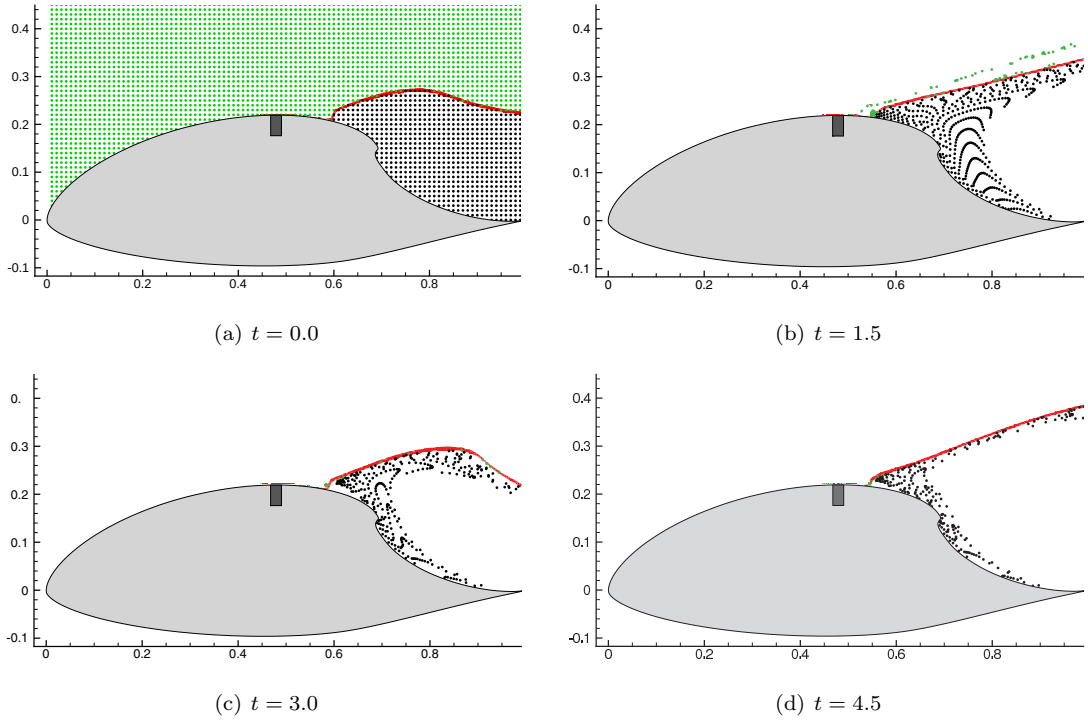

(a) $t = 0.0$ (b) $t = 1.5$

(c) $t = 3.0$ (d) $t = 4.5$

Figure 8.10: Evolution of LCS and a grid of fluid particles over the airfoil. The LCS represents the separation profile that marks the boundary between the free-stream flow from the dead-water zone behind the airfoil. For the complete movie see http://www.cds.caltech.edu/∼marsden/research/demos/.

of the blowing valve is denoted by the dark gray rectangle located on the top, center of the airfoil in Figure 8.10. The flow is actuated to produce a highly unsteady separation point. As we can see from Figure 8.10, even though the LCS is itself highly unsteady, it does a remarkable job capturing not just a transport barrier between the two regions, but the actual separation profile. Particles located above the LCS exit the domain very quickly with the ones locally near the LCS being ejected along the structure, while particles below the LCS are slowly ejected along the LCS. For the complete animation of Figure 8.10, see http://www.cds.caltech.edu/∼marsden/research/demos/.

Note that this example demonstrates that prediction of *future* Lagrangian behavior can be obtained from FTLE fields obtained by integrating *backward in time*, e.g., predicting the qualitative behavior of particles based on their initial location with respect to the LCS. It should also be noted that the assumption listed in equation (2.13) is not satisfied at the separation point because the velocity field has a no-slip boundary condition along the surface of the airfoil. However, as this simulation shows, extrapolation of the LCS to the boundary appears to be reasonable for practical purposes. It should also be noted here that the separation location predicted by Eulerian based methods, such as Prandtl's criterion, varies significantly from the true separation location predicted by the LCS.

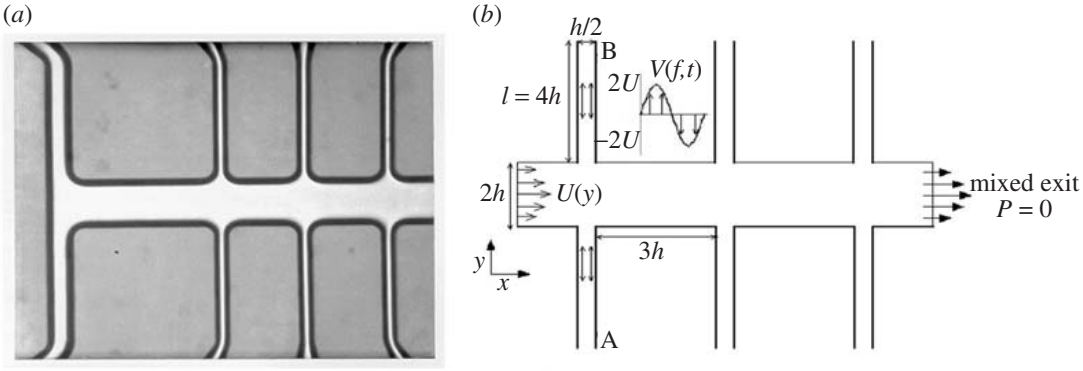

Figure 8.11: *(a)* Micrograph of the working portion of the mixing microchip. *(b)* Schematic of the fluid flow in the channel. Figure reproduced from Bottausci et al. [9].

8.4 Micromixer

In collaboration with Frederic Bottausci and Igor Mezić

In this section we analyze the mixing geometry of flow in an active micromixer. The micromixer devise consists of a main rectangular channel, two input channels that feed the main channel, and three pairs of secondary channels aligned perpendicular to the main channel, as shown in Figure 8.11. The main channel is 2h microns wide, 13.5h microns long, h microns deep, where h=100 microns. The secondary channels are 5h microns long and h/2 microns wide. The flows in the secondary channels are controlled, time-dependent oscillating profiles which are mechanically driven by an external syringe pump. Velocity measurements of the middle plane of the micromixer were obtained from a micro particle image velocimetry (μ-PIV) measurement system. The spatial resolution of the velocity measurements is approximately 5 microns and the temporal resolution is 0.4 ms. More details regarding the experimental setup and μ-PIV measurement technique can be found in [9, 8].

Mixing of two fluids is enhanced when the interface between the fluids is increased due to stretching and folding [69]. In such cases, diffusion between the two fluids has a much larger interface to occur over and thus mixing is made more efficient. In the case of the micromixer, we can demonstrate that this paradigm occurs to help provide mixing.

The μ-PIV velocity data was used to compute FTLE fields near the intersection of the main mixing channel and a secondary channel. Figure 8.12 shows the backward-time FTLE field at a junction of the main channel. For this study, the period of oscillation of the side channel flow was 5.2 ms. From the backward time FTLE field we see that an aLCS loops back and forth near the bottom corner of the junction. We next interpret the significance of this geometry.

The mechanism that is revealed is that the rLCS pulls fluid from right to left, i.e., drives the "turnstyle" mechanism that is often seen in chaotic mixing. When the cross-channel flow is directed

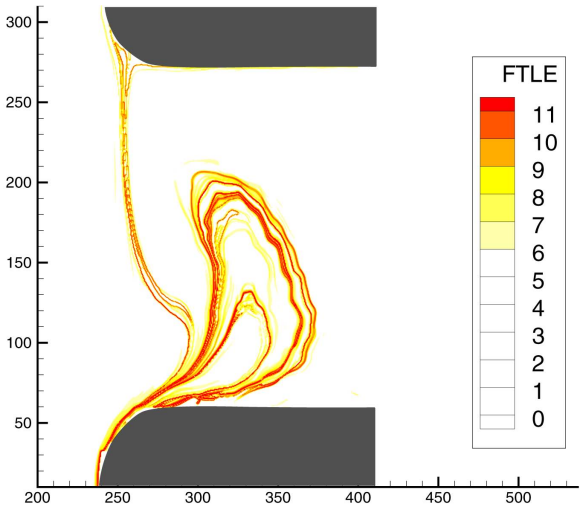

Figure 8.12: Backward time FTLE field for the micromixer. Computed using an integration time length of $T = -10.4$ ms.

downward, a blob of fluid gets pinched off near the bottom corner between the main channel and cross-channel. For example, consider the aLCS shown by the blue curve in Figure 8.13(a). Recall that fluid tends to align with aLCS. The rLCS "pulls" the aLCS up, stretching this lobe into a long filament, much like how a sewing machine works. Then when the cross-flow reverses it folds the lobe back on itself and over additional fluid that is pinched off in this process. We can think of the fluid enclosed by the aLCS at $t = 0$ as being one of the fluids needing to be mixed that initially resides in the lower half of the micromixer. When this lobe of fluid becomes stretched and then folds over, it pinches off fluid from the upper portion of the mixing channel, thus creating a much larger interface between the two fluids. This process then repeats to create thin striations of well mixed fluid as time evolves.

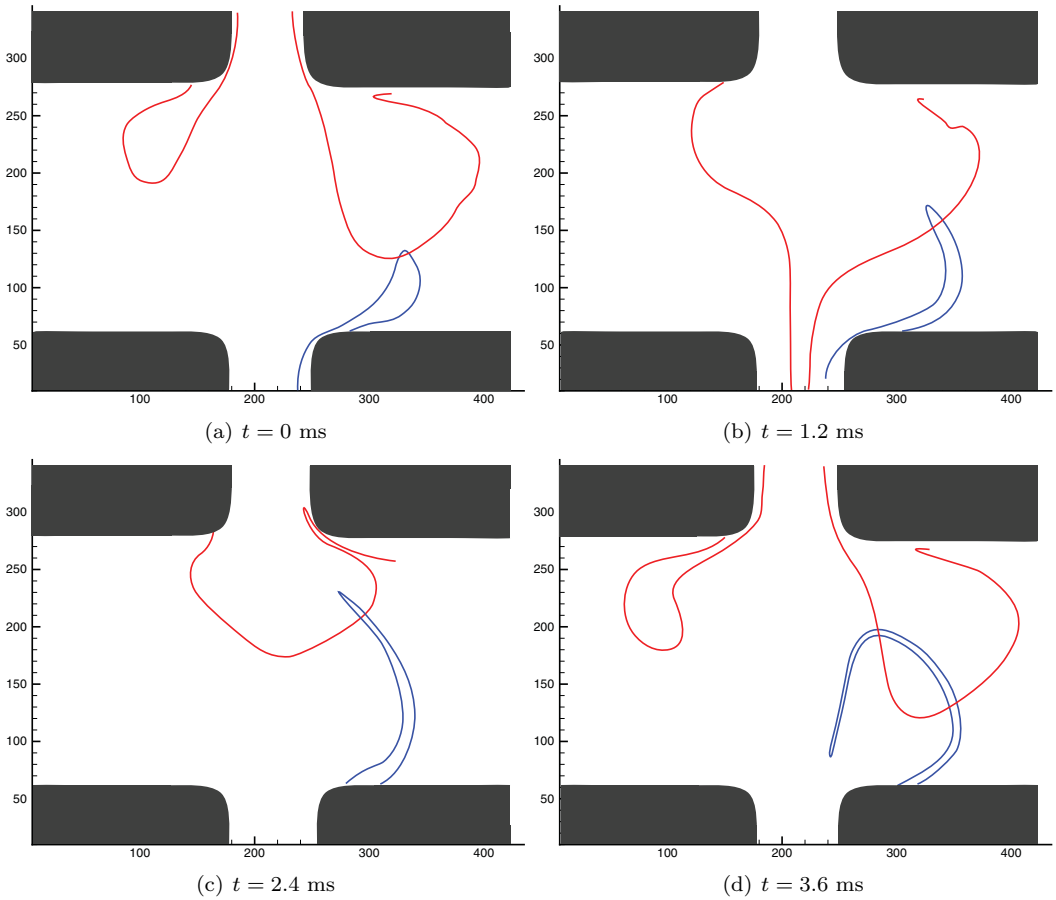

(a) $t = 0$ ms (b) $t = 1.2$ ms

(c) $t = 2.4$ ms (d) $t = 3.6$ ms

Figure 8.13: Evolution of the attracting (blue) and repelling (red) LCS show the classic stretching and folding of fluid that is the basis for chaotic mixing.

Chapter 9

Conclusions

Particle trajectories for unsteady systems are often chaotic, making direct interpretation difficult. It is often easier, and more intuitive, to plot the velocity field of the fluid at fixed locations in space, or streamlines of the velocity field, to visualize the dynamics. However, for unsteady systems, these Eulerian approaches typically do a poor job providing an understanding of how the *fluid itself* evolves over time, or identifying coherent patterns in the flow. Their dependence on coordinate choice is also undesirable. While the Lagrangian approach is clearly attractive for unsteady systems, care must be taken to ensure that Lagrangian-based techniques produce an intuitive description of the flow that can be readily interpreted. This thesis presents a method which helps address this problem by exploring a technique that can be used to reveal often non-obvious separatrices in unsteady flows, which can greatly illuminate the flow geometry. The approach is based on Lagrangian information, but is plotted as an Eulerian quantity, which aids interpretation.

In particular, Finite-Time Lyapunov Exponent (FTLE) fields are used to located Lagrangian Coherent Structures (LCS), which are quasi-invariant, co-dimension 1 manifolds that partition fluid with qualitatively different dynamics. The FTLE can be thought of as a local, finite-time measure of hyperbolicity. In other words, the FTLE at a point measures how strongly nearby trajectories diverge or converge over a fixed, finite interval. Therefore, the FTLE can be thought of as a measure of sensitivity to initial conditions. In fact, the traditional Lyapunov exponent was developed to provide such a measure. However, its use is more statistical and quantifies the long term behavior of trajectories. Such an asymptotic approach is often meaningless for unsteady systems, however, when properly used, the FTLE can reveal a very clear and elaborate understanding of the flow structure of unsteady systems.

The first half of this thesis focuses on the theoretical framework of defining LCS from FTLE fields, which is contained in Chapters 2 and 3. Chapter 2 addresses 2-D dynamical systems and defines LCS as *ridges* in the FTLE field. A ridge is a special gradient line of the FTLE field that is transverse to the direction of minimum (most negative) curvature. It is shown that for well-defined LCS, the flux, while not necessarily zero, is usually negligible, and therefore these structures are

effectively transport barriers, which had been previously concluded in the past literature, but not proven. Chapter 3 extends the ridge definition to dynamical systems with dimension greater than two, and shows that the flux estimate derived in Chapter 2 can be extended to LCS for higher-dimensional systems.

Chapter 4 overviews the computation of FTLE and LCS and some related concerns hopefully to allow readers the ability to understand the algorithm used to provide the results shown in this thesis. The remaining Chapters, 5–8, demonstrate the application of the FTLE method for computing LCS on a range of applications, from geophysical to microfluidic flows. These examples demonstrate that LCS seem to be ubiquitous in a variety of practical fluid flows on many scales, *and* that the method presented here offers an accessible and robust way to locate such structures. These results also reaffirm a longstanding belief that hyperbolic structures play a key role in influencing transport and mixing. While the ability to compute the important hyperbolic structures for steady and periodic systems is well-developed and relatively straightforward, the understanding is less developed for unsteady systems. Hopefully this thesis provides some needed insight in helping to advance this understanding.

It is reasonable to believe that other complex flows of interest in nature and technology should be examined within the framework described here to help understand the transport structure of such systems. For example, flows in the cardiovascular system represent significant opportunities for such an analysis as it has long been believed that hemodynamic flow structures relate to molecular, cellular, tissue, and system-level biological changes [106].

It is clear that for visualization purposes, these techniques are not practical for systems with dimension larger than three. Fortunately, fluid flows are 3-D (or less). However, even for 3-D systems, current techniques used to compute FTLE and LCS become computationally intensive. To make this method useful for higher dimensional systems, including those where visualization is not an option but one still desires the parametrization of the LCS, there is a need for automated algorithms to extract theses structures.

Bibliography

[1] R. J. Adrian. Particle-imaging techniques for experimental fluid mechanics. *Annual Review of Fluid Mechanics*, 23:261–304, 1991.

[2] P. E. Arratia, G. A. Voth, and J. P. Gollub. Stretching and mixing of non-Newtonian fluids in time-periodic flows. *Physics of Fluids*, 17(5):053102, 2005.

[3] R. Bachmayer, N. Leonard, J. Graver, E. Fiorelli, P. Bhatta, and D. Paley. Underwater gliders: Recent developments and future applications. In *IEEE International Symposium on Underwater Technology*, Tapei, Taiwan, 2004.

[4] E. Beckenbach and L. Washburn. Low-frequency waves in the Santa Barbara channel observed by high-frequency radar. *Journal of Geophysical Research-Oceans*, 109(C02):C02010 1–18, 2004. C02010.

[5] D. Beigie. Multiple separatrix crossing in multi-degree-of-freedom Hamiltonian flows. *Journal of Nonlinear Science*, 5(1):57–103, 1995.

[6] D. Beigie, A. Leonard, and S. Wiggins. A global study of enhanced stretching and diffusion in chaotic tangles. *Physics of Fluids A-Fluid Dynamics*, 3(5):1039–1050, 1991.

[7] J. T. Betts. *Practical methods for optimal control using nonlinear programming.* Advances in design and control. Society for Industrial and Applied Mathematics, Philadelphia, PA, 2001.

[8] F. Bottausci, C. Cardonne, C. D. Meinhart, and I. Mezic. Shear superposition micromixer, preprint, 2006.

[9] F. Bottausci, I. Mezic, C. D. Meinhart, and C. Cardonne. Mixing in the shear superposition micromixer: Three-dimensional analysis. *Philosophical Transactions of the Royal Society of London Series a-Mathematical Physical and Engineering Sciences*, 362(1818):1001–1018, 2004.

[10] A. E. Bryson and Y. Ho. *Applied optimal control: Optimization, estimation, and control.* Hemisphere Pub. Corp., New York, 1975.

[11] G. F. Carnevale and R. C. Kloosterziel. Lobe shedding from propagating vortices. *Physica D*, 76(1-3):147–167, 1994.

[12] W. A. Coppel. *Dichotomies in stability theory*. Springer-Verlag, New York, 1978.

[13] G. H. Cottet and P. D. Koumoutsakos. *Vortex methods: Theory and practice*. Cambridge University Press, New York, 2000.

[14] C. Coulliette and S. Wiggins. Intergyre transport in a wind-driven, quasigeostrophic double gyre: An application of lobe dynamics. *Nonlinear Processes in Geophysics*, 7(1-2):59–85, 2000.

[15] T. B. Curtin and J. G. Bellingham. Autonomous ocean-sampling networks. *IEEE Journal of Oceanic Engineering*, 26(4):421–423, 2001.

[16] J. O. Dabiri, S. P. Colin, J. H. Costello, and M. Gharib. Flow patterns generated by oblate medusan jellyfish: Field measurements and laboratory analyses. *Journal of Experimental Biology*, 208(7):1257–1265, 2005.

[17] J. O. Dabiri and M. Gharib. Fluid entrainment by isolated vortex rings. *Journal of Fluid Mechanics*, 511:311–331, 2004.

[18] J. O. Dabiri and M. Gharib. The role of optimal vortex formation in biological fluid transport. *Proceedings of the Royal Society B-Biological Sciences*, 272(1572):1557–1560, 2005.

[19] J. O. Dabiri and M. Gharib. Starting flow through nozzles with temporally variable exit diameter. *Journal of Fluid Mechanics*, 538:111–136, 2005.

[20] J. O. Dabiri, M. Gharib, S. P. Colin, and J. H. Costello. Vortex motion in the ocean: In situ visualization of jellyfish swimming and feeding flows. *Physics of Fluids*, 17(9):091108, 2005.

[21] C. de Boor. *A practical guide to splines*. Applied mathematical sciences. Springer, New York, 2001.

[22] L. Dieci and T. Eirola. On smooth decompositions of matrices. *Siam Journal on Matrix Analysis and Applications*, 20(3):800–819, 1999.

[23] J. D. Eldredge, T. Colonius, and A. Leonard. A vortex particle method for two-dimensional compressible flow. *Journal of Computational Physics*, 179(2):371–399, 2002.

[24] E. Fiorelli, N. Leonard, P. Bhatta, D. Paley, R. Bachmayer, and D. M. Fratantoni. Multi-AUV control and adaptive sampling in Monterey Bay. In *IEEE Autonomous Underwater Vehicles 2004: Workshop on Multiple AUV Operations*, Sebasco, ME, 2004.

[25] M. Gharib, E. Rambod, and K. Shariff. A universal time scale for vortex ring formation. *Journal of Fluid Mechanics*, 360:121–140, 1998.

[26] P. E. Gill, W. Murray, M. A. Saunders, and M.H. Wright. User's guide for NPSOL (version 4.0): A Fortran package for nonlinear programming: Stanford Systems Optimization Laboratory, **86**, 1986.

[27] G. Gomez, W. S. Koon, W. S. Lo, J. E. Marsden, J. Masdemont, and S. D. Ross. Connecting orbits and invariant manifolds in the spatial restricted three-body problem. *Nonlinearity*, 17(5):1571–1606, 2004.

[28] J. Guckenheimer and P. Holmes. *Nonlinear oscillations, dynamical systems, and bifurcations of vector fields*. Applied mathematical sciences. Springer-Verlag, New York, 1986.

[29] G. Haller. Finding finite-time invariant manifolds in two-dimensional velocity fields. *Chaos*, 10(1):99–108, 2000.

[30] G. Haller. Distinguished material surfaces and coherent structures in three-dimensional fluid flows. *Physica D*, 149(4):248–277, 2001.

[31] G. Haller. Lagrangian structures and the rate of strain in a partition of two-dimensional turbulence. *Physics of Fluids*, 13(11):3365–3385, 2001.

[32] G. Haller. Lagrangian coherent structures from approximate velocity data. *Physics of Fluids*, 14(6):1851–1861, 2002.

[33] G. Haller. Exact theory of unsteady separation for two-dimensional flows. *Journal of Fluid Mechanics*, 512:257–311, 2004.

[34] G. Haller and A. C. Poje. Finite time transport in aperiodic flows. *Physica D-Nonlinear Phenomena*, 119(3-4):352–380, 1998.

[35] G. Haller and G. Yuan. Lagrangian coherent structures and mixing in two-dimensional turbulence. *Physica D-Nonlinear Phenomena*, 147(3-4):352–370, 2000.

[36] Philip Hartman. *Ordinary differential equations*. Classics in applied mathematics. Society for Industrial and Applied Mathematics, Philadelphia, 2nd edition, 2002.

[37] J. R. Hove, R. W. Koster, A. S. Forouhar, G. Acevedo-Bolton, S. E. Fraser, and M. Gharib. Intracardiac fluid forces are an essential epigenetic factor for embryonic cardiogenesis. *Nature*, 421(6919):172–177, 2003.

[38] T. Inanc, S. C. Shadden, and J.E. Marsden. Optimal trajectory generation in ocean flows. In *American Control Conference*, pages 674–679, Portland, OR, USA, 2005.

[39] C. K. R. T. Jones and S. Winkler. Invariant manifolds and Lagrangian dynamics in the ocean and atmosphere. In B. Fiedler, editor, *Handbook of dynamical systems*, volume 2, pages 55–92. Elsevier, Amsterdam, 2002.

[40] B. Joseph and B. Legras. Relation between kinematic boundaries, stirring, and barriers for the Antarctic polar vortex. *Journal of the Atmospheric Sciences*, 59(7):1198–1212, 2002.

[41] T. Y. Koh and B. Legras. Hyperbolic lines and the stratospheric polar vortex. *Chaos*, 12(2):382–394, 2002.

[42] R. Krasny and M. Nitsche. The onset of chaos in vortex sheet flow. *Journal of Fluid Mechanics*, 454:47–69, 2002.

[43] P. S. Krueger and A. Gharib. Thrust augmentation and vortex ring evolution in a fully pulsed jet. *AIAA Journal*, 43(4):792–801, 2005.

[44] H. Lamb. *Hydrodynamics*. Dover Publications, New York, 6th edition, 1945.

[45] F. Lekien. *Time-dependent dyanmical systems and geophysical flows*. Ph.d., California Institute of Technology, 2003.

[46] F. Lekien, S. Berman, and E. Fiorelli. Multivariate Gaussian noise generator, `http://www.lekien.com/~francois/software/rndfieldgen`., 2006.

[47] F. Lekien, C. Coulliette, R. Bank, and J. Marsden. Open-boundary modal analysis: Interpolation, extrapolation, and filtering. *Journal of Geophysical Research-Oceans*, 109(C12):C12004, 2004.

[48] F. Lekien, C. Coulliette, A. J. Mariano, E. H. Ryan, L. K. Shay, G. Haller, and J. Marsden. Pollution release tied to invariant manifolds: A case study for the coast of Florida. *Physica D-Nonlinear Phenomena*, 210(1-2):1–20, 2005.

[49] F. Lekien and N. Leonard. Dynamically consistent Lagrangian coherent structures. In S. Boccaletti, B.J. Gluckman, J. Kurths, L.M. Pecora, R. Meucci, and O. Yordanov, editors, *8th Experimental Chaos Conference*, volume 742 of *AIP Conference Proceedings*, pages 132–139, Florence, Italy, 2004.

[50] F. Lekien and J. Marsden. Tricubic interpolation in three dimensions. *International Journal for Numerical Methods in Engineering*, 63(3):455–471, 2005.

[51] A. Leonard, V. Rom-Kedar, and S. Wiggins. Fluid mixing and dynamical systems. In *International Conference on the Physics of Chaos and Systems Far from Equilibium*, volume Nuclear Physics B (Proc. Suppl.) 2, pages 179–190, 1987.

[52] P. F. J. Lermusiaux and A. R. Robinson. Data assimilation via error subspace statistical estimation, Part i: Theory and schemes. *Monthly Weather Review*, 127(7):1385–1407, 1999.

[53] N. Malhotra, I. Mezic, and S. Wiggins. Patchiness: A new diagnostic for Lagrangian trajectory analysis in time-dependent fluid flows. *International Journal of Bifurcation and Chaos*, 8(6):1053–1093, 1998.

[54] A. M. Mancho, D. Small, and S. Wiggins. Computation of hyperbolic trajectories and their stable and unstable manifolds for oceanographic flows represented as data sets. *Nonlinear Processes in Geophysics*, 11(1):17–33, 2004.

[55] A. M. Mancho, D. Small, S. Wiggins, and K. Ide. Computation of stable and unstable manifolds of hyperbolic trajectories in two-dimensional, aperiodically time-dependent vector fields. *Physica D-Nonlinear Phenomena*, 182(3-4):188–222, 2003.

[56] J. E. Marsden and M. J. Hoffman. *Elementary classical analysis*. W.H. Freeman, New York, 2nd edition, 1993.

[57] MBARI. Autonomous ocean sampling network, `http://www.mbari.org/aosn/default.htm`, 2005.

[58] V. K. Melnikov. On the stability of the center for time periodic perturbations. *Trans. Moscow Math. Soc.*, 12:3–52, 1963.

[59] I. Mezic and S. Wiggins. A method for visualization of invariant sets of dynamical systems based on the ergodic partition. *Chaos*, 9(1):213–218, 1999.

[60] M. B. Milam, K. Mushabi, and R. M. Murray. A new computational approach to real-time trajectory generation for constrained mechanical systems. In *39th IEEE Conference on Decision and Control*, Sydney, Australia, 2000.

[61] K. Misovec, T. Inanc, J. Wohletz, and R. M. Murray. Low–observable nonlinear trajectory generation for unmanned air vehicles. In *42nd IEEE Conference on Decision and Control*, Maui, Hawaii, 2003.

[62] H. K. Moffatt and D. W. Moore. Response of Hill's spherical vortex to a small axisymmetric disturbance. *Journal of Fluid Mechanics*, 87:749–760, 1978.

[63] D. W. Moore. The velocity of a vortex ring with a thin core of elliptical cross-section. *Proceedings of the Royal Society of London Series a-Mathematical Physical and Engineering Sciences*, 370(1742):407–415, 1980.

[64] C. P. Neuman and A. Sen. Suboptimal control algorithm for constrained problems using cubic splines. *Automatica*, 9(5):601–613, 1973.

[65] P. P. Niiler and J. D. Paduan. Wind-driven motions in the Northeast Pacific as measured by Lagrangian drifters. *Journal of Physical Oceanography*, 25(11):2819–2830, 1995.

[66] J. Norbury. Family of steady vortex rings. *Journal of Fluid Mechanics*, 57:417–431, 1973.

[67] B. O'Neill. *Elementary differential geometry.* Academic Press, San Diego, 2nd edition, 1997.

[68] V. I. Oseledec. A multiplicative ergodic theorem: Ljapunov characteristic numbers for dynamical systems. *Trans. Moscow Math. Soc.*, 19:197–231, 1968.

[69] J. M. Ottino. *The kinematics of mixing: Stretching, chaos, and transport.* Cambridge texts in applied mathematics. Cambridge University Press, New York, 1989.

[70] K. Padberg. *Numerical analysis of chaotic transport in dynamical systems.* Ph.d., University of Paderborn, 2005.

[71] J. D. Paduan and M. S. Cook. Mapping surface currents in Monterey Bay with CODAR-type HF radar. *Oceanography*, 10:49–52, 1997.

[72] J. D. Paduan and H. C. Graber. Introduction to high frequency radar: Reality and myth. *Oceanography*, 10:36–39, 1997.

[73] J. D. Paduan, H. C. Kim, M. S. Cook, and F.P. Chavez. Calibration and validation of direction-finding high frequency radar ocean surface current observations. *IEEE Journal of Oceanic Engineering*, In Press, 2006.

[74] J. D. Paduan and L. K. Rosenfeld. Remotely sensed surface currents in Monterey Bay from shore-based HF radar (Coastal Ocean Dynamics Application Radar). *Journal of Geophysical Research-Oceans*, 101(C9):20669–20686, 1996.

[75] H. Peters, L. K. Shay, A. J. Mariano, and T. M. Cook. Current variability on a narrow shelf with large ambient vorticity. *Journal of Geophysical Research-Oceans*, 107(C8):3087, 2002.

[76] R. T. Pierrehumbert. Large-scale horizontal mixing in planetary-atmospheres. *Physics of Fluids A-Fluid Dynamics*, 3(5):1250–1260, 1991. Part 2.

[77] R. T. Pierrehumbert and H. Yang. Global chaotic mixing on isentropic surfaces. *Journal of the Atmospheric Sciences*, 50(15):2462–2480, 1993.

[78] A. C. Poje and G. Haller. Geometry of cross-stream mixing in a double-gyre ocean model. *Journal of Physical Oceanography*, 29(8):1649–1665, 1999.

[79] C. Pozrikidis. The nonlinear instability of Hill's vortex. *Journal of Fluid Mechanics*, 168:337–367, 1986.

[80] D. Prandle. The fine-structure of nearshore tidal and residual circulations revealed by HF radar surface current measurements. *Journal of Physical Oceanography*, 17(2):231–245, 1987.

[81] W. H. Press, S. A. Teukolsky, W. T. Vetterling, and B. P. Flannery. *Numerical recipes in C: The art of scientific computing*. Cambridge University Press, New York, 2nd edition, 1992.

[82] A. Provenzale. Transport by coherent barotropic vortices. *Annual Review of Fluid Mechanics*, 31:55–93, 1999.

[83] S. R. Ramp, J. D. Paduan, I. Shulman, J. Kindle, F. L. Bahr, and F. Chavez. Observations of upwelling and relaxation events in the northern Monterey Bay during August 2000. *Journal of Geophysical Research-Oceans*, 110(C7):C07013, 2005.

[84] H. Ran and T. Colonius. Numerical simulation of sound radiated from a turbulent vortex ring. *AIAA Paper 2004-2918*, pages 1–16, 2004.

[85] A. M. Rogerson, P. D. Miller, L. J. Pratt, and C. K. R. T. Jones. Lagrangian motion and fluid exchange in a barotropic meandering jet. *Journal of Physical Oceanography*, 29(10):2635–2655, 1999.

[86] V. Romkedar. Transport rates of a class of 2-dimensional maps and flows. *Physica D*, 43(2-3):229–268, 1990.

[87] V. Romkedar, A. Leonard, and S. Wiggins. An analytical study of transport, mixing and chaos in an unsteady vortical flow. *Journal of Fluid Mechanics*, 214:347–394, 1990.

[88] V. Romkedar and S. Wiggins. Transport in 2-dimensional maps: Concepts, examples, and a comparison of the theory of Rom-Kedar and Wiggins with the Markov model of Mackay, Meiss, Ott, and Percival. *Physica D*, 51(1-3):248–266, 1991.

[89] M. Roughan, E. J. Terrill, J. L. Largier, and M. P. Otero. Observations of divergence and upwelling around Point Loma, California. *Journal of Geophysical Research-Oceans*, 110(C4), 2005. C04011.

[90] D. L. Rudnick, R. E. Davis, C. C. Eriksen, D. M. Fratantoni, and M. J. Perry. Underwater gliders for ocean research. *Marine Technology Society Journal*, 38(2):73–84, 2004.

[91] P. G. Saffman. Dynamics of vorticity. *Journal of Fluid Mechanics*, 106:49–58, 1981.

[92] S. C. Shadden, J. O. Dabiri, and J. E. Marsden. Lagrangian analysis of fluid transport in empirical vortex rings. *Physics of Fluids*, 18(4), 2006.

[93] S. C. Shadden, F. Lekien, and J. E. Marsden. Definition and properties of Lagrangian coherent structures from finite-time Lyapunov exponents in two-dimensional aperiodic flows. *Physica D-Nonlinear Phenomena*, 212(3-4):271–304, 2005.

[94] K. Shariff. *Dynamics of a class of vortex rings*. Ph.d., Stanford University, 1989.

[95] K. Shariff and A. Leonard. Vortex rings. *Annual Review of Fluid Mechanics*, 24:U235–U279, 1992.

[96] L. K. Shay, T. M. Cook, H. Peters, A. J. Mariano, R. Weisberg, E. An, A. Soloviev, and M. Luther. Very high-frequency radar mapping of surface currents. *IEEE Journal of Oceanic Engineering*, 27(2):155–169, 2002.

[97] L. K. Shay, H. C. Graber, D. B. Ross, and R. D. Chapman. Mesoscale ocean surface current structure detected by high-frequency radar. *Journal of Atmospheric and Oceanic Technology*, 12(4):881–900, 1995.

[98] S. Smale. Diffeomorphisms with many periodic points. In S. S. Cairns, editor, *Differential and Combinatorial Topology*. Princeton University Press, Princeton, N.J., 1965.

[99] T. H. Solomon and J. P. Gollub. Passive transport in steady Rayleigh-Benard convection. *Physics of Fluids*, 31(6):1372–1379, 1988.

[100] T. H. Solomon and J. P. Gollub. Sheared boundary layers in turbulent Rayleigh-Benard convection. *Physical Review Letters*, 64(20):2382–2385, 1990.

[101] T. H. Solomon and J. P. Gollub. Thermal boundary layers and heat flux in turbulent convection: The role of recirculating flows. *Physical Review A*, 43(12):6683–6693, 1991.

[102] F. Sotiropoulos, D. R. Webster, and T. C. Lackey. Experiments on Lagrangian transport in steady vortex-breakdown bubbles in a confined swirling flow. *Journal of Fluid Mechanics*, 466:215–248, 2002.

[103] R. H. Stewart and J. W. Joy. HF radio measurements of surface currents. *Deep-Sea Research*, 21(12):1039–1049, 1974.

[104] H. A. Stone, A. D. Stroock, and A. Ajdari. Engineering flows in small devices: Microfluidics toward a lab-on-a-chip. *Annual Review of Fluid Mechanics*, 36:381–411, 2004.

[105] B. Sturtevant, L. Hesselink, and J. F. Haas. Interaction of weak shock-waves with random media. *Journal of the Acoustical Society of America*, 65:S96–S96, 1979.

[106] C. A. Taylor and M. T. Draney. Experimental and computational methods in cardiovascular fluid mechanics. *Annual Review of Fluid Mechanics*, 36:197–231, 2004.

[107] C. Truesdell. *The kinematics of vorticity.* Indiana University Press, Bloomington, 1954.

[108] F. Verhulst. *Nonlinear differential equations and dynamical systems.* Springer, New York, 2nd edition, 1996.

[109] J. von Hardenberg, K. Fraedrich, F. Lunkeit, and A. Provenzale. Transient chaotic mixing during a baroclinic life cycle. *Chaos*, 10(1):122–134, 2000.

[110] G. A. Voth, G. Haller, and J. P. Gollub. Experimental measurements of stretching fields in fluid mixing. *Physical Review Letters*, 88(25):254501, 2002.

[111] S. Wiggins. *Chaotic transport in dynamical systems.* Interdisciplinary applied mathematics. Springer-Verlag, New York, 1992.

[112] S. Wiggins. The dynamical systems approach to Lagrangian transport in oceanic flows. *Annual Review of Fluid Mechanics*, 37:295–328, 2005.

[113] C. E. Willert and M. Gharib. Digital particle image velocimetry. *Experiments in Fluids*, 10(4):181–193, 1991.

[114] H. Yamada and T. Matsui. Preliminary study of mutual slip-through of a pair of vortices. *Physics of Fluids*, 21(2):292–294, 1978.

[115] G. C. Yuan, L. J. Pratt, and Ckrt Jones. Barrier destruction and Lagrangian predictability at depth in a meandering jet. *Dynamics of Atmospheres and Oceans*, 35(1):41–61, 2002.